Verification and Validation of MicroCT-based Finite Element Models of Bone Tissue Biomechanics

DOCTOR IN PHILOSOPHY

DEPARTMENT OF MECHANICAL ENGINEERING
UNIVERSITY OF SHEFFIELD

July 2016

Yuan Chen

SUPERVISOR

Prof. Marco Viceconti

Dr. Enrico Dall'Ara

Internal examiner: Prof. Damien Lacroix

External examiner: Prof. Bert Van Rietbergen

The University Of Sheffield.

INSIGNEO Institute for in silico Medicine

Acknowledgements

Publications and presentations from this thesis

Publications in scientific journals

Chen Y, Pani M, Taddei F, Mazza C, Li X, Viceconti M, 2014. Large-scale Finite Element Analysis of Human Cancellous Bone Tissue Micro-computer Tomography Data: A Convergence Study. J. Biomech. Eng. 136.

Chen Y, Dall'Ara E, Sales E, Manda K, Wallace R, Pankaj P, Viceconti M 2015. Micro-CT based Finite Element Models of Cancellous Bone Predict Accurately Displacement Computed by Elastic Registration: A Validation Study, *Submitted* to JMBBM on September 2015.

Poster presentations in conferences

Chen Y, Dall'Ara E, Li X, Viceconti, M. Effect of Bone Lamellae Heterogeneity on the Biomechanics of Cancellous Bone Tissue. Insigneo Showcase 2014, May 8 2014.

Chen Y, Pani M, Taddei F, Mazza C, Li X, Viceconti M, 2014. Convergence Study for Large-scale Finite Element Analysis of Cancellous Bone Tissue. 7th World Congress of Biomechanics WCB 2014), Boston, USA. July 6-11 2014.

Chen Y, Dall'Ara E, Pankaj P, Viceconti, M. Micro-CT Based Finite Element Models of Cancellous Bone Predict Accurately Displacement Measured with Deformable Image Registration. Insigneo Showcase 2015, May 8 2015.

Oral presentations in conferences

Chen Y, Li X, Viceconti M. Large-scale FEA of Cancellous Bones sing HPC. HPC@Sheffield at Sheffield, April 15 2013.

Chen Y, Dall'Ara E, Sales E, Manda K, Wallace R, Pankaj P, Viceconti, M. Micro-CT Based Finite Element Models of Cancellous Bone Predict Accurately Displacement Measured with Deformable Image Registration. 21st Congress of the European Society of Biomechanics, Prague, Czech Republic, July 5 - 8 2015.

Abstract

Non-destructive 3D micro-computed tomography (microCT) based finite element (microFE) model is popular in estimating bone mechanical properties in recent decades. From a fundamental scientific perspective, as the primary function of the skeleton is mechanical in nature, a lot of related biological and physiological mechanisms are mechano-regulated that becomes evident at the tissue scale. In all these research it is essential to known with the best possible accuracy the displacements, stresses, and strains induced by given loads in the bone tissue. Correspondingly, verification and validation of the microFE model has become crucial in evaluating the quality of its predictions. Because of the complex geometry of cancellous bone tissue, only a few studies have investigated the local convergence behaviour of such models and post-yield behaviour has not been reported. Moreover, the validation of their prediction of local properties remains challenging. Recent technique of digital volume correlation (DVC) combined with microCT images can measure internal displacements and deformation of bone specimen and therefore is able to provide experimental data for validation. However, the strain error of this experimental method tends to be a lot higher (in the order of several thousand microstrains) for spatial resolutions of 10-20 µm, typical element size of microFE models. Strictly speaking no validation of strain is possible. Therefore, the goal of this thesis it to conduct a local convergence study of cancellous bone microFE models generated using three microCT-based tissue modelling methods (*homogeneous tetrahedral model, homogeneous hexahedral model and heterogeneous hexahedral model*); to validate these models' prediction in terms of displacement using the novel DVC technique; and finally to compare the strain field predicted by three tissue modelling methods, in order to explore the effect of specific idealisations/simplifications on the prediction of strain.

Abbreviations

FEA	finite element analysis
microCT	micro computed tomography
HRpQCT	high resolution peripheral quantitative computed tomography
SRµCT	synchrotron radiation micro-computed tomography
microFE	microCT-based finite element
DXA	dual-energy X-ray absorptiometry
DOF	degrees of freedom
DMB	degree of mineralisation of bone
BMD	bone mineral density
TMD	tissue mineral density
DVC	digital volume correlation
BC	boundary condition
BV/TV	bone volume fraction
DIC	digital image correlation
SG	strain gauge
CFD	center finite difference
V&V	verification and validation
HPC	high performance computing
HA	hydroxyapatite
Tb.Th	trabecular thickness
Tb.Sp	trabecular spacing
DA	degree of anisotropy
α.Z	angle between main trabecular direction and loading axis

Table of Contents

Chapter1

FEA Theory and Bioengineering Background

Summary

This chapter demonstrates the standard finite element procedure using simplex tetrahedron elements as an example and explains the importance of verification and validation for such models, which are the key steps to test their reliability. The chapter also introduces the biomechanics of bone, which as a living tissue exhibits complicated mechanical properties and microstructure. The non-invasive characteristics of microCT and its ability to accurately resolve bone microstructure makes modelling bone tissue using finite element technique a popular tool in studying bone biomechanics. The main challenge is to validate the microFE models in its local predictions. The state-of-art DVC technique combined with microCT aims to provide a volumetric field of the displacement accurately, which can be used to validate such models.

1.1. The theory of finite element analysis for solid mechanics

1.1.1. General theory and assumptions

Finite element analysis (FEA) is at present a widely used and indispensable technology in engineering analysis (Bathe, 1996). It was initially developed to solve problems in traditional structural field, such as automobile and aircraft industry (Fagan, 1992). Over the decades, this technique has been continuously developed, improved and extended to other fields. In early 1970s, FEA has the first time been applied to analyse mechanical behaviour of bone tissue (Brekelmans et al., 1972). Owning to the development of computer power and imaging technique (Feldkamp et al., 1989), it has been used widely and in particular intensively in biomechanics area since 1990s (Fyhrie et al., 1992; Hollister et al., 1994; van Rietbergen et al., 1995).

Generally, the FEA is a numerical approach which seeks an approximated solution of the distribution of field variables in the problem domain that is difficult to obtain analytically (Bathe, 1996). This is achieved by discretizing the entire problem domain into small parts of simple geometry, called elements. The variable (e.g. displacement) inside each element is assumed to behave in a pre-defined manner using linear, quadratic or higher order polynomial. The unknowns are the discrete values of the field variables at the element joints, called nodes. Then the individual elements are assembled back together to give the system equations. And after assigning the material properties and boundary conditions, the system will be ready to solve using a series of linear algebraic simultaneous equations to obtain the field variables required (Fig.1.1).

1.1.2. Discretization of the problem

The foundation of FEA is taking a problem domain governed by differential equations and partitioning it into elements (meshes) with pre-defined field variable behaviour (Pointer, 2004). These series of approximation unit should strive to map, as closely as possible, the real continuous solution. The elements used in the model can be one-dimensional (1D), two-dimensional (2D) or three-dimensional (3D). 1D element allows displaying directly the bending which is one of the root of failure in structures with long member structures. For modelling systems of simple geometry and loading conditions, such as a dam loaded in plain strain state, 2D elements would be adequate. However, all structures in the real world are 3D and in many cases, the geometry of a structure to be analysed are very complicated, such as cancellous bone tissue (Fig.1.2). Therefore,

although requiring higher computational cost, in order to obtain more accurate results in every direction, modelling such an object with 3D finite elements is indispensable.
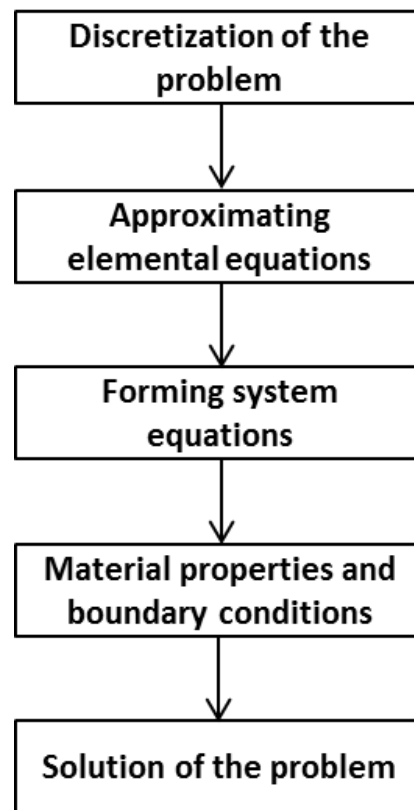
Fig.1.1. A standard procedure of FEA
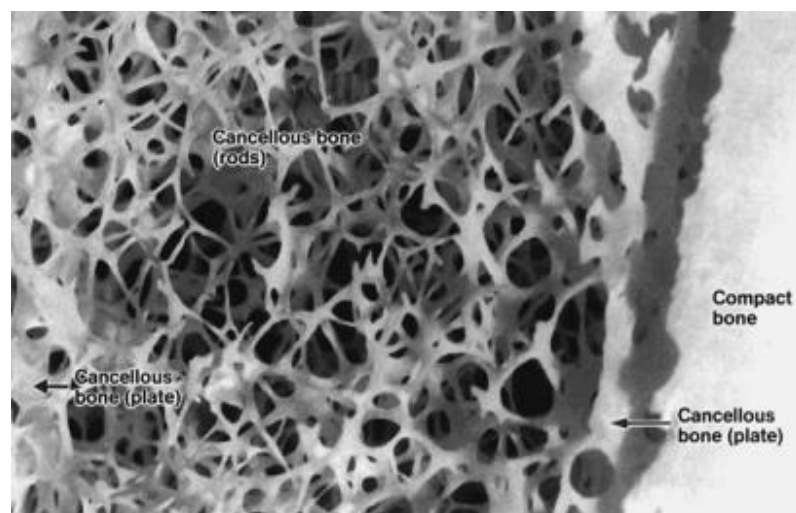
Fig.1.2. The histology of cancellous bone (From Weiss, L., Cell and Tissue Biology, A Textbook of Histology, Urban and Schwarzenberg, Baltimore, 1988).

Since its first application in 1992 (Fyhrie et al., 1992), the micro computed tomography (microCT) based finite element (microFE) method has become a popular tool for non-destructive structural analysis of cancellous bone tissue (Hollister et al., 1994; van Rietbergen et al., 1995; Verhulp et al., 2008). One of the most popular 3D elements used to model complex structure such as bone tissue is 8-node hexahedral (Polgar et al., 2001; van Rietbergen, 2001). Models with hexahedral elements, also referred to as Cartesian meshes elsewhere, are based on a direct conversion of the 3D voxels of microCT images of the bone (Feldkamp et al., 1989) into equally shaped and sized hexahedral elements. Therefore despite the complicated geometry the bone tissue has, the mesh generation is always guaranteed and the process is straightforward and efficient. Such element is defined by eight corner nodes with each node having three degrees of freedom (DOF): translation in nodal X, Y and Z directions (Fig.1.3). Finite element displacements are most accurate at the nodes with an adequate mesh density. For simpler elements, analytical solutions of the derived values (i.e. stresses and strains) are readily available. However, deriving solutions for complicated 3D elements is not trivial, and most FEA codes tend to use numerical integration to approximate the results, normally at Gauss points, where the integration error is minimum (Bathe, 1996). With eight nodes, eight shape functions can be described and two Gauss integration points are necessary for each direction, resulting in total eight Gaussian points inserted in each shape function (Bathe, 1996). For years, such bone models of Cartesian meshes have been widely used and validated to predict accurate apparent properties (e.g. stiffness, strength) with accurate experimental measurements (Christen et al., 2013; Pistoia et al., 2002; Wolfram et al., 2010; Yeni and Fyhrie, 2001). However, as this type of mesh often has a jagged surface, the boundary can only be approximated to be true when the element size is close to zero. Therefore, the only way to achieve a reliable representation of the surface geometry is to keep the size of mesh as small as possible, leading to a large number of DOFs (Huiskes and Hollister, 1993; van Rietbergen, 2001; Viceconti, 2012). Consequently, simulations of such model are highly computationally expensive and sometimes with low prediction accuracy on the bone surface (Depalle et al., 2012).
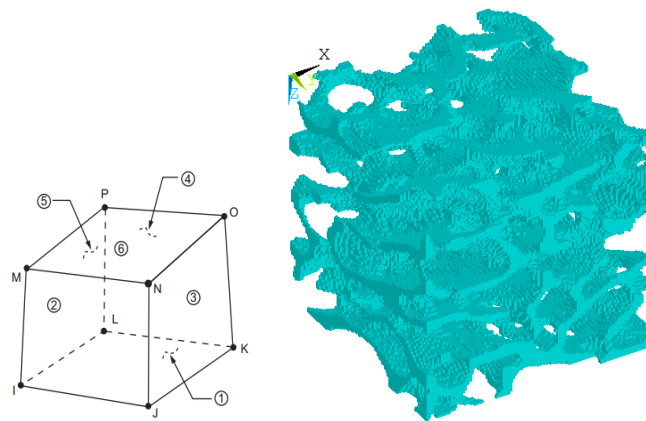
Fig.1.3. *Eight-node hexahedral element and its FE model of cancellous bone tissue*
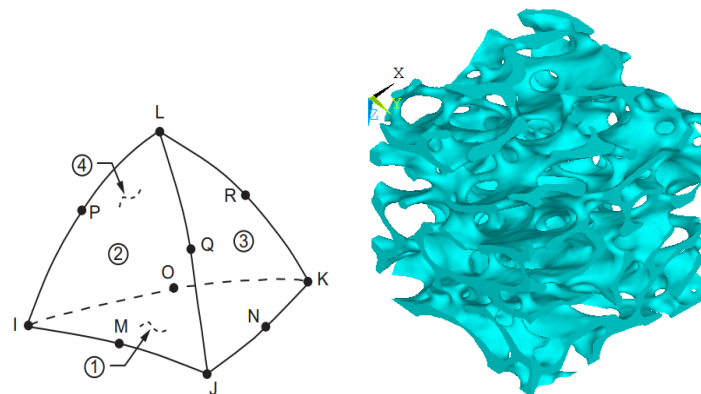
Fig.1.4. *Ten-node tetrahedral element and its FE model of cancellous bone tissue*

Alternatively, 3D tetrahedral mesh can be used. Especially with cancellous bone tissue, where the geometry changes sharply and a complex stress gradient is expected, both a smoothed geometry representation and more complicated displacement field element need to be used (Polgar et al., 2001; Viceconti, 2000). Studies have shown that the high order 10-node tetrahedral element allows more accurate strain field representation than lower order 4-node tetrahedral element and therefore remains a more preferable choice when modelling bone tissue with smoothed geometry (Polgar et al., 2001). Such element is defined by ten nodes having three DOFs at each node: translation in nodal X, Y and Z directions (Fig.1.4). The element has quadratic displacement behaviour and is well suited to modelling irregular meshes. With ten nodes, ten shape functions can be described and five Gauss integration points are necessary for numerical integration. Studies have shown that such models are able to predict apparent ultimate stress and strain at failure validated against experiments (Hambli, 2013). However, generation

tetrahedral mesh of bone tissue may not be a trivial task; one often has to achieve the balance between the accurate geometry and acceptable element shape and distortion. So even with automatic mesh generation implemented within some commercial software, for each specimen with specific micro-structure, it involves trials and errors to check the mesh quality and the generation of such models requires long processing time.

1.1.3. Formulation of three-dimensional elasticity

After the system has been partitioned, the governing equations for each element are calculated and then assembled back to provide system equations. Once the general format of the equation of an element is set, it becomes a matter of substituting the spatial coordinates of nodes, material properties of each element, and the boundary conditions. The following demonstration takes simplex 4-node tetrahedron elements as an example.

The displacement of a 3D element (e) takes the form of:

$$\{u^{(e)}\} = [N^{(e)}]\{U^{(e)}\} \tag{1.1}$$

where $\{U^{(e)}\}$ contains the unknown displacements of each node, $[N^{(e)}]$ the shape function of a certain element, which has the general form for a simplex element as:

$$N_\beta^{(e)} = (a_\beta + b_\beta x + c_\beta y + d_\beta z)/6V \qquad \beta = i, j, k, l \tag{1.2}$$

where $a_\beta, b_\beta, c_\beta, d_\beta$ are constants related to the coordinates of each node, V the volume of the element.

The $[B^{(e)}]$ matrix is the derivative of the shape function matrix $[N^{(e)}]$ and it relates the strain and displacement in the form of:

$$\begin{Bmatrix} \varepsilon_x \\ \varepsilon_y \\ \varepsilon_z \\ \gamma_{xy} \\ \gamma_{yz} \\ \gamma_{zx} \end{Bmatrix} = [B^{(e)}]\{U^{(e)}\} \tag{1.3}$$

The material property matrix $[D^{(e)}]$ for an isotropic material is:

$$[D^{(e)}] = \frac{E}{(1+v)(1-2v)}\begin{bmatrix} 1-v & v & v & 0 & 0 & 0 \\ v & 1-v & v & 0 & 0 & 0 \\ v & v & 1-v & 0 & 0 & 0 \\ 0 & 0 & 0 & \frac{1-2v}{2} & 0 & 0 \\ 0 & 0 & 0 & 0 & \frac{1-2v}{v} & 0 \\ 0 & 0 & 0 & 0 & 0 & \frac{1-2v}{v} \end{bmatrix}$$
(1.4)

where E is the Young's modulus of the element and v the Poisson's ratio.

The stiffness matrix $[K^{(e)}]$ can then be calculated using:

$$[K^{(e)}] = \int_V [B^{(e)}]^T [D^{(e)}][B^{(e)}]dV = [B^{(e)}]^T [D^{(e)}][B^{(e)}]$$
(1.5)

The force vector takes the form of:

$$\{F^{(e)}\} = \{T^{(e)}\} + \{b^{(e)}\} + \{S^{(e)}\} + \{P^{(e)}\}$$
(1.6)

where $\{T^{(e)}\}$ is the thermal expansion, $\{b^{(e)}\}$ the body force, $\{S^{(e)}\}$ the pressure on sides of the element, $\{P^{(e)}\}$ nodal force, $\{F^{(e)}\}$ the total force of the element.

When a structure in a loading condition reaches an equilibrium state, the potential energy of the system Π must be a minimum, which is defined as:

$$\frac{\partial \Pi}{\partial \{U\}} = 0$$
(1.7)

where

$$\Pi = \Lambda - W$$
(1.8)

Λ is the strain energy and W is the work done by external load defined as

$$W = \{U\}^T \{F\}$$
(1.9)

This minimization gives:

$$\sum_{e=1}^{E}([K^{(e)}]\{U^{(e)}\} - \{F^{(e)}\}) = 0$$
(1.10)

7

where $[K^e]$ is the element stiffness matrix, $\{U^e\}$ is the element unknown displacement, $\{F^e\}$ the element force vector, E the total number of elements

Finally, after assembling back the contribution of each element, it gives the general finite element equation as:

$$[K]\{U\} = \{F\} \tag{1.11}$$

where $[K]$ is the system stiffness matrix, $\{U\}$ is the unknown nodal displacement of the whole system, $\{F\}$ the force vector applied to the system.

After the unknown displacement vector $\{U\}$ has been solved, the strain vector can be calculated using equation 1.3 and the stress will be calculated simply using:

$$\{\sigma^e\} = [E^e]\{\varepsilon^e\} \tag{1.12}$$

1.1.4. Principal stress and strain

In solid mechanics, the normal strains at a point can reach its maximum/minimum at certain directions with reference of the global coordinate system, where the shear strain is zero. The maximum/minimum normal strains are called principal strains, a parameter essential for materials using strain failure criterion (Beer et al., 2006).

The principal strains are the eigenvalues of the strain tensor. These can be calculated from the following determinant equation:

$$\begin{vmatrix} \varepsilon_x - \varepsilon_o & \frac{1}{2}\varepsilon_{xy} & \frac{1}{2}\varepsilon_{xz} \\ \frac{1}{2}\varepsilon_{xy} & \varepsilon_y - \varepsilon_o & \frac{1}{2}\varepsilon_{yz} \\ \frac{1}{2}\varepsilon_{xz} & \frac{1}{2}\varepsilon_{yz} & \varepsilon_z - \varepsilon_o \end{vmatrix} = 0 \tag{1.13}$$

The three principal strains are labelled ε_{11}, ε_{22} and ε_{33}, ordered as ε_{11} the most positive (in tension), and ε_{33} the most negative (in compression) in a normal uniaxial loading condition.

Similarly, the principal stresses (σ_{11}, σ_{22} and σ_{33}) are calculated from the stress components by the determinant equation:

$$\begin{vmatrix} \sigma_x - \sigma_o & \sigma_{xy} & \sigma_{xz} \\ \sigma_{xy} & \sigma_y - \sigma_o & \sigma_{yz} \\ \sigma_{xz} & \sigma_{yz} & \sigma_z - \sigma_o \end{vmatrix} = 0 \tag{1.14}$$

The three principal stresses are labelled σ_{11}, σ_{22} and σ_{33}, ordered as σ_{11} the most positive (tensile), and σ_{33} the most negative (compressive) in a normal uniaxial loading condition.

1.1.5. Nonlinear finite element approach

In linear elastic finite element analysis, the problem to be solved can be described as equation 1.11.

This equation corresponds to a linear analysis, as we assumed only small displacement in the system and the material property is linear elastic. Further, we assumed that the boundary condition remains unchanged during the load application in the simulation. All these make the stiffness matrix $[K]$ constant and the displacement vector $\{U\}$ is propotional to the external force vector $\{F\}$. In nonlinear simulation however, the stiffness matrix $[K]$ doesn't remain constant anymore, either due to geometrical effect or the nonlinear constitutive equation used. Rather, the stiffness matrix becomes $[K^t]$, a tangent stiffness matrix, corresponding to geometric and material properties at time t.

Therefore, a classic approach to solve a nonlinear system is to gradually increase the load in steps, where we assume to know the solution for the time step t, and the solution for the time step $t + \Delta t$ is to be calculated, where Δt is a small time increment. We can write:

$$\{F^{t+\Delta t}\} = \{F^t\} + \{\dot{F}\} \tag{1.15}$$

where $\{\dot{F}\}$ denotes the increment in nodal force corresponding to the increment in element displacement and stress from time t to time $t + \Delta t$.

In each time step, we solve the equation:

$$[K^t]\{\dot{U}\} = \{\dot{F}\} \tag{1.16}$$

where $\{\dot{U}\}$ is the incremental nodal displacement vector.

A common way to solve the above equation is the classic Newton-Raphson iteration, which states that with the incremental nodal displacement $\{\dot{U}\}$ calculated, the incremental solution can be repeated using the currently known displacement rather than the displacement at time step t.

For iteration step i, it becomes:

$$[K_{i-1}^{t+\Delta t}]\{\Delta U_i\} = \{F_{i-1}^{t+\Delta t}\} \tag{1.17}$$

$$\{U_i^{t+\Delta t}\} = \{U_{i-1}^{t+\Delta t}\} + \{\Delta U_i\} \tag{1.18}$$

In each iteration, a solution $\{U_{i-1}^{t+\Delta t}\}$ is considered within tolerance moves on to the next sub-step, once the largest unbalance force $\{F_{i-1}^{t+\Delta t}\}$ at any node is lower than a use defined value (usually by default 10^{-4} times the largest force applied in some commercial FEA software such as ANSYS).

1.1.6. Verification and validation of FEA

In every modelling procedure, we come up with a conceptual model first by gathering the information of the real object, which will be later on transferred to a mathematical model. By employing proper method such as FEA, complex mathematical model can be solved (Fig.1.5). By taking certain assumptions, FE model is only a simplified version of the real object and the solution can provide no more information than what is contained in the mathematical model (Bathe, 1996). Therefore, verification and validation (V&V) in FEA has become a major focus for people wanting to control the quality of their engineering solutions. V&V are processes where evidence and credits are gathered showing that numerically predicted results by a model is sufficiently accurate for its purpose (Anderson et al., 2007; ASME, 2006). If we are going to use a numerical model to make any prediction useful to us, we need to know what the level of accuracy of the model is and decide if this accuracy is acceptable (Bathe, 1996; Fagan, 1992; Viceconti, 2012).

Verification is the process of determining if a model implementation accurately represents the conceptual description and solution to the model (Bathe, 1996). In the context of FEA, the verification of a model often relates to understanding its discretization error – the error committed in the solution due to insufficient mesh density (Shah, 2002). The foundation of FEA is taking a problem domain governed by differential equations and partitioning it into elements with pre-defined field variable behaviour. These series of partitions should strive to map, as closely as possible, the real continuous solution. However in a field problem, derived results such as stress and strain from each element do not necessarily be continuous from one element to the next.

This discontinuity is called discretization error and it goes to zero with the increasing number of elements of the system representing as close as possible the true continuous
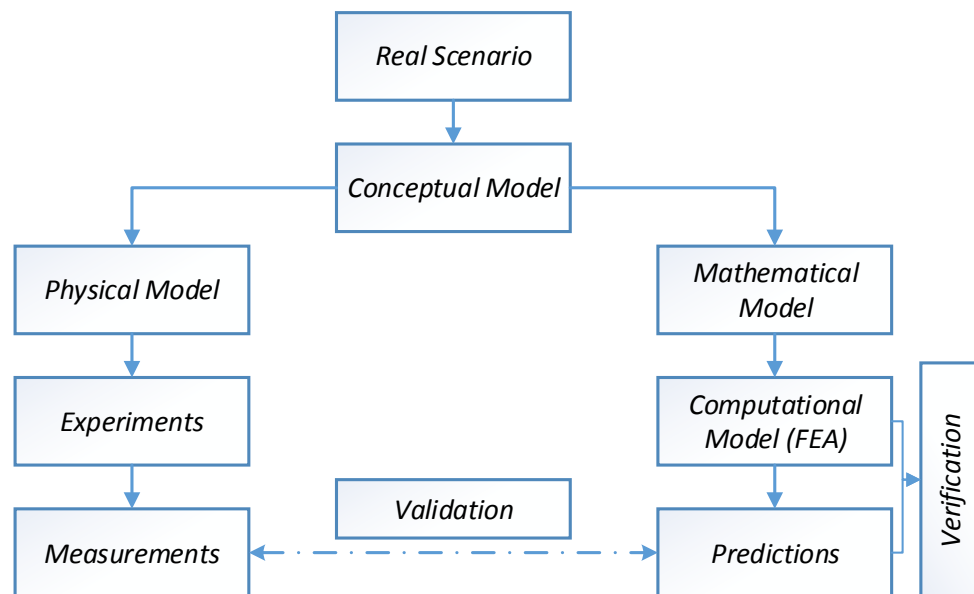
Fig.1.5. *Verification and validation of a standard modelling procedure*

system. As stated by Burnett (1987): "If a model satisfies the completeness and continuity conditions, the energy of the entire model will converge the exact solution as the size of the elements are decreased and in a well-posed problem, convergence of energy will also results in convergence of a particular local results in the model." Therefore the most straightforward way of verifying a finite element model is to generate different mesh refinements and conduct a convergence study (Viceconti, 2012). Bruce Irons first proposed the Patch Test in 1965 from a physical perspective (Irons and Loikkanen, 1983). But only in 2001 the Patch Test was proved sufficient for the convergence of nonconforming FE models provided some approximation and weak continuity are satisfied (Wang, 2001). A reliable patch test requires all the nodes that exist in the coarsest mesh also exist in other mesh refinements, and the peak values at nodes with fixed spatial position are investigated. Models with decreasing mesh size will be solved and the predicted results should converge monotonically to the exact solution. Furthermore, in a convergence study, the investigations on lower order results such as strains are preferred since in a region characterized by a rapidly changing strain field, a converged mesh measured by displacement may not satisfy the same convergence criterion for the strain (Bathe, 1996; Viceconti, 2012).

Validation is a process by which computational predictions are compared to experimental data (the 'gold standard') in an effort to assess the modelling error (Anderson et al., 2007; Anderson et al., 2005). In other words, validation procedure checks if the numerical model predicts accurately the physical phenomenon it was designed to replicate (Fig.1.5). If the validation shows large inconsistency between the model prediction and the experiments, one should always go back to check the error sources. Assuming an accurate experimental measurements and the model has been verified (acceptable numerical error), the mathematical representation of the physical problem of the system might not be adequate. One should then check if there are some inconsistencies regarding geometry, boundary conditions, material properties between the model and the real object.

1.2. The biomechanics of bone tissue

1.2.1. Bone anatomy and tissue scale classification

Bone is a living tissue that makes up the body's skeleton. In gross anatomy, bone can be described as organ providing supportive and protective function of the body, as well as enabling mobility (Cowin, 2001). It also serves as a mineral reservoir for calcium and phosphorus, which must be maintained within narrow limits in blood for muscles and nerves to function normally (Omi and Ezawa, 2001).

According to the classic Gray's anatomy, bones are classified as axial, appendicular and auditory by their location in the body or categorised as long, short, flat by their shape. Another classification, dependent on how lamellae are organised, categorises bone tissue as compact and cancellous. However, it is worthwhile mentioning that this difference between compact and cancellous bone is purely histological. Bone tissue is a composite material which mainly consists of a complex texture of collagen fibres that is gradually mineralized by crystals of hydroxyapatite ($Ca_{10}(PO_4)_6(OH)_2$) (Cowin, 2001; Viceconti, 2012). It is only when we observe the bone tissue using micro-tomography imaging technique (Bouxsein et al., 2010), that we can recognise and discriminate compact bone from cancellous bone by their location, structure and porosity. Such classification can often be observed in long bones such as femur (Fig.1.6), where a wall of lamellae covers the outer surface with little porosity, called compact bone. Approximately 75% of an adult human skeletal mass is cortical bone, which is largely responsible for supportive and protective functions. On the other hand, at the internal

region of bones where the porosity of bone becomes higher, trabeculae are formed by networks of tiny packages called lamellae shaped as either rod or plate (Fig.1.2 and Fig.1.6). Because of the sponge like structure of the three-dimensional trabeculae network, trabecular bone is also referred to as spongy bone or cancellous bone elsewhere (Viceconti, 2012). Such porous structure allows loading transmission and therefore plays an important role in energy absorption in some major parts such as knee, hip and spine (Silva and Gibson, 1997).
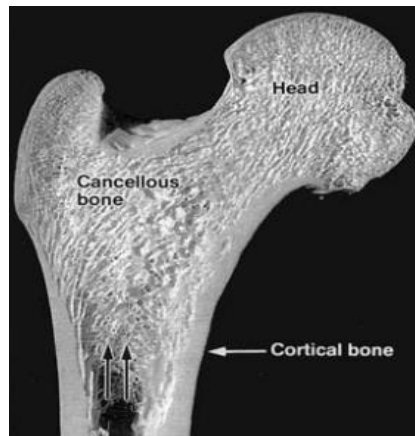
Fig.1.6. *Compact and cancellous tissue of proximal end of femur (From Weiss, L., Cell and Tissue Biology, A Textbook of Histology, Urban and Schwarzenberg, Baltimore, 1988)*

In this thesis, we mainly focused on the biomechanics of cancellous bone tissue, and to be consistent the word ''cancellous'' is used throughout the following text.

1.2.2. Mechanical properties of cancellous bone tissue

Cancellous bone plays a major load-bearing role in the human skeleton, with both its spongy-like structure and mineralisation distribution contributing to the mechanical properties (Bourne and van der Meulen, 2004; Renders et al., 2011; Ulrich et al., 1998; van der Linden et al., 2001; van Rietbergen et al., 1995; van Ruijven et al., 2007). Depending on anatomical site, age as well as pathologies, the morphology of cancellous bone tissue can be different. Compared to cortical bones, cancellous bone tissue has higher surface to mass ratio, which makes it less stiff but more flexible. The high porosity existing in cancellous bone makes proper reservoirs of red bone marrow, mainly haematopoietic stem cells capable of differentiating into all blood cell types (Cowin, 2001). Therefore cancellous bone is more sensitive to adaptation and remodelling, a homeostatic process where the mature bone is resorbed by osteoclasts

(bone resorbing cells) and new bone is generated by osteoblasts (bone forming cells) (Del Fattore et al., 2012). Lining cells covering the surface of the bone are former
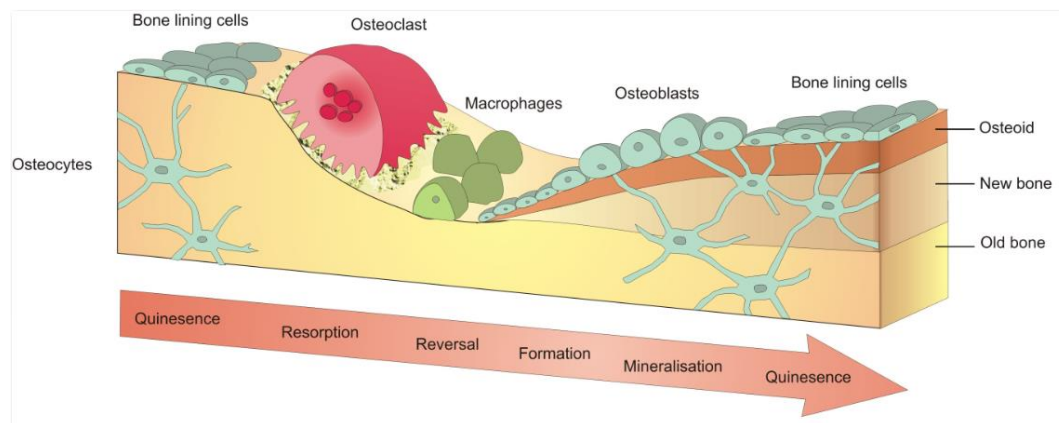
Fig.1.7. *Bone cells in remodelling process (From Bone from Blood, Biomedical Tissue Research, University of York, http://www.york.ac.uk/res/bonefromblood.html)*

osteoblasts and are responsible for regulating the calcium homeostasis in the blood. The complicated network of osteocytes allows them to contact each other and to the lining cells on the bone surface. By sensing the mechanical strain, osteocytes will activate the lining cells in forming the osteoblast thus directing the bone remodelling (Fig.1.7). Such processes control the reshaping of the bone according to its loading history and also the replacement of old bones tissue due to micro-damage. As there is conclusive evidence showing that bone is constantly remodelled, thus each volume of tissue might have a different level of mineralisation and consequently exhibits significantly difference mechanical properties (Gross et al., 2012; Renders et al., 2008). As a matter of fact, at the surface of trabeculae, where the remodelling process predominates, relatively younger bone with lower degree of mineralisation (DMB) is found while more mature and denser tissue is observed towards the core of trabeculae (Roschger et al., 2003).

1.2.3. Advantages of FEA in tissue scale modelling of bone tissue

Mechanical testing is the most straightforward way to evaluate cancellous bone mechanical properties at the apparent level. Like any other traditional materials, tensile testing (Keaveny et al., 1994; Lambers et al., 2014), compressive testing (Chen and McKittrick, 2011; Urban et al., 2004) and torsion testing (Bruyere Garnier et al., 1999) can be applied to cancellous bone tissue. Indentation test can also be used to measure cancellous bone indentation modulus (Sumner et al., 1994; Zysset, 2009). While such

experiments can be used for all cadaver bones, yet it becomes a limitation when we try to trace and evaluate the mechanical properties of bones *in vivo* because of the invasive and destructive nature of these experiments. Moreover, tissue scale is the scale where the interaction between mechanical stimuli and biological function become most evident, from which more on the biomechanics of bone tissue can be investigated (Viceconti, 2012). However, the mechanical strain that a single bone cell senses is the mechanical strain at the spatial scale of the cell itself (10-100 µm) (Cowin, 2001), which is difficult to measure using experiment measurements. Therefore, it is important to numerically quantify the stresses and strains at the tissue level and to better understand the biomechanics under certain loading conditions.

Pioneered by Feldkamp et al. (1989), microCT uses a polychromatic X-ray tube and a cone beam reconstruction algorithm to create 3D object with a typical resolution of 10µm or even smaller (Bouxsein et al., 2010). This imaging system allows a detailed examination of 3D structures of bone tissue and can be used both *in vivo* on small rodents (Laperre et al., 2011) and *ex vivo* on cadaver bones (Feldkamp et al., 1989; Issever et al., 2003; Patel et al., 2003). Since its first application in 1992 (Fyhrie et al., 1992), the microFE method has become a popular tool for non-destructive structural analysis of cancellous bone tissue (Hollister et al., 1994; van Rietbergen et al., 1995; Verhulp et al., 2008). As microCT imaging has the ability to accurately resolve bone morphology in great detail, specimen-specific microFE models that represent the structure of the specimen can be generated (Ulrich et al., 1998). For years, microFEs shows a great potential in studying biomechanics of bone tissue. Linear microFE models are able to predict around 80% of variance in experiment modulus and stress of cancellous bone samples (Hou et al., 1998; Yeni and Fyhrie, 2001) and is also feasible in tracking changes in mechanical properties *in vivo* (Liebschner et al., 2003; van Rietbergen et al., 2002). Nevertheless, numerically predicted bone apparent properties (e.g. stiffness, strength) of such models have also shown good correlation with accurate experiment measurements (Christen et al., 2013; Pistoia et al., 2002; Wolfram et al., 2010; Yeni and Fyhrie, 2001). Therefore, microFE model, with its non-destructive characteristics and its ability to accurately predict mechanical properties of bone tissue is a popular tool in in studying bone biomechanics at the tissue scale. It can also help us understanding better the interaction between bone mechanical stimuli and the biological function driven by the cell activity.

1.2.4. Important factors in modelling bone tissue

As discussed in section 1.1.6, a FE model is only a simplified version of the real object and the solution can never provide more information but only strive to approximate as possible the reality. Therefore, when preforming a modelling work, some critical factors must be reflected in the model and treated with caution, such as structural geometry, material properties and boundary conditions (BC).

One of the most traditional modelling approaches based on microCT image datasets is voxel conversion technique (Hollister et al., 1994; van Rietbergen et al., 1995), which takes Cartesian approximation of the bone geometry. Because of its jagged surface, the reasonable geometry representation can only be achieved by decreasing the element size, leading to a large number of DOFs (10 to 100 millions) (Chen et al., 2014). Consequently, simulations of such model are highly computationally expensive and sometimes with low prediction accuracy on the bone surface (Depalle et al., 2012). Alternatively, boundary recovery mesh generation can be used. Such models consist of tetrahedral elements and therefore guarantees smoothed surfaces. In addition, when modelling cancellous bone tissue, where the geometry changes sharply and a complex stress gradient is expected, higher order tetrahedral elements are recommended (Muller and Ruegsegger, 1995; Polgar et al., 2001). As the generation of tetrahedral model produces elements of varying sizes and may locally have distorted elements, such meshes of good quality normally requires longer processing time (for details please refer to 1.1.2).

Bone tissue is a composite material made up of collagen and inorganic mineralized matrix. Because of the complicated microstructure and material properties, bone's linear elastic regime is limited to a small strain and in general shows nonlinearities due to its rate dependency and its plastic deformation and damage behaviour (Cowin, 2001). When subjected to gentle loading conditions such as slow walking or stair climbing, bone tissue will mostly stay in elastic regime and therefore the error induced in modelling bone tissue as purely linear elastic is very small and maybe acceptable (Viceconti, 2012). Linear microFE have been shown not only to predict the modulus and strength of cancellous bone tissue (Hou et al., 1998; Yeni and Fyhrie, 2001), but also to adequately predict the failure of bone tissue (Pistoia et al., 2002). By assuming that bone failure start when a significant part of the tissue was strained beyond a critical

limit, they found the failure predicted by the linear FE model well correlated with experiments. However, they also concluded that prediction could be further improved by including post-yield behaviour. Therefore to accurately predict bone yield strength, nonlinear FE model instead of pure linear elastic models has been proposed (Bayraktar et al., 2004; MacNeil and Boyd, 2008). Some suggested a simple elastic-perfectly-plastic constitutive equation to avoid the error induced by some local area having started to deform plastically while the rest of the tissue still behaves as elastic (Viceconti, 2012). More complicated formulations including finite plasticity, strain rate dependent plastic behaviour or perfect damage model have also been proposed (Kosmopoulos et al., 2008; Natali et al., 2008; Pankaj, 2013; Wallace et al., 2013). Furthermore, there is conclusive evidence that bone is constantly remodelled (Currey, 1999), thus each volume of tissue might have a different level of mineralisation and consequently exhibit significantly different mechanical properties. While the effect of bone lamellae heterogeneity on the apparent mechanical properties of cancellous bone tissue has been investigated by some studies (Gross et al., 2012; Jaasma et al., 2002; Kaynia et al., 2015; Renders et al., 2008; van der Linden et al., 2001), little is known about the effect of heterogeneity on the local mechanical behaviour (displacement, stress and strain) (Renders et al., 2011). There are potentially infinite local configurations that could provide the same results at the apparent level, thus the issue requires further investigation.

In every modelling study, especially ones with validations, the boundary conditions imposed in the model should be as close as possible as in the experiments (Hao et al., 2011; Kallemeyn et al., 2006; Zauel et al., 2006). Depending on different BCs, the biomechanical behaviour observed from a specific model can be significantly different (Hao et al., 2011). Further, in some cases where the experimental protocol is complex (such as *in situ* mechanical testing within a microCT scanner), it is not trivial to control them during the tests and it becomes very hard to accurately replicate them into the models. Therefore, numerical results predicted by microFE models simulated under different BCs should be explored and compared with proper experimental measurements.

Last but not least, at the tissue scale, while the predicted apparent properties (e.g. stiffness, strength) of the numerical models can be compared with accurate experimental measurements (Christen et al., 2013; Pistoia et al., 2002; Wolfram et al., 2010; Yeni and Fyhrie, 2001), the validation of such models for local predictions is not trivial. In fact,

there are potentially infinite local configurations that could provide the same results at the apparent level. Fortunately, elastic registration or digital volume correlation (DVC) combined with high resolution microCT scanning has been recently applied to bone for filling this gap (Grassi and Isaksson, 2015; Roberts et al., 2014). In particular, this method can be applied to undeformed and deformed microCT images of the same specimen in order to estimate the local mechanical behaviour of cancellous bone tissue under certain loading conditions (Bay et al., 1999; Dall'Ara et al., 2014; Gillard et al., 2014; Liu and Morgan, 2007). Therefore, this approach can measure 3D volumetric displacement and strain fields within the specimen, making possible the validation of microFE model for local prediction (Zauel et al., 2006). Attentions should be taken that when a novel technique such as DVC is applied for validation of microFE models, it is important to test its applicability for different independent experimental setups and cross different specimens in order to evaluate the robustness of the method. For the validation methods, please refer to Chapter 3 for more details.

1.3. References

Anderson, A.E., Ellis, B.J., Weiss, J.A., 2007. Verification, validation and sensitivity studies in computational biomechanics. Computer methods in biomechanics and biomedical engineering 10, 171-184.

Anderson, A.E., Peters, C.L., Tuttle, B.D., Weiss, J.A., 2005. Subject-specific finite element model of the pelvis: development, validation and sensitivity studies. J. Biomech. Eng. 127, 364-373.

ASME, C., 2006. Verification and Validation in Computational Solid Mechanics Guide for verification and validation in computational solid mechanics.

Bathe, K.-J.r., 1996. Finite element procedures. Prentice Hall, Englewood Cliffs, N.J.

Bay, B.K., Smith, T.S., Fyhrie, D.P., Saad, M., 1999. Digital volume correlation: Three-dimensional strain mapping using X-ray tomography. Exp Mech 39, 217-226.

Bayraktar, H.H., Gupta, A., Kwon, R.Y., Papadopoulos, P., Keaveny, T.M., 2004. The modified super-ellipsoid yield criterion for human trabecular bone. J. Biomech. Eng. 126, 677-684.

Beer, F.P., Johnston, E.R., DeWolf, J.T., 2006. Mechanics of materials, 4th ed. McGraw-Hill Higher Education, Boston.

Bourne, B.C., van der Meulen, M.C., 2004. Finite element models predict cancellous apparent modulus when tissue modulus is scaled from specimen CT-attenuation. J. Biomech. 37, 613-621.

Bouxsein, M.L., Boyd, S.K., Christiansen, B.A., Guldberg, R.E., Jepsen, K.J., Muller, R., 2010. Guidelines for assessment of bone microstructure in rodents using micro-computed tomography. J. Bone Miner. Res. 25, 1468-1486.

Brekelmans, W.A., Poort, H.W., Slooff, T.J., 1972. A new method to analyse the mechanical behaviour of skeletal parts. Acta Orthop. Scand. 43, 301-317.

Bruyere Garnier, K., Dumas, R., Rumelhart, C., Arlot, M.E., 1999. Mechanical characterization in shear of human femoral cancellous bone: torsion and shear tests. Med. Eng. Phys. 21, 641-649.

Burnett, D.S., 1987. Finite element analysis : from concepts to applications. Addison-Wesley Pub. Co., Reading, Mass.

Chen, P.Y., McKittrick, J., 2011. Compressive mechanical properties of demineralized and deproteinized cancellous bone. Journal of the mechanical behavior of biomedical materials 4, 961-973.

Chen, Y., Pani, M., Taddei, F., Mazza, C., Li, X., Viceconti, M., 2014. Large-scale finite element analysis of human cancellous bone tissue micro computer tomography data: a convergence study. J. Biomech. Eng. 136.

Christen, D., Melton, L.J., 3rd, Zwahlen, A., Amin, S., Khosla, S., Muller, R., 2013. Improved fracture risk assessment based on nonlinear micro-finite element simulations from HRpQCT images at the distal radius. J. Bone Miner. Res. 28, 2601-2608.

Cowin, S.C., 2001. Bone mechanics handbook, 2nd ed. CRC, Boca Raton, Fla. ; London.

Currey, J.D., 1999. What determines the bending strength of compact bone? J. Exp. Biol. 202, 2495-2503.

Dall'Ara, E., Barber, D., Viceconti, M., 2014. About the inevitable compromise between spatial resolution and accuracy of strain measurement for bone tissue: a 3D zero-strain study. J. Biomech. 47, 2956-2963.

Del Fattore, A., Teti, A., Rucci, N., 2012. Bone cells and the mechanisms of bone remodelling. Front Biosci (Elite Ed) 4, 2302-2321.

Depalle, B., Chapurlat, R., Walter-Le-Berre, H., Bou-Said, B., Follet, H., 2012. Finite element dependence of stress evaluation for human trabecular bone. Journal of the mechanical behavior of biomedical materials 18, 200-212.

Fagan, M.J., 1992. Finite element analysis : theory and practice. Longman Scientific & Technical;Wiley, Harlow, Essex, England.

Feldkamp, L.A., Goldstein, S.A., Parfitt, A.M., Jesion, G., Kleerekoper, M., 1989. The direct examination of three-dimensional bone architecture in vitro by computed tomography. J. Bone Miner. Res. 4, 3-11.

Fyhrie, D.P., Hamid, M.S., Kuo, R.F., Lang, S.M., 1992. Direct three-dimensinal finite element analysis of human vertebral cancellous bone. Trans. 38th Meeting Orthopaedic Research Society, 551.

Gillard, F., Boardman, R., Mavrogordato, M., Hollis, D., Sinclair, I., Pierron, F., Browne, M., 2014. The application of digital volume correlation (DVC) to study the microstructural behaviour of trabecular bone during compression. Journal of the mechanical behavior of biomedical materials 29, 480-499.

Grassi, L., Isaksson, H., 2015. Extracting accurate strain measurements in bone mechanics: A critical review of current methods. Journal of the mechanical behavior of biomedical materials 50, 43-54.

Gross, T., Pahr, D.H., Peyrin, F., Zysset, P.K., 2012. Mineral heterogeneity has a minor influence on the apparent elastic properties of human cancellous bone: a SRmuCT-based finite element study. Computer methods in biomechanics and biomedical engineering 15, 1137-1144.

Hambli, R., 2013. Micro-CT finite element model and experimental validation of trabecular bone damage and fracture. Bone 56, 363-374.

Hao, Z., Wan, C., Gao, X., Ji, T., 2011. The effect of boundary condition on the biomechanics of a human pelvic joint under an axial compressive load: a three-dimensional finite element model. J. Biomech. Eng. 133, 101006.

Hollister, S.J., Brennan, J.M., Kikuchi, N., 1994. A homogenization sampling procedure for calculating trabecular bone effective stiffness and tissue level stress. J. Biomech. 27, 433-444.

Hou, F.J., Lang, S.M., Hoshaw, S.J., Reimann, D.A., Fyhrie, D.P., 1998. Human vertebral body apparent and hard tissue stiffness. J. Biomech. 31, 1009-1015.

Huiskes, R., Hollister, S.J., 1993. From structure to process, from organ to cell: recent developments of FE-analysis in orthopaedic biomechanics. J. Biomech. Eng. 115, 520-527.

Irons, B., Loikkanen, M., 1983. An Engineers Defense of the Patch Test. Int J Numer Meth Eng 19, 1391-1401.

Issever, A.S., Burghardt, A., Patel, V., Laib, A., Lu, Y., Ries, M., Majumdar, S., 2003. A micro-computed tomography study of the trabecular bone structure in the femoral head. J. Musculoskelet. Neuronal Interact. 3, 176-184.

Jaasma, M.J., Bayraktar, H.H., Niebur, G.L., Keaveny, T.M., 2002. Biomechanical effects of intraspecimen variations in tissue modulus for trabecular bone. J. Biomech. 35, 237-246.

Kallemeyn, N.A., Grosland, N.M., Pedersen, D.R., Martin, J.A., Brown, T.D., 2006. Loading and boundary condition influences in a poroelastic finite element model of cartilage stresses in a triaxial compression bioreactor. Iowa Orthop. J. 26, 5-16.

Kaynia, N., Soohoo, E., Keaveny, T.M., Kazakia, G.J., 2015. Effect of intraspecimen spatial variation in tissue mineral density on the apparent stiffness of trabecular bone. J. Biomech. Eng. 137.

Keaveny, T.M., Wachtel, E.F., Ford, C.M., Hayes, W.C., 1994. Differences between the tensile and compressive strengths of bovine tibial trabecular bone depend on modulus. J. Biomech. 27, 1137-1146.

Kosmopoulos, V., Schizas, C., Keller, T.S., 2008. Modeling the onset and propagation of trabecular bone microdamage during low-cycle fatigue. J. Biomech. 41, 515-522.

Lambers, F.M., Bouman, A.R., Tkachenko, E.V., Keaveny, T.M., Hernandez, C.J., 2014. The effects of tensile-compressive loading mode and microarchitecture on microdamage in human vertebral cancellous bone. J. Biomech. 47, 3605-3612.

Laperre, K., Depypere, M., van Gastel, N., Torrekens, S., Moermans, K., Bogaerts, R., Maes, F., Carmeliet, G., 2011. Development of micro-CT protocols for in vivo follow-up of mouse bone architecture without major radiation side effects. Bone 49, 613-622.

Liebschner, M.A., Kopperdahl, D.L., Rosenberg, W.S., Keaveny, T.M., 2003. Finite element modeling of the human thoracolumbar spine. Spine 28, 559-565.

Liu, L., Morgan, E.F., 2007. Accuracy and precision of digital volume correlation in quantifying displacements and strains in trabecular bone. J. Biomech. 40, 3516-3520.

MacNeil, J.A., Boyd, S.K., 2008. Bone strength at the distal radius can be estimated from high-resolution peripheral quantitative computed tomography and the finite element method. Bone 42, 1203-1213.

Muller, R., Ruegsegger, P., 1995. Three-dimensional finite element modelling of non-invasively assessed trabecular bone structures. Med. Eng. Phys. 17, 126-133.

Natali, A.N., Carniel, E.L., Pavan, P.G., 2008. Investigation of bone inelastic response in interaction phenomena with dental implants. Dent. Mater. 24, 561-569.

Omi, N., Ezawa, I., 2001. Change in calcium balance and bone mineral density during pregnancy in female rats. J. Nutr. Sci. Vitaminol. (Tokyo) 47, 195-200.

Pankaj, P., 2013. Patient-specific modelling of bone and bone-implant systems: the challenges. International journal for numerical methods in biomedical engineering 29, 233-249.

Patel, V., Issever, A.S., Burghardt, A., Laib, A., Ries, M., Majumdar, S., 2003. MicroCT evaluation of normal and osteoarthritic bone structure in human knee specimens. J. Orthop. Res. 21, 6-13.

Pistoia, W., van Rietbergen, B., Lochmuller, E.M., Lill, C.A., Eckstein, F., Ruegsegger, P., 2002. Estimation of distal radius failure load with micro-finite element analysis models based on three-dimensional peripheral quantitative computed tomography images. Bone 30, 842-848.

Pointer, J., 2004. Understanding Accuracy and Discretization Error in an FEA Model. ANSYS 7.1, 2004 Conference.

Polgar, K., Viceconti, M., O'Connor, J.J., 2001. A comparison between automatically generated linear and parabolic tetrahedra when used to mesh a human femur. Proc. Inst. Mech. Eng. H 215, 85-94.

Renders, G.A., Mulder, L., Langenbach, G.E., van Ruijven, L.J., van Eijden, T.M., 2008. Biomechanical effect of mineral heterogeneity in trabecular bone. J. Biomech. 41, 2793-2798.

Renders, G.A., Mulder, L., van Ruijven, L.J., Langenbach, G.E., van Eijden, T.M., 2011. Mineral heterogeneity affects predictions of intratrabecular stress and strain. J. Biomech. 44, 402-407.

Roberts, B.C., Perilli, E., Reynolds, K.J., 2014. Application of the digital volume correlation technique for the measurement of displacement and strain fields in bone: a literature review. J. Biomech. 47, 923-934.

Roschger, P., Gupta, H.S., Berzlanovich, A., Ittner, G., Dempster, D.W., Fratzl, P., Cosman, F., Parisien, M., Lindsay, R., Nieves, J.W., Klaushofer, K., 2003. Constant mineralization density distribution in cancellous human bone. Bone 32, 316-323.

Shah, C., 2002. Mesh Discretization Error and Criteria for Accuracy of Finite Element Solutions. Ansys Users Conference, Pittsburgh, PA.

Silva, M.J., Gibson, L.J., 1997. Modeling the mechanical behavior of vertebral trabecular bone: effects of age-related changes in microstructure. Bone 21, 191-199.

Sumner, D.R., Willke, T.L., Berzins, A., Turner, T.M., 1994. Distribution of Young's modulus in the cancellous bone of the proximal canine tibia. J. Biomech. 27, 1095-1099.

Ulrich, D., van Rietbergen, B., Weinans, H., Ruegsegger, P., 1998. Finite element analysis of trabecular bone structure: a comparison of image-based meshing techniques. J. Biomech. 31, 1187-1192.

Urban, R.M., Turner, T.M., Hall, D.J., Infanger, S.I., Cheema, N., Lim, T.H., Moseley, J., Carroll, M., Roark, M., 2004. Effects of altered crystalline structure and increased initial compressive strength of calcium sulfate bone graft substitute pellets on new bone formation. Orthopedics 27, s113-118.

van der Linden, J.C., Birkenhager-Frenkel, D.H., Verhaar, J.A., Weinans, H., 2001. Trabecular bone's mechanical properties are affected by its non-uniform mineral distribution. J. Biomech. 34, 1573-1580.

van Rietbergen, B., 2001. Micro-FE analyses of bone: state of the art. Adv. Exp. Med. Biol. 496, 21-30.

van Rietbergen, B., Majumdar, S., Newitt, D., MacDonald, B., 2002. High-resolution MRI and micro-FE for the evaluation of changes in bone mechanical properties during longitudinal clinical trials: application to calcaneal bone in postmenopausal women after one year of idoxifene treatment. Clin. Biomech. (Bristol, Avon) 17, 81-88.

van Rietbergen, B., Weinans, H., Huiskes, R., Odgaard, A., 1995. A new method to determine trabecular bone elastic properties and loading using micromechanical finite-element models. J. Biomech. 28, 69-81.

van Ruijven, L.J., Mulder, L., van Eijden, T.M., 2007. Variations in mineralization affect the stress and strain distributions in cortical and trabecular bone. J. Biomech. 40, 1211-1218.

Verhulp, E., van Rietbergen, B., Muller, R., Huiskes, R., 2008. Indirect determination of trabecular bone effective tissue failure properties using micro-finite element simulations. J. Biomech. 41, 1479-1485.

Viceconti, M., 2000. A comparative study on different methods of automatic mesh generation of human femurs. Medical Engineering and Physics 20 (1998): 1-10. Med. Eng. Phys. 22, 379-380.

Viceconti, M., 2012. Multiscale modeling of the skeletal system. Cambridge University Press, Cambridge.

Wallace, R.J., Pankaj, P., Simpson, A.H., 2013. The effect of strain rate on the failure stress and toughness of bone of different mineral densities. J. Biomech. 46, 2283-2287.

Wang, M., 2001. On the Necessity and Sufficiency of the Patch Test for Convergence of Nonconforming Finite Elements. Journal on Numerical Analysis 39, 363-384.

Wolfram, U., Wilke, H.J., Zysset, P.K., 2010. Valid micro finite element models of vertebral trabecular bone can be obtained using tissue properties measured with nanoindentation under wet conditions. J. Biomech. 43, 1731-1737.

Yeni, Y.N., Fyhrie, D.P., 2001. Finite element calculated uniaxial apparent stiffness is a consistent predictor of uniaxial apparent strength in human vertebral cancellous bone tested with different boundary conditions. J. Biomech. 34, 1649-1654.

Zauel, R., Yeni, Y.N., Bay, B.K., Dong, X.N., Fyhrie, D.P., 2006. Comparison of the linear finite element prediction of deformation and strain of human cancellous bone to 3D digital volume correlation measurements. J. Biomech. Eng. 128, 1-6.

Zysset, P.K., 2009. Indentation of bone tissue: a short review. Osteoporos. Int. 20, 1049-1055.

Chapter2

Motivation and relevant literature review

Summary

This chapter addresses the need for a microCT-based computational tool that takes into account the bone geometry and material properties than DXA, a traditional clinical practice in assessing bone fracture risk caused by osteoporosis. It also reviews the key aspects in generating, verifying and validating such computational models, which introduces the aim of the PhD project: to conduct a systematic convergence study of microFE models of cancellous bone tissue using different mesh generation techniques; to validate models' local mechanical property prediction using the DVC measurement; most importantly, when a novel technique such as DVC is used for validation, to test its capability by using difference specimens on different independent experimental setups.

2.1. The motivation of microFE analysis of bone tissue

Osteoporosis is a systemic skeletal disease characterized by a reduction of bone mass and deterioration of bone microstructure (Borah et al., 2001; Kanis and Johnell, 2005; Kim et al., 2009; Sedlak et al., 2007). It causes bones to become weak and fragile, and therefore more sensitive to fracture from falling or overloading. It is reported that approximately 22 million women and 5.5 million men aged between 50 to 84 are estimated to have osteoporosis in Europe and the total number is expected to increase to 33.9 million by 2025 (Hernlund et al., 2013). The osteoporotic fractures can have a huge impact on the patient, leading to substantial pain, disability and even premature mortality, especially for elderly people (Edwards et al., 2015; Kanis et al., 2015). It is a large and growing concern for public health, and has drawn a lot of attentions on the research and treatment of the disease. Correspondingly, the finical burden is high: the cost of osteoporosis, including pharmacological intervention in Europe in 2010 alone was estimated at € 37 billion (Hernlund et al., 2013; Strom et al., 2011).

In traditional clinical practice, bone fracture risk is assessed using dual-energy X-ray absorptiometry (DXA) by evaluating the bone quality based on its density (Brask-Lindemann et al., 2011; Salehi-Abari, 2015). However, the skeletal competence is not only determined by the bone mineral density, but also by its microstructure (Ulrich et al., 1999), the information which cannot be provided by DXA. Therefore it becomes obvious the need of a modelling tool which has the potential to provide more information than DXA by including subject-specific structure of the bone tissue. With the development of high resolution computed tomography technology combined with finite element technique, specimen-specific microFE model can be generated, which has the potential to fill the gap. The majority of clinical studies in the literature have focused on in vivo high-resolution peripheral quantitative computed tomography (HRpQCT), which scans typically a 9 mm cross-section of the peripheral sites such as distal radius or tibia at 82 μm (Varga et al., 2010). Using such data in microFE analysis makes a way to assess human bone strength more directly (Christen et al., 2013; Cody et al., 1999; Pistoia et al., 2001; Vilayphiou et al., 2011). Studies have shown that HRpQCT-based models better predicts the bone strength and have done at least as good as DXA in predicting bone fracture risk. A thorough review of HRpQCT based microFE model analysis for clinical assessment of bone strength can be found in (van Rietbergen and Ito, 2015). However, considering the trabecular thickness (Tb.Th) even for young human

group (186 ± 29 μm, 16-39 years, N = 40) (Ding and Hvid, 2000), the spatial resolution of 82 μm may not adequately reflect the structure of the cancellous bone tissue. Correspondingly, the HRpQCT-based microFE often exhibits overestimated bone volume (using threshold such that the structural indices calculated from HRpQCT best correlated to those obtained from microCT (Laib and Ruegsegger, 1999)) which leads to an overestimation of the bone stiffness and strength (Liu et al., 2010). On the other hand, the scanning of microCT can be performed *ex vivo* or on biopsies (Chen et al., 2014; Renders et al., 2008) of human or *in vivo* on small rodents (Ravoori et al., 2010). Moreover, the higher resolution of microCT (typically 10 μm or even smaller) makes possible a thorough investigation of the bone at the tissue scale, where the interaction between mechanical stimuli and biological function becomes most evident. Therefore, for a better understanding of the underlying structural and systematic changes caused by certain bone diseases and how they are related to bone failure, there is a need for numerical simulations using microCT-based model to assess the local mechanical properties of the bone tissue.

2.2. Literature review

2.2.1. Convergence behaviour of cancellous bone microFE

Over the years, researchers have investigated the relationship between the mechanical properties of trabecular bones and the optimal element size of the microFE models. In a study exploring the relationship between image resolution and meshing techniques for trabecular bones, Ulrich et al. (1998) found that Cartesian meshes with a resolution of 168 μm taken from the femoral head produced the best results, compared against models of 28 μm as reference (a minor decrease of 3% in the elastic modulus and 9% in tissue stress were found). A recent study conducted by Torcasio et al. (2012) aimed at validating specimen-specific micro FE models for the assessment of bone strains in the rat tibia under compression showed that Cartesian models of 40 μm and 80 μm converged with a difference in stiffness of 1.30% and 1.35% respectively compared with the reference model of 20 μm. Depalle et al. (2012) showed that at the tissue level, the increase in element size affects the local stress distribution during a compression test simulation. Both stiffening and global softening due to discretisation errors caused fluctuation in local stress values compared to the theoretical value. They also found that numerical stiffening errors occurred when trabecular thickness was close to element size,

especially when there were less than three elements across the cross-section. This was in agreement with van Rietbergen (2001) who reported that convergence could be obtained in linear simulation when the ratio of mean trabecular thickness over element size is greater than four. Nevertheless, different bone types, the voxel conversion routines, image modalities and the various complicated loading conditions all add extra complexity on bone's convergence behaviour (van Rietbergen, 2001). Thus, the convergence behaviour of models may differ from case to case.

Previous convergence studies were mostly conducted over the apparent properties (Ulrich et al., 1998; van Rietbergen et al., 1998; van Rietbergen et al., 1995; Yeni et al., 2005), whereas only a limited number of studies investigated convergence at the local values (Niebur et al., 1999; Torcasio et al., 2012). Bone tissue is found to yield at around 7000 microstrain (Bayraktar et al., 2004; Niebur et al., 2000; Pistoia et al., 2002). However, the mechanical strain that a single bone cell senses is the mechanical strain at the spatial scale of the cell itself, i.e. 10-100 microns (Cowin, 2001; Viceconti, 2012). Therefore before we can start to explore bone mechanobiology, we need to be able to quantify mechanical stresses and strains of the bone tissue at such a fine scale. In practice the voxels of reconstructed images may be subsampled to generate coarser microFE models in order to reduce computational cost. In these coarse models, small areas with high mineral content may not be accurately reproduced, which lead to an underestimation of the CT attenuation due to averaging (Gross et al., 2012; Homminga et al., 2001; Ulrich et al., 1998). This would further reduce the accuracy of the results. Therefore, convergence study should be performed routinely with large-scale microFE analysis in order to choose a proper voxel size that does not lead to substantial loss of trabecular information, subsequently affecting the predicted results.

2.2.2. Effect of lamellae heterogeneity on the biomechanics of cancellous bone tissue

Cancellous bone plays a major load-bearing role in the human skeleton, with both its spongy-like structure and mineralisation distribution contributing to the mechanical properties (Bourne and van der Meulen, 2004; Renders et al., 2011; Ulrich et al., 1998; van der Linden et al., 2001; van Rietbergen et al., 1995; van Ruijven et al., 2007). Because of this, two types of bone heterogeneity can be defined. At the organ level, bone is represented as a heterogeneous continuum, whose heterogeneity comes from the large macro-pores (Currey, 1988; Morgan et al., 2003; Zannoni et al., 1998). At the

organ level, the term bone mineral density (BMD) is normally used (Lai et al., 2005), which is the average density of a well-defined volume that contains a mixture of both bone and soft tissue. This parameter relates to the amount of bone within a mixed bone-soft tissue region , but does not give information about the material density itself; at the tissue level, where the tissue porosities are represented explicitly, the heterogeneity emerges from the different local mineralisation due to the constant remodelling process (Fig.2.1) (Currey, 1999). In this case, the term tissue mineral density (TMD) is used (Gross et al., 2012; Renders et al., 2008), which is a measurement of bone density within the pure volume of calcified bone tissue. By contrast to BMD, the TMD provides us the information abo ut the material density of the bone itself and ignores the surrounding soft tissue. In our study, we focused on the effect of bone heterogeneity driven at the tissue level, and the term TMD is used throughout the thesis.

The mechanical property of cancellous bone tissue is both affected by its structure and the degree of mineralisation. In the early studies, most authors neglect the latter and used only the homogeneous FE models (Huiskes and Hollister, 1993; Jaecques et al., 2004; Niebur et al., 2000; Ulrich et al., 1998; van Rietbergen, 2001; van Rietbergen et al., 1995). However, bone tissues are not homogeneous due to constant remodelling (Currey, 1988; Ruffoni et al., 2007). Due to the improvement of computationnal power and imaging technique, more recent studies used density-based microFE model where the element material properties are distributed from the greyscale of the voxels and suggested such models could lead to more accurate prediction of the bone mechanical behaviour (Bourne and van der Meulen, 2004; Harrison et al., 2008; Renders et al., 2008; Renders et al., 2011).
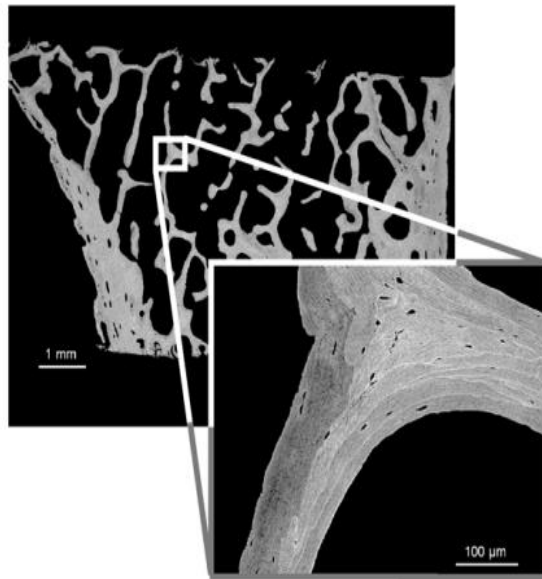
Fig.2.1. *Backscattered electron image of transiliac bone biopsy. Dark gray means low mineral content, light gray high mineral content. Adapted from (Ruffoni et al., 2007)*

Amongst the non-destructive methods to evaluate the bone local heterogneneity, synchrotron radiation micro-computed tomography (SRµCT) is currently found to be the most accurate approach and therefore referred to as the gold standard of this type of measurement (Carter et al., 2013; Kazakia et al., 2008). SRµCT imaging is performed using relativistic electrons accelerated by a magnetic field (Cowin, 2001; Takeda et al., 1994). The beam is normally equipped with a monochromator to create a specific narrow energy incident beam. Therefore the mono-energetic, high flux, parallel beam used in SRµCT produces high resolution, high signal-to-noise ratio, and accurate attenuation measurement, which is free of beam hardening artefact seen in microCT (Kazakia et al., 2008; Nuzzo et al., 2002). By using SRµCT, Gross et al. (2012) found only a minor underestimation (2.19 ± 0.78%) of the apparent stiffness when bone heterogeneity was taken into account, indicating that neglecting bone heterogeneity in cancellous microFE models had only a minor effect on the apparent elastic properties of bone tissue. This is in agreement in a more recent finding, where Kaynia et al. (2015) confirmed that by including local heterogeneity in the model, it results in an underestimation of the apparent modulus for both microCT and SRµCT based microFE models. But this difference is higher in microCT based models (underestimated by 14%) than SRµCT based models (underestimated by 9%), because of microCT imaging artifacts.

Although having the ability to accurately access the TMD over microCT, SRμCT scanners in general are less available. Alternatively, most of the studies were conducted using microCT (Bourne and van der Meulen, 2004; Harrison et al., 2008; Renders et al., 2008; Renders et al., 2011; van Ruijven et al., 2007) van der Linden et al. (2001) used a hypothetical mineral distribution of cancellous bone tissue. They found a higher apparent stiffness of the major load-bearing direction (superior–inferior) compared to homogeneous models. This difference was up to 20% when a cubic relationship between tissue modulus and calcium concentration was assumed. Bourne and van der Meulen (2004) found that the predicted apparent modulus of heterogeneous microFE models was significantly lower than that of homogeneous models assuming a tissue modulus of 20 GPa and the role of bone heterogeneity became more important with the increasing mineral distribution variability. Specifically, by increasing the bone mineralisation variation to 16%, 26% and 34%, approximately 26%, 35% and 43% reductions in the predicted apparent stiffness of the heterogeneous models were obtained, respectively. Using nano-indentation to determine the local tissue moduli, Harrison et al. (2008), reported a very good agreement of mean apparent modulus between the experiments and the numerical results from heterogeneous FE models, which were 1.65±0.20 GPa and 1.64±0.32 GPa respectively. Renders et al. (2008) found in human mandibular condyles, although the bone volume fraction (BV/TV) has more influence (up to 82%) on the apparent moduli than TMD (29%), the TMD still plays an important role in the mechanical property of cancellous bone tissue and the apparent moduli of the homogeneous models were overestimated by 20% on average compared to that of the heterogeneous models.

While most of the above-mentioned studies aimed to investigate the effect of bone heterogeneity on the apparent properties of cancellous bones, a few studies focused on the local stresses and strains (Renders et al., 2011; van Ruijven et al., 2007). van Ruijven et al. (2007) showed that the assumption of homogeneity in microFE models of human mandibular cancellous bone yielded lower mean strains (up to 70%) compared to the heterogeneous models. Renders et al. (2011) found the predicted patterns of stress and strain were more consistent with the expected biomechanical behaviour of the cancellous bone tissue when bone heterogeneity was incorporated. In their study, a significant increase in stress with increasing distance from trabecular surface was found

followed by a significant decrease towards the core, which reflected the bending state of the rod-like trabeculae.

Moreover, all the above-mentioned studies failed to validate the approach against in vitro experiments; instead the confirmations were carried out between computational models. Before we can jump to the conclusion claiming which type of model is more representitive and accurate, proper experimental measurements of the modelling specimen are needed.

2.2.3. Validation approaches of microFE models

Although showing a great potential of studying biomechanics of cancellous bone at the tissue level, as discussed in section 1.2.3 and 2.1, microFE models, presented as mathematical equations, are simplified version of the real subjects. Therefore, it becomes fundamental to validate those models before drawing any useful conclusions (Cristofolini et al., 2010; Viceconti et al., 2005).

The predicted apparent properties (e.g. stiffness, strength) of each specimen can be compared with accurate experimental measurements in many ways (Christen et al., 2013; Pistoia et al., 2002; Wolfram et al., 2010; Yeni and Fyhrie, 2001). Using Quasi-static compression load setup combined with extensometer, the force displacement curve of the mechanical test can be measured and the ultimate apparent stress, strain and strength can be calculated (Hambli, 2013; Imai, 2015). To simulate a fall on an outstretched hand, Pistoia et al. (2002) used an Instron uniaxial-driven mechanical testing machine to record the force displacement curve and the bone failure load can be obtained. A custom-made stepwise loading device mounted in a high resolution peripheral computer tomography system, allows better understanding of the progressive collapse of trabecular bone and the failure of cortical shell (Hosseini et al., 2014). Using a special designed mechanical setup with infrared markers to simulate the femur on a side fall, the failure location of the femur can be determined (Dall'Ara et al., 2013).

Among all the possible mechanical parameters of bone tissue that can be measured using experimental approach, strain is the most critical one because of the failure criteria heavily used in the literature (Bayraktar et al., 2004; Niebur et al., 2000; Pistoia et al., 2002). Yet, measuring strains on bone tissue is not trivial because of its complicated geometry. For years, the biomechanics community has developed different

technologies in measuring bone strain with increased accuracy and precision, each with its own pros and cons. At the organ level strain gauge (SG) has been intensively used in bone biomechanics as a gold standard because of its accuracy and high frequency response (Cristofolini et al., 2009; Kim et al., 2001; Ostbyhaug et al., 2009; Zani et al., 2015). It works by tracking the changes of the resistance of a metallic material under certain loading conditions. However, the SG can only measure the average strain over surfaces of limited area where they attach and consequently, this method is usually applied to long bones such as femur and cannot apply to porous materials like cancellous bone tissue (Cristofolini et al., 2009; Kim et al., 2001; Ostbyhaug et al., 2009; Zani et al., 2015). By mapping two digital images and calculating the displacement on the surface of the sample based on its transformation field (Grassi and Isaksson, 2015), digital image correlation (DIC) method has been applied to measure the full-field surface strain of bones (Amin Yavari et al., 2013; Dickinson et al., 2011). Due its non-contact nature, DIC are not restricted to a limited number of discrete strain measurements as SG. However, this method cannot be applied at the biopsy level, where there is limited space and 3D volumetric information becomes essential because of the complicated microstructure (Dall'Ara et al., 2014). In addition, the measurement accuracy of DIC can be affected by several factors, such as the size of subarea chosen to match the same point between two images, the step size and the type of data filter used. More often than not, the user need to go a long way in finding the balance between these parameters in order to achieve an optimal measurement of a sample, which requires both experience and trials (Sutton et al., 2009).

Yet, elastic registration or digital volume correlation (DVC) combined with high resolution microCT scanning has been recently applied to bone for measuring 3D volumetric displacement and strain fields within the specimen (Grassi and Isaksson, 2015; Roberts et al., 2014). This method can be applied to undeformed and deformed microCT images of the same specimen in order to estimate the local mechanical behavior of cancellous bone tissue under certain loading conditions (Fig.2.2) (Bay et al., 1999; Dall'Ara et al., 2014; Gillard et al., 2014; Liu and Morgan, 2007). Therefore, this approach can measure 3D volumetric displacement fields within the specimen, making possible the validation of microFE model for local prediction (Zauel et al., 2006)

Actually, there are a number of computational approaches for DVC to recognize the features between the undeformed and deformed images and to provide the displacement

and strain distribution. One approach, referred to as the global approach, is based on a method driven by the continuity assumption (Fig.2.2b) (Barber et al., 2007; Dall'Ara et al., 2014). In this method, the whole volume of interest is analyzed and the registration procedure focuses on the recognition of identical features from two reconstruction image datasets (undeformed and deformed images). Consequently, the problem can be translated by describing the mapping function which maps the coordinates *(x,y,z)* of a feature in undeformed images to the coordinates *(x',y',z')* of the same feature in the deformed images. These coordinate pairs are related through three displacement functions: *u(x,y,z), v(x,y,z)* and *w(x,y,z)* where *x' = u(x,y,z) + x; y' = v(x,y,z) + y; z' = w(x,y,z) + z*. Another approach, referred to as the local approach, begins by partitioning the image dataset into smaller sub-volumes, described as a discrete function of greyscales (Fig.2.2a). By using either Fourier space or direct coupling cross correlation to quantify the similarity between the images and a multi-pass approach that uses the displacement gradient from previous passes to deform the sub-volumes on the subsequent passes, the displacement at the center of each sub-volume can be retrieved (Madi et al., 2013). Then the strain measurements can be estimated from the displacement field using either center finite difference (CFD) scheme or finite element (FE) analysis (Palanca et al., 2015). In general, the global approach requires higher computational cost than the local approach, but results in lower displacement measurement error by imposing continuity assumption, such that the mapping of an individual subset depends on the mapping of the neighborhood (Madi et al., 2013; Palanca et al., 2015; Roberts et al., 2014). Furthermore, it should be noted that the precision and accuracy of the global approach are related to the chosen sub-sampling (i.e. a compromise should be taken between the accuracy and the spatial resolution of the experimental method, defined by the sub-volume chosen during the elastic registration of the un-deformed and deformed images) (Dall'Ara et al., 2014; Palanca et al., 2015). In particular, while the accuracy in computing the displacements is in the order of a fraction of voxel size, for the strain the errors can be in the order of hundreds of microstrain even for relatively large subsampling areas (e.g. 425±202 $\mu\varepsilon$ for subsampling areas of approximately 500 μm as reported by Palanca et al. (2015)). Therefore, while the experimental measurement for the displacement can be considered a true value when compared to microFE predictions, this assumption does not hold anymore for strain.
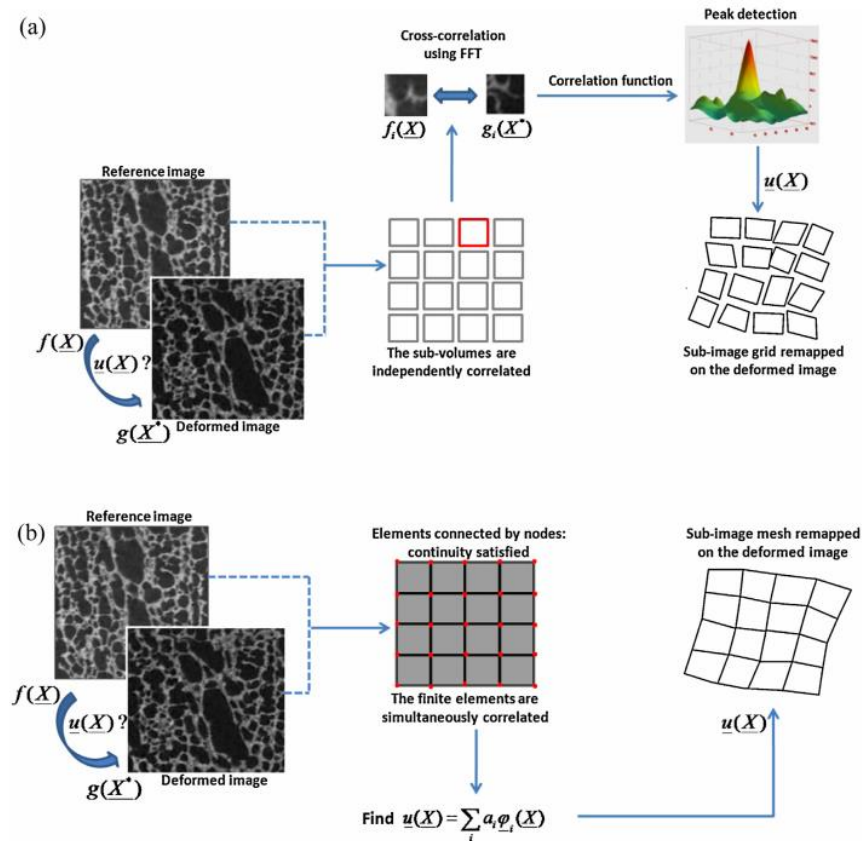
Fig.2.2. *Difference between local DVC approach (a) and global DVC approach (b). Adapted from (Madi et al., 2013)*

Last but not least, DVC as a novel technique may be affected by the initial image quality and by the external loading that is applied. Therefore when applied for validation of microFE models, it is important to test its applicability for different independent experimental setups and cross different specimens in order to evaluate the robustness of the method.

2.3. Aims of the study

The literature review shows that previous verification and validation studies (V&V) conducted on cancellous bone tissue were mostly done by considering apparent properties, whereas only a limited number of studies focused on the local values. This context draws heavily the need to V&V such microFEs models for their local mechanical properties at the tissue scale, which are essential for studying bone mechanobiology. Moreover, previous research indicated that incorporating the bone lamella heterogeneity or recovering smoothed boundary of microFE models is likely to affect the prediction of local cancellous bone mechanical properties. To the author's

knowledge there is no study that systematically investigated the effect of certain assumptions of modelling technique on the local mechanical properties of cancellous bone tissue validated with the state-of-art DVC approach. Therefore, the aims of this PhD project are:

- To conduct a systematic convergence study of cancellous bone microFEs generated using three different modelling methods: *homogenous hexahedral model:* traditional Cartesian mesh mostly used in the literature; *heterogeneous hexahedral model:* continuous Cartesian mesh which takes into account the local mineralization distribution of the bone tissue; *homogenous tetrahedral model:* boundary recovery mesh that allows for smoothed topology at trabecular surface.

- To validate displacement predicted by three different modelling methods against the state-of-art DVC approach, which provide a full-field 3D measurement of displacements of the sample. Further, to test the capability of the novel DVC technique, the study will be performed on two independent experimental setups and cross different specimens in order to evaluate the robustness of the method.

- As currently there is no experiment method to validate the strain at 10-20 μm level, typical element size used in microFE models. This sub-goal is to compare the strain fields predicted by different tissue modelling methods in order to explore the effect of specific idealizations/simplifications for each model type on the prediction of strains.

2.4. References

Amin Yavari, S., van der Stok, J., Weinans, H., Zadpoor, A.A., 2013. Full-field strain measurement and fracture analysis of rat femora in compression test. J. Biomech. 46, 1282-1292.

Barber, D.C., Oubel, E., Frangi, A.F., Hose, D.R., 2007. Efficient computational fluid dynamics mesh generation by image registration. Med. Image Anal. 11, 648-662.

Bay, B.K., Smith, T.S., Fyhrie, D.P., Saad, M., 1999. Digital volume correlation: Three-dimensional strain mapping using X-ray tomography. Exp Mech 39, 217-226.

Bayraktar, H.H., Morgan, E.F., Niebur, G.L., Morris, G.E., Wong, E.K., Keaveny, T.M., 2004. Comparison of the elastic and yield properties of human femoral trabecular and cortical bone tissue. J. Biomech. 37, 27-35.

Borah, B., Gross, G.J., Dufresne, T.E., Smith, T.S., Cockman, M.D., Chmielewski, P.A., Lundy, M.W., Hartke, J.R., Sod, E.W., 2001. Three-dimensional microimaging

(MRmicroI and microCT), finite element modeling, and rapid prototyping provide unique insights into bone architecture in osteoporosis. Anat. Rec. 265, 101-110.

Bourne, B.C., van der Meulen, M.C., 2004. Finite element models predict cancellous apparent modulus when tissue modulus is scaled from specimen CT-attenuation. J. Biomech. 37, 613-621.

Brask-Lindemann, D., Cadarette, S.M., Eskildsen, P., Abrahamsen, B., 2011. Osteoporosis pharmacotherapy following bone densitometry: importance of patient beliefs and understanding of DXA results. Osteoporos. Int. 22, 1493-1501.

Carter, Y., Thomas, C.D., Clement, J.G., Peele, A.G., Hannah, K., Cooper, D.M., 2013. Variation in osteocyte lacunar morphology and density in the human femur--a synchrotron radiation micro-CT study. Bone 52, 126-132.

Chen, Y., Pani, M., Taddei, F., Mazza, C., Li, X., Viceconti, M., 2014. Large-scale finite element analysis of human cancellous bone tissue micro computer tomography data: a convergence study. J. Biomech. Eng. 136.

Christen, D., Melton, L.J., 3rd, Zwahlen, A., Amin, S., Khosla, S., Muller, R., 2013. Improved fracture risk assessment based on nonlinear micro-finite element simulations from HRpQCT images at the distal radius. J. Bone Miner. Res. 28, 2601-2608.

Cody, D.D., Gross, G.J., Hou, F.J., Spencer, H.J., Goldstein, S.A., Fyhrie, D.P., 1999. Femoral strength is better predicted by finite element models than QCT and DXA. J. Biomech. 32, 1013-1020.

Cowin, S.C., 2001. Bone mechanics handbook, 2nd ed. CRC, Boca Raton, Fla. ; London.

Cristofolini, L., Juszczyk, M., Taddei, F., Viceconti, M., 2009. Strain distribution in the proximal human femoral metaphysis. Proc. Inst. Mech. Eng. H 223, 273-288.

Cristofolini, L., Schileo, E., Juszczyk, M., Taddei, F., Martelli, S., Viceconti, M., 2010. Mechanical testing of bones: the positive synergy of finite-element models and in vitro experiments. Philosophical transactions. Series A, Mathematical, physical, and engineering sciences 368, 2725-2763.

Currey, J.D., 1988. The effect of porosity and mineral content on the Young's modulus of elasticity of compact bone. J. Biomech. 21, 131-139.

Currey, J.D., 1999. What determines the bending strength of compact bone? J. Exp. Biol. 202, 2495-2503.

Dall'Ara, E., Barber, D., Viceconti, M., 2014. About the inevitable compromise between spatial resolution and accuracy of strain measurement for bone tissue: a 3D zero-strain study. J. Biomech. 47, 2956-2963.

Dall'Ara, E., Luisier, B., Schmidt, R., Kainberger, F., Zysset, P., Pahr, D., 2013. A nonlinear QCT-based finite element model validation study for the human femur tested in two configurations in vitro. Bone 52, 27-38.

Depalle, B., Chapurlat, R., Walter-Le-Berre, H., Bou-Said, B., Follet, H., 2012. Finite element dependence of stress evaluation for human trabecular bone. Journal of the mechanical behavior of biomedical materials 18, 200-212.

Dickinson, A.S., Taylor, A.C., Ozturk, H., Browne, M., 2011. Experimental validation of a finite element model of the proximal femur using digital image correlation and a composite bone model. J. Biomech. Eng. 133, 014504.

Ding, M., Hvid, I., 2000. Quantification of age-related changes in the structure model type and trabecular thickness of human tibial cancellous bone. Bone 26, 291-295.

Edwards, M.H., Dennison, E.M., Aihie Sayer, A., Fielding, R., Cooper, C., 2015. Osteoporosis and sarcopenia in older age. Bone 80, 126-130.

Gillard, F., Boardman, R., Mavrogordato, M., Hollis, D., Sinclair, I., Pierron, F., Browne, M., 2014. The application of digital volume correlation (DVC) to study the microstructural behaviour of trabecular bone during compression. Journal of the mechanical behavior of biomedical materials 29, 480-499.

Grassi, L., Isaksson, H., 2015. Extracting accurate strain measurements in bone mechanics: A critical review of current methods. Journal of the mechanical behavior of biomedical materials 50, 43-54.

Gross, T., Pahr, D.H., Peyrin, F., Zysset, P.K., 2012. Mineral heterogeneity has a minor influence on the apparent elastic properties of human cancellous bone: a SRmuCT-based finite element study. Computer methods in biomechanics and biomedical engineering 15, 1137-1144.

Hambli, R., 2013. Micro-CT finite element model and experimental validation of trabecular bone damage and fracture. Bone 56, 363-374.

Harrison, N.M., McDonnell, P.F., O'Mahoney, D.C., Kennedy, O.D., O'Brien, F.J., McHugh, P.E., 2008. Heterogeneous linear elastic trabecular bone modelling using micro-CT attenuation data and experimentally measured heterogeneous tissue properties. J. Biomech. 41, 2589-2596.

Hernlund, E., Svedbom, A., Ivergard, M., Compston, J., Cooper, C., Stenmark, J., McCloskey, E.V., Jonsson, B., Kanis, J.A., 2013. Osteoporosis in the European Union: medical management, epidemiology and economic burden. A report prepared in collaboration with the International Osteoporosis Foundation (IOF) and the European Federation of Pharmaceutical Industry Associations (EFPIA). Archives of osteoporosis 8, 136.

Homminga, J., Huiskes, R., Van Rietbergen, B., Ruegsegger, P., Weinans, H., 2001. Introduction and evaluation of a gray-value voxel conversion technique. J. Biomech. 34, 513-517.

Hosseini, H.S., Clouthier, A.L., Zysset, P.K., 2014. Experimental validation of finite element analysis of human vertebral collapse under large compressive strains. J. Biomech. Eng. 136.

Huiskes, R., Hollister, S.J., 1993. From structure to process, from organ to cell: recent developments of FE-analysis in orthopaedic biomechanics. J. Biomech. Eng. 115, 520-527.

Imai, K., 2015. Analysis of vertebral bone strength, fracture pattern, and fracture location: a validation study using a computed tomography-based nonlinear finite element analysis. Aging Dis. 6, 180-187.

Jaecques, S.V., Van Oosterwyck, H., Muraru, L., Van Cleynenbreugel, T., De Smet, E., Wevers, M., Naert, I., Vander Sloten, J., 2004. Individualised, micro CT-based finite element modelling as a tool for biomechanical analysis related to tissue engineering of bone. Biomaterials 25, 1683-1696.

Kanis, J.A., Johnell, O., 2005. Requirements for DXA for the management of osteoporosis in Europe. Osteoporos. Int. 16, 229-238.

Kanis, J.A., McCloskey, E.V., Harvey, N.C., Johansson, H., Leslie, W.D., 2015. Intervention Thresholds and the Diagnosis of Osteoporosis. J. Bone Miner. Res. 30, 1747-1753.

Kaynia, N., Soohoo, E., Keaveny, T.M., Kazakia, G.J., 2015. Effect of intraspecimen spatial variation in tissue mineral density on the apparent stiffness of trabecular bone. J. Biomech. Eng. 137.

Kazakia, G.J., Burghardt, A.J., Cheung, S., Majumdar, S., 2008. Assessment of bone tissue mineralization by conventional x-ray microcomputed tomography: comparison with synchrotron radiation microcomputed tomography and ash measurements. Med. Phys. 35, 3170-3179.

Kim, S.H., Suh, H.S., Cho, M.H., Lee, S.Y., Kim, T.S., 2009. Finite element simulation of ultrasound propagation in bone for quantitative ultrasound toward the diagnosis of osteoporosis. Conf. Proc. IEEE Eng. Med. Biol. Soc. 2009, 436-439.

Kim, Y.H., Kim, J.S., Cho, S.H., 2001. Strain distribution in the proximal human femur. An in vitro comparison in the intact femur and after insertion of reference and experimental femoral stems. J. Bone Joint Surg. Br. 83, 295-301.

Lai, Y.M., Qin, L., Yeung, H.Y., Lee, K.K., Chan, K.M., 2005. Regional differences in trabecular BMD and micro-architecture of weight-bearing bone under habitual gait loading--a pQCT and microCT study in human cadavers. Bone 37, 274-282.

Laib, A., Ruegsegger, P., 1999. Comparison of structure extraction methods for in vivo trabecular bone measurements. Comput. Med. Imaging Graph. 23, 69-74.

Liu, L., Morgan, E.F., 2007. Accuracy and precision of digital volume correlation in quantifying displacements and strains in trabecular bone. J. Biomech. 40, 3516-3520.

Liu, X.S., Zhang, X.H., Sekhon, K.K., Adams, M.F., McMahon, D.J., Bilezikian, J.P., Shane, E., Guo, X.E., 2010. High-resolution peripheral quantitative computed tomography can assess microstructural and mechanical properties of human distal tibial bone. J. Bone Miner. Res. 25, 746-756.

Madi, K., Tozzi, G., Zhang, Q.H., Tong, J., Cossey, A., Au, A., Hollis, D., Hild, F., 2013. Computation of full-field displacements in a scaffold implant using digital volume correlation and finite element analysis. Med. Eng. Phys. 35, 1298-1312.

Morgan, E.F., Bayraktar, H.H., Keaveny, T.M., 2003. Trabecular bone modulus-density relationships depend on anatomic site. J. Biomech. 36, 897-904.

Niebur, G.L., Feldstein, M.J., Yuen, J.C., Chen, T.J., Keaveny, T.M., 2000. High-resolution finite element models with tissue strength asymmetry accurately predict failure of trabecular bone. J. Biomech. 33, 1575-1583.

Niebur, G.L., Yuen, J.C., Hsia, A.C., Keaveny, T.M., 1999. Convergence behavior of high-resolution finite element models of trabecular bone. J. Biomech. Eng. 121, 629-635.

Nuzzo, S., Peyrin, F., Cloetens, P., Baruchel, J., Boivin, G., 2002. Quantification of the degree of mineralization of bone in three dimensions using synchrotron radiation microtomography. Med. Phys. 29, 2672-2681.

Ostbyhaug, P.O., Klaksvik, J., Romundstad, P., Aamodt, A., 2009. An in vitro study of the strain distribution in human femora with anatomical and customised femoral stems. J. Bone Joint Surg. Br. 91, 676-682.

Palanca, M., Tozzi, G., Cristofolini, L., Viceconti, M., Dall'Ara, E., 2015. Three-dimensional local measurements of bone strain and displacement: comparison of three digital volume correlation approaches. J. Biomech. Eng. 137.

Pistoia, W., van Rietbergen, B., Laib, A., Ruegsegger, P., 2001. High-resolution three-dimensional-pQCT images can be an adequate basis for in-vivo microFE analysis of bone. J. Biomech. Eng. 123, 176-183.

Pistoia, W., van Rietbergen, B., Lochmuller, E.M., Lill, C.A., Eckstein, F., Ruegsegger, P., 2002. Estimation of distal radius failure load with micro-finite element analysis models based on three-dimensional peripheral quantitative computed tomography images. Bone 30, 842-848.

Ravoori, M., Czaplinska, A.J., Sikes, C., Han, L., Johnson, E.M., Qiao, W., Ng, C., Cody, D.D., Murphy, W.A., Do, K.A., Navone, N.M., Kundra, V., 2010. Quantification of mineralized bone response to prostate cancer by noninvasive in vivo microCT and non-destructive ex vivo microCT and DXA in a mouse model. PLoS One 5, e9854.

Renders, G.A., Mulder, L., Langenbach, G.E., van Ruijven, L.J., van Eijden, T.M., 2008. Biomechanical effect of mineral heterogeneity in trabecular bone. J. Biomech. 41, 2793-2798.

Renders, G.A., Mulder, L., van Ruijven, L.J., Langenbach, G.E., van Eijden, T.M., 2011. Mineral heterogeneity affects predictions of intratrabecular stress and strain. J. Biomech. 44, 402-407.

Roberts, B.C., Perilli, E., Reynolds, K.J., 2014. Application of the digital volume correlation technique for the measurement of displacement and strain fields in bone: a literature review. J. Biomech. 47, 923-934.

Ruffoni, D., Fratzl, P., Roschger, P., Klaushofer, K., Weinkamer, R., 2007. The bone mineralization density distribution as a fingerprint of the mineralization process. Bone 40, 1308-1319.

Salehi-Abari, I., 2015. Early diagnosis of osteopenia/osteoporosis by bone mineral density test using DXA method in early adulthood. Int. J. Rheum. Dis.

Sedlak, C.A., Doheny, M.O., Estok, P.J., Zeller, R.A., Winchell, J., 2007. DXA, health beliefs, and osteoporosis prevention behaviors. J. Aging Health 19, 742-756.

Strom, O., Borgstrom, F., Kanis, J.A., Compston, J., Cooper, C., McCloskey, E.V., Jonsson, B., 2011. Osteoporosis: burden, health care provision and opportunities in the EU: a report prepared in collaboration with the International Osteoporosis Foundation (IOF) and the European Federation of Pharmaceutical Industry Associations (EFPIA). Archives of osteoporosis 6, 59-155.

Sutton, M.A., Orteu, J.-J., Schreier, H.W., 2009. Image correlation for shape, motion and deformation measurements : basic concepts, theory and applications. Springer, New York, N.Y.

Takeda, T., Itai, Y., Hayashi, K., Nagata, Y., Yamaji, H., Hyodo, K., 1994. High spatial resolution CT with a synchrotron radiation system. J. Comput. Assist. Tomogr. 18, 98-101.

Torcasio, A., Zhang, X., Duyck, J., van Lenthe, G.H., 2012. 3D characterization of bone strains in the rat tibia loading model. Biomechanics and modeling in mechanobiology 11, 403-410.

Ulrich, D., van Rietbergen, B., Laib, A., Ruegsegger, P., 1999. The ability of three-dimensional structural indices to reflect mechanical aspects of trabecular bone. Bone 25, 55-60.

Ulrich, D., van Rietbergen, B., Weinans, H., Ruegsegger, P., 1998. Finite element analysis of trabecular bone structure: a comparison of image-based meshing techniques. J. Biomech. 31, 1187-1192.

van der Linden, J.C., Birkenhager-Frenkel, D.H., Verhaar, J.A., Weinans, H., 2001. Trabecular bone's mechanical properties are affected by its non-uniform mineral distribution. J. Biomech. 34, 1573-1580.

van Rietbergen, B., 2001. Micro-FE analyses of bone: state of the art. Adv. Exp. Med. Biol. 496, 21-30.

van Rietbergen, B., Ito, K., 2015. A survey of micro-finite element analysis for clinical assessment of bone strength: the first decade. J. Biomech. 48, 832-841.

van Rietbergen, B., Majumdar, S., Pistoia, W., Newitt, D.C., Kothari, M., Laib, A., Ruegsegger, P., 1998. Assessment of cancellous bone mechanical properties from micro-FE models based on micro-CT, pQCT and MR images. Technol. Health Care 6, 413-420.

van Rietbergen, B., Weinans, H., Huiskes, R., Odgaard, A., 1995. A new method to determine trabecular bone elastic properties and loading using micromechanical finite-element models. J. Biomech. 28, 69-81.

van Ruijven, L.J., Mulder, L., van Eijden, T.M., 2007. Variations in mineralization affect the stress and strain distributions in cortical and trabecular bone. J. Biomech. 40, 1211-1218.

Varga, P., Pahr, D.H., Baumbach, S., Zysset, P.K., 2010. HR-pQCT based FE analysis of the most distal radius section provides an improved prediction of Colles' fracture load in vitro. Bone 47, 982-988.

Viceconti, M., 2012. Multiscale modeling of the skeletal system. Cambridge University Press, Cambridge.

Viceconti, M., Olsen, S., Nolte, L.P., Burton, K., 2005. Extracting clinically relevant data from finite element simulations. Clin. Biomech. (Bristol, Avon) 20, 451-454.

Vilayphiou, N., Boutroy, S., Szulc, P., van Rietbergen, B., Munoz, F., Delmas, P.D., Chapurlat, R., 2011. Finite element analysis performed on radius and tibia HR-pQCT images and fragility fractures at all sites in men. J. Bone Miner. Res. 26, 965-973.

Wolfram, U., Wilke, H.J., Zysset, P.K., 2010. Valid micro finite element models of vertebral trabecular bone can be obtained using tissue properties measured with nanoindentation under wet conditions. J. Biomech. 43, 1731-1737.

Yeni, Y.N., Christopherson, G.T., Dong, X.N., Kim, D.G., Fyhrie, D.P., 2005. Effect of microcomputed tomography voxel size on the finite element model accuracy for human cancellous bone. J. Biomech. Eng. 127, 1-8.

Yeni, Y.N., Fyhrie, D.P., 2001. Finite element calculated uniaxial apparent stiffness is a consistent predictor of uniaxial apparent strength in human vertebral cancellous bone tested with different boundary conditions. J. Biomech. 34, 1649-1654.

Zani, L., Erani, P., Grassi, L., Taddei, F., Cristofolini, L., 2015. Strain distribution in the proximal Human femur during in vitro simulated sideways fall. J. Biomech. 48, 2130-2143.

Zannoni, C., Mantovani, R., Viceconti, M., 1998. Material properties assignment to finite element models of bone structures: a new method. Med. Eng. Phys. 20, 735-740.

Zauel, R., Yeni, Y.N., Bay, B.K., Dong, X.N., Fyhrie, D.P., 2006. Comparison of the linear finite element prediction of deformation and strain of human cancellous bone to 3D digital volume correlation measurements. J. Biomech. Eng. 128, 1-6.

Chapter3

Bone specimens' preparation and mechanical testing

Summary

In parallel to the development of this PhD thesis, Dr Enrico Dall'Ara and his team developed a robust experimental method, based on Digital Volume Correlation, capable of accurately quantifying the displacement field of a specimen of bone tissue subjected to static compression. With this method the results of three experiments where analysed, one conducted by Dr Dall'Ara at the Insigneo institute for in silico medicine of the University of Sheffield, and the other two by Drs Sales, Manda, Wallace, and Pankaj at the Institute for Bioengineering, University of Edinburgh. The resulting displacement fields were made available to the author, and used extensively in this thesis.

While such experimental work is not part of this thesis, its results were essential for the validation study (chapter 5), and reflected also, in the choice of the boundary conditions, in the verification study (chapter 4). Thus, we thought it was necessary to provide here a detailed description of the experimental methods used to collect the measurements used in the following of this thesis. However, it is important to stress that this experimental work was not part of my PhD project, and its author did not contribute in any way to it.

The chapter describes the materials and methods of the compression experiments, the DVC analysis, and some limitations in the specimens' preparation that became evident when the displacement data were analysed. We also discuss how we defined the boundary conditions for our models so as to accurately replicate the experimental conditions.

3.1. Specimen preparation and scanning

All procedures on human tissue were performed with the approval from the Research Ethics Committee for use of discarded bone material (LREC 2002/1/22). Animal tissue was extracted from a bovine femur, collected from animal that was killed for alimentary purposes. Two cylindrical cancellous bone specimens (Specimen1: height equal to 13.2 mm, diameter equal to 10.6mm; Specimen2: height equal to 11.5 mm, diameter equal to 10.6mm) were extracted from the central part of two human femoral heads from patients who underwent total hip replacement. Specimen 1 was extracted from an osteoarthritic male aged 68 and Specimen 2 from a 94 years old male without any known musculoskeletal pathologies. The specimens were extracted by using diamond-tipped cores (Starlite Indistries, Rosemount PA, USA), and the ends of the core samples were cut parallel using a Buehler Isomet low speed saw (Buehler, Illinois, USA). The third specimen (Specimen3: height equal to 11.88 mm, diameter equal to 7.89 mm) was drilled (diamond core drill with nominal internal diameter equal to 8mm mounted on a pillar drilling machine, GDM50B, Sealey, UK) from a bone slice cut (0.2 mm diamond band saw mounted on a 300 CP, Exakt Gmbh, Germany) from a bovine femoral greater trochanter (female, 18 months old). All operations were performed under constant water irrigation in order to reduce potential damage to be bone specimen. The specimens were scanned with a microCT (Skyscan 1172; Specimen1 and Specimen2: voxel size 17.22 µm, 54 kV, 185 µA, 0.5 mm aluminium filter, exposure time 885 ms, no averaging; Specimen3: voxel size 9.92 µm, 59 kV, 169 µA, 1 mm aluminium filter, exposure time 1180 ms, averaged by two frames). Each image was cropped in order to include only the bone specimens and datasets were subsampled by a factor of two (ImageJ, V1.50a), resulting in a new voxel size equal to 34.44 µm and 19.84 µm for human and bovine specimens, respectively. For the Specimen1 and Specimen2 top and bottom slices with partial bone and air were removed, while for Specimen3 slices in the embedding material were removed. Bone volume fraction (BV/TV), trabecular thickness (Tb.Th), trabecular spacing (Tb.Sp), degree of anisotropy (DA) and angle between the main trabecular direction and the loading axis (α.Z) were computed with the ImageJ plugin BoneJ (Doube et al., 2010). Information for all specimens was summarized in Table.3.1.

Table.3.1. *Specimens' information*

Specimen	Species	Location	Height (mm)	Diameter (mm)	BV/TV (%)	Tb.Th (μm)	Tb.Sp (μm)	DA (-)	α.Z (deg°)	Voxel size (μm)	Force (N)	Disp (mm)
Specimen 1	Human	Femoral head	13.2	10.6	30.29	192 ± 69	427 ± 193	0.571	27	17.22	42	0.13
Specimen 2	Human	Femoral head	11.5	10.6	29.64	188 ± 67	376 ± 160	0.594	9	17.22	162	0.12
Specimen 3	Bovine	Greater trochanter	11.88	7.89	22.82	171 ± 51	550 ± 152	0.539	60	9.92	120	Na

Na: no displacement was measured and this type of BCs was not modelled
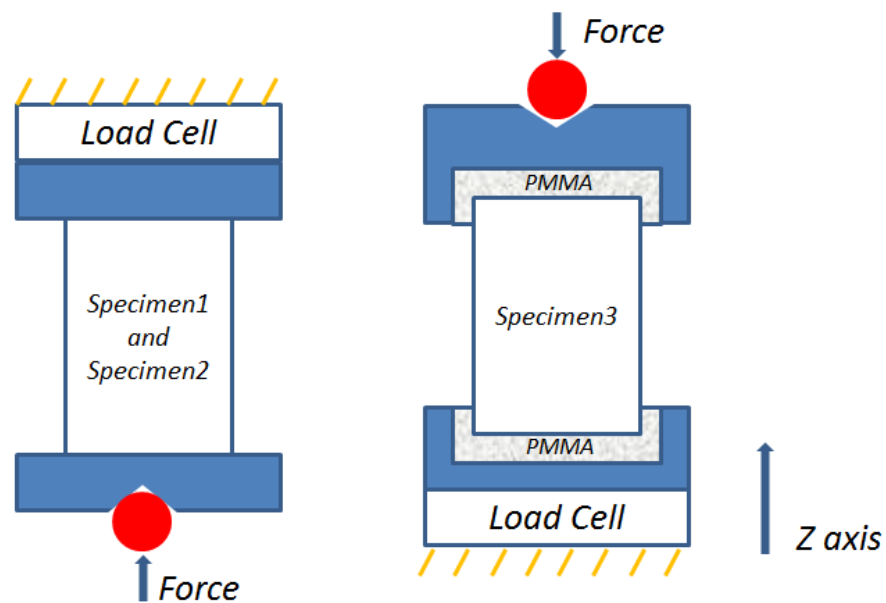
Fig.3.1. *Nominal configuration of the loading jigs used for testing Specimen1 and Specimen2 (left) and Specimen3 (right).*

3.2. In situ mechanical testing

All three specimens were tested in situ within the microCT system.

Specimen1 and Specimen2 were tested with the in situ compressive device provided by the manufacturer of the microCT (Skyscan 1172, Kontich, Belgium) with a 440 N loadcell. The specimens were positioned in between two parallel loading plates, in the middle of the device. A first scan (undeformed) was performed with the specimens under a small preload of 7 N in order to avoid motion artefacts. Afterwards, a compressive step up to 1% apparent strain was applied without repositioning and the specimen was scanned in its deformed configuration (Fig.3.1, left). These specimens were hydrated before testing.

Specimen3 was tested in a custom made in situ compressive device to be positioned within the same microCT model (Skyscan1172). The load was applied by a manual screw-ball joint mechanism and was measured with a 2 kN loadcell (LPM530, Cooper Instruments & Systems, Warrenton, USA). The 1.5mm external portions of the specimen were embedded in PMMA (Technovit 4071, Heraeus Kulzer Gmbh, Wehrheim, Germany) after proper alignment with the loading axis of the jig. A first

scan (undeformed) was performed with the specimen under a preload of 2 N in order to avoid motion artefacts. Afterwards, a compressive step to 120 N was applied without repositioning and the specimen was scanned in its deformed configuration. A liquid cell was used in order to keep the specimen submerged to 0.9% NaCl solution during the test (Fig.3.1, right).

It should be noticed that Fig. 3.1 shows only the nominal configuration of the two loading jigs. Ideally, the two flat surfaces of each specimen should be parallel and the compressive loading should be perfectly uniaxial (Fig.3.2, left). However, due to inevitable errors in the sample preparation and to the fact that the jig cannot be very stiff as some of the components, at least around the sample, should be made of radio transparent material, in reality both conditions are hardly achieved. The combination of these two issues makes the experiment slightly divergent from the nominal uniaxial compression test, resulting in a situation where one side of the sample is displaced more than the other (Fig.3.2, right). To reduce this effect, the external portions of the specimen can be embedded in a resin (e.g. polymethylmethacrylate, PMMA), in order to compensate for surface parallelism error (Fig.3.3, left). Nevertheless, it should be noted that the potential misalignment induced by the jig may still exist (Fig3.3, right). Of course on the top of this the densitometric and morphological heterogeneities of the specimen play a role in the inhomogeneity of the applied displacement field.

Because of all these factors, the resulting displacement fields are not so "uniaxial" as one would expect in a compression test. In particular, for the specimens tested without embedding, the misalignment produced a considerable gradient of displacement in the directions orthogonal to the compression axis. However, since the DVC provide full field information, and the goal of the finite element models subject of this thesis is to predict tri-axial deformation state, all these issues do not reduce the usefulness of these experimental data in the validation of our microFE models.
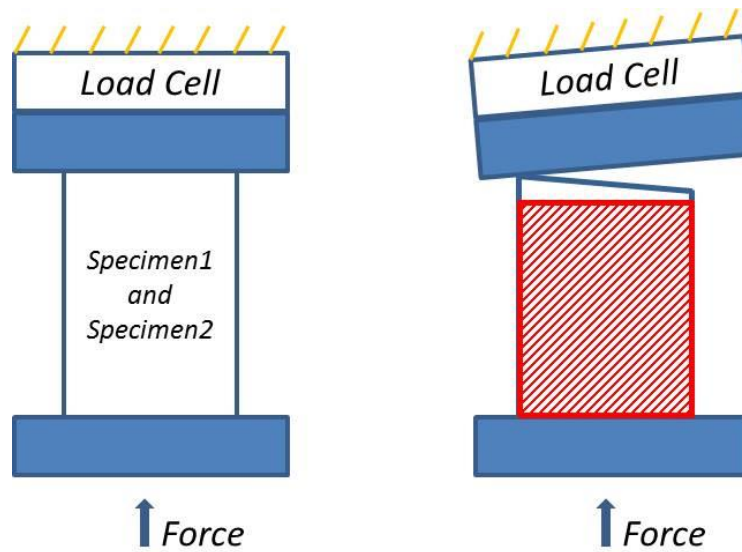
Fig.3.2. *Ideal status (left) and real conditions in exaggeration (right) of the loading jig used for testing Specimen1 and Specimen2. Slash lines shows the modelling part of the specimen.*
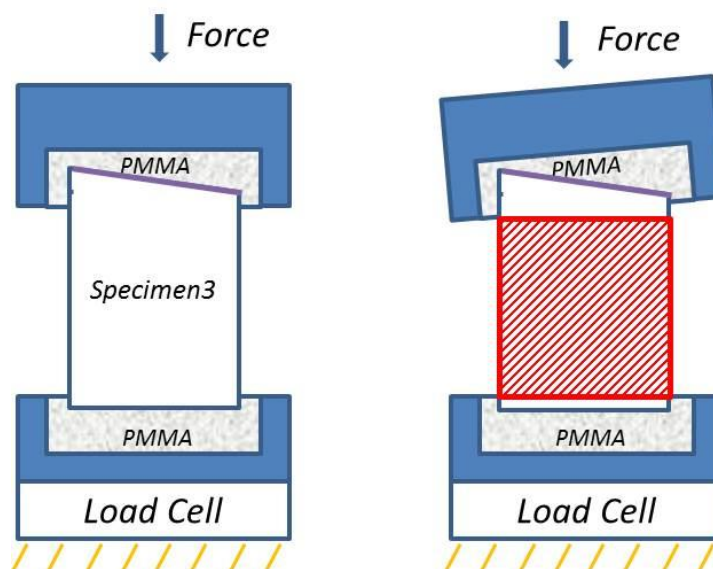
Fig.3.3. *Ideal status (left) and reality status in exaggeration (right) of the loading jig used for testing Specimen3. Slash lines shows the modelling part of the specimen.*

51

3.3. DVC measurement of displacement

The DVC method computes the field of displacements by registering elastically the couple of undeformed and deformed images for each specimen (34.44 μm and 19.84 μm) and therefore has the potential to validate microCT-based finite element models (microFE). In the present study, we used a deformable image registration toolkit (Sheffield Image Registration Toolkit, ShIRT) (Barber and Hose, 2005; Barber et al., 2007; Khodabakhshi et al., 2013). The registration equations are solved in the nodes of a grid superimposed to both images to be registered and with certain nodal spacing (NS), assuming a linear behaviour in displacement in between the nodes. In the current study, we used NS equal to 12 voxels (~ 413 μm) for human cancellous bone (Specimen1 and Specimen2) and NS 25 voxels (~ 496 μm) for bovine cancellous bone (Specimen3). With this NS the accuracy and precision in displacement is approximately 0.00016±0.0034 μm (~ 400 μm) for Specimen1 and Specimen2 and 0.0000098±0.00014 μm (~ 500 μm) for Specimen3 (Palanca et al., 2015). However, this value was calculated by using virtually moved images, which provides us the lower limit of the error.

The displacement contour plot in the nominal loading direction measured with DVC (Fig.3.4) showed asymmetric inhomogeneous displacement field. This effect is due to a combination of the issues reported in in 3.1: the parallelism error between the flat surfaces of the specimen and the slight misalignment of the loading plate would lead to a non-uniaxial compression, causing one side of the specimen translate more than the other. For Specimen 3, although the former issue has been fixed, the latter one still exist resulting in less severe problem than Specimen 1 and 2.
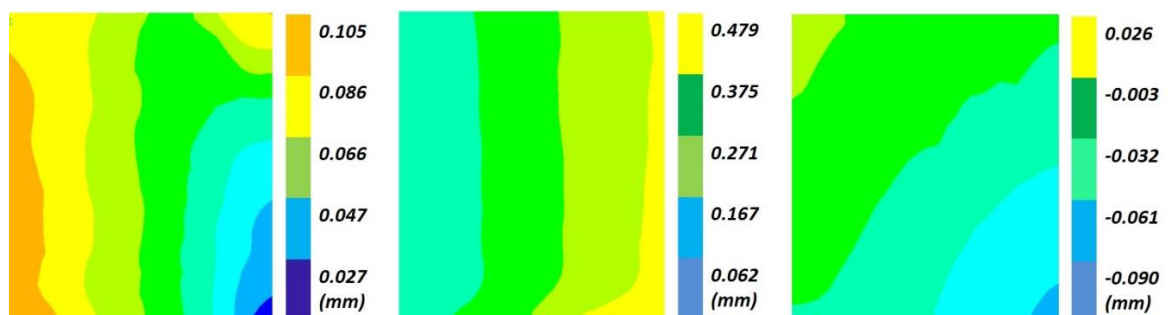
Fig.3.4. *Contour plot of the displacement along the loading direction viewed in the coronal plane for Specimen1 (left), Specimen2 (middle) and Specimen3 (right), measured from DVC*

3.4. MicroFE models' boundary conditions

In the following chapters the microFE models were analysed under three distinct boundary conditions (BC). Here we explain how these related to the experimental measurements they are supposed to represent. During the experiment they are continuously recorded by a load cell the resultant axial force, and by a displacement transducer the jig displacement, i.e. the change in distance between the mobile and the fixed plates. Then the DVC analysis provide a full field displacement, including the points in contact with the loading jig.

The first set of BCs was defined based on the resultant axial force as measured during the experiments. A zero vertical displacement was imposed to the fixed layer of nodes of the microFE model, while a vertical force was evenly distributed on the loaded layer of nodes, so that their resultant was equal to the measured resultant axial force (42N for Specimen1, 162N for Specimen2, and 120N for Specimen3). The nodes of the both layers were free to move in transverse direction for the Specimen1 and Specimen2 (free boundary conditions, assuming null friction at the plates) and fixed in the transverse directions for Specimen3 (simulation of embedding). This set of BCs is hereinafter in the following chapters referred to as "force BCs".

The second set of BCs was defined based on the jig displacement measured experimentally. Again, a zero vertical displacement was imposed to the fixed layer of nodes of the microFE model, while the jig displacement recorded experimentally was imposed as vertical displacement to all nodes of the loaded layer (130 μm for Specimen1, 115 μm for Specimen2; for Specimen3 no displacement was measured and this type of BCs was not modelled), leaving them free to move in the transverse directions. This set of BCs is hereinafter in the following chapters referred to as "displacement BCs".

The third set of BCs was defined after the DVC measurements (Fig.3.5). The DVC was used to determine the displacement vector at the coordinates of each node in the surface layer of the microFE model using element shape function that was applied as imposed displacements to the nodes. This set of BCs is hereinafter in the following chapters referred to as "interpolated BCs".

A local convergence study will be conducted to all microFEs with respected to three sets of BCs (Chapter 4) and the verified models will be used to predict the local displacements validated against the DVC measurements (Chapter 5).
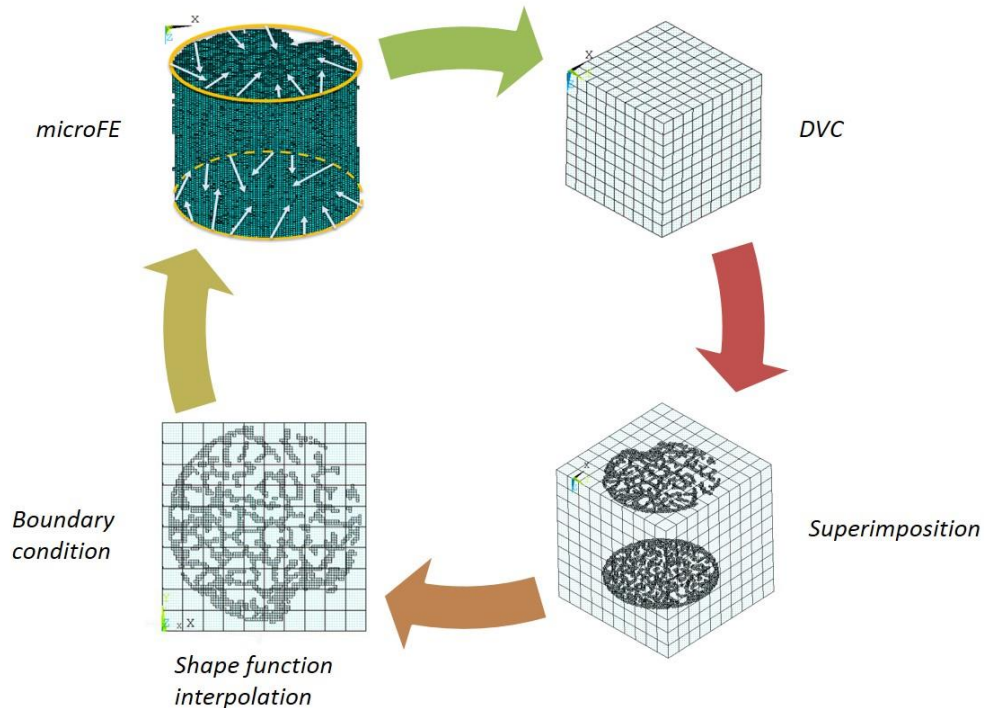
Fig.3.5. *"interpolated BC" assignment scheme*

3.5. References

Barber, D.C., Hose, D.R., 2005. Automatic segmentation of medical images using image registration: diagnostic and simulation applications. J. Med. Eng. Technol. 29, 53-63.

Dall'Ara, E., Barber, D., Viceconti, M., 2014. About the inevitable compromise between spatial resolution and accuracy of strain measurement for bone tissue: a 3D zero-strain study. J. Biomech. 47, 2956-2963.

Doube, M., Klosowski, M.M., Arganda-Carreras, I., Cordelieres, F.P., Dougherty, R.P., Jackson, J.S., Schmid, B., Hutchinson, J.R., Shefelbine, S.J., 2010. BoneJ: Free and extensible bone image analysis in ImageJ. Bone 47, 1076-1079.

Palanca, M., Tozzi, G., Cristofolini, L., Viceconti, M., Dall'Ara, E., 2015. Three-dimensional local measurements of bone strain and displacement: comparison of three digital volume correlation approaches. J. Biomech. Eng. 137.

Chapter4

Convergence study of cancellous bone tissue microFE

Summary

The complex geometry of cancellous bone tissue makes it difficult to generate micro computed tomography (microCT) based finite element models (microFE). Only a few studies investigated the convergence behaviour at the tissue scale. In this study, convergence behaviour of different microFE models (*homogeneous hexahedral model, heterogeneous hexahedral model and homogeneous tetrahedral model*) was investigated. The displacement, third principal strain and stress from coarser models were compared against its reference model. Uniaxial compression simulations using both linear-elastic and nonlinear constitutive equations were performed. The results of the current study confirm that linear elastic simulation of cancellous bones of homogeneous hexahedral models, assuring convergence of the displacements, stress and strain by using an element size less than one quarter of the trabecular thickness (34-40 µm). This modelling framework can be used for future reference. However, heterogeneous model, presented with different local modulus distribution in each mesh refinement, converged at an even finer scale (20 µm). By preserving the same geometry at each mesh refinement, tetrahedral model tends to converge better than other meshes, despite of the difficulty to in generating the mesh. Nonlinear simulations on the other hand, do not always guarantee the convergence at the same voxel size converged in linear simulation. Therefore, a local convergence study should always be conducted before any further analysis of the model. Further investigation is needed by using more samples and different CT modalities. Part of this chapter was originally published in Large-scale Finite Element Analysis of Bone Tissue MicroCT Data: A Convergence Study. Chen Y, Pani M, Taddei F, MAzzà F, Li X, and Viceconti M. J. J Biomech Eng. 2014 Oct;136(10):101013. DOI: 10.1115/1.4028106.

4.1. Introduction

With the rapid development of 3D image reconstruction techniques and commodity computer, the micro finite element (microFE) method has become a popular tool for modelling bones at the tissue scale, where the biomechanical behaviour is closely associated with biological function (Huiskes and Hollister, 1993; Vaughan et al., 2012; Viceconti, 2012). Traditional modelling processes, often referred to as smooth boundary or boundary-recovery FE methods, involve the estimation of structural topology using surface-fitting methods. Historically, boundary-recovery methods were difficult to apply at the tissue scale, because the small features present in cancellous bone (Fig.4.1) would had required a very large number of elements to be meshes accurately, much large of what for a long while was possible to solve with most available computers (Guldberg et al., 1998). On the contrary, microFE models could be solved with special-purpose solvers that leveraging on the regularity of the mesh size and topology allowed to solve models with hundred million elements in reasonable times. These models use 3D voxels of bone tissues obtained from microCT (Feldkamp et al., 1989) and convert them directly to equally sized hexahedral finite elements (Hollister et al., 1994; Keyak et al., 1990; van Rietbergen et al., 1995). One advantage of this method is that the generation of a well-conditioned mesh is guaranteed even with complex topology. However, as this type of mesh often has a "staircase-like" appearance, the boundary can only be smoothed when the element size approaches zero. More often than not, native voxel size in image dataset has to be kept in such models to achieve a reliable representation of the surface geometry, which results in a large number of degrees of freedom (NDOF) (Huiskes and Hollister, 1993; van Rietbergen, 2001; Viceconti, 2012). Consequently, simulations performed using these FE models are computationally intensive, and sometimes with low prediction accuracy on the bone surface or internally (Depalle et al., 2012). Nevertheless, this type of model, with a resolution fine enough to capture the bone microstructure (Bouxsein et al., 2010), can be used to predicted stiffness and strength of the bone tissue (Niebur et al., 2000; Pistoia et al., 2004), which make it a potential tool for osteoporotic fracture diagnosis.

Over the years, only a few researchers have investigated the relationship between the mechanical properties of trabecular bones and the optimal element size. In a study exploring the relationship between image resolution and meshing techniques for trabecular bones, Ulrich et al. (1998) found that Cartesian meshes with a resolution of

168 µm taken from the femoral head produced better results, compared against models of 28 µm as reference (a minor decrease of 3% in the elastic modulus and 9% in tissue stress were found).

Fig.4.1. *3D representation of bovine cancellous bone specimen scanned by microCT at 9.92 µm*

A recent study conducted by Torcasio et al. (2012) aimed at validating specimen-specific micro FE models for the assessment of bone strains in the rat tibia under compression showed that Cartesian models of 40 µm and 80 µm converged with a difference in stiffness of 1.30% and 1.35% respectively compared with the reference model of 20 µm. Depalle et al. (2012) showed that at the tissue level, the increase in element size affects the local stress distribution during a compression test simulation. Both stiffening and global softening due to discretisation errors caused fluctuation in local stress values. The author also found that numerical stiffening errors occurred when trabecular thickness was close to element size, especially when there were less than three elements across the cross-section. This was in agreement with Niebur et al. (1999) where they found that the difference in apparent modulus were always less than 10% when the ratio of mean trabecular thickness over element size is greater than four. Bert van Rietbergen (2001) suggested that the accuracy of simulation in such models was dependent on a number of factors, such as the types of bones (Pistoia et al., 2001; Ulrich et al., 1998), image acquisition modalities (van Rietbergen et al., 1998), and the complexity of various loading conditions. It is therefore not surprising to find that some researchers have reported considerable errors in their FE apparent modulus comparing between models with voxel sizes of 50 µm and 20 µm (Ladd and Kinney, 1998), whereas others have reported sufficiently converged results for models with a voxel size of up to 150 µm (Ulrich et al., 1998; van Rietbergen, 2001; van Rietbergen et al., 1998).

A systematic numerical validation is required in order for this microFE approach to be used as a standard in the future. Also, for the simulation of bone failure behaviour, where large deformation and strain-dependent changes become significant, a non-linear FE test is required (Christen et al., 2010; van Rietbergen, 2001). It was shown that a bilinear constitutive model with asymmetric tissue yield criteria could reach more accurate solution than a linear model (Niebur et al., 2000). The structural failure of human radii predicted by non-linear microFE models correlated well with experimental tests based on high-resolution peripheral quantitative computer tomography (HR-pQCT) (MacNeil and Boyd, 2008). Viceconti (2012) also suggested that an elastic-perfectly-plastic constitutive equation could be used to yield a better prediction of bone tissue behaviour, where stress raisers within complex bone tissue might bring considerable errors. In addition, from a mathematical point of view, higher order values such as strains are usually preferred over the displacement as a convergence criterion, as strain is slower to converge in an area with a large strain gradient (Bathe, 1996; Fagan, 1992).

Previous convergence studies were mostly conducted on the apparent properties (Ulrich et al., 1998; van Rietbergen et al., 1998; van Rietbergen et al., 1995; Yeni et al., 2005), whereas only a limited number of studies investigated the local results convergence (Niebur et al., 1999; Torcasio et al., 2012). Moreover, there is conclusive evidence showing that bone is constantly remodelled (Currey, 1999), thus each volume of tissue might have a different level of mineralisation and consequently exhibit significantly difference mechanical properties. Some studies suggested that incorporating the bone heterogeneity into microFE models is likely to affect the prediction of cancellous bone mechanical properties (Kaynia et al., 2015; Renders et al., 2008; van der Linden et al., 2001; van Ruijven et al., 2007). In addition, in every validation study, the boundary conditions (BC) applied to the model should be as close as the experiments, therefore it is essential to explore the model convergence behaviour under different BCs. Therefore, the aims of the present study are: (1) to conduct a convergence test of cancellous bones with linear elastic homogeneous hexahedral models under different BCs. Post yield convergence behaviour will also be investigated; (2) to investigate the convergence behaviour of heterogeneous hexahedral model and homogeneous tetrahedral model using the most accurate BC (results from an independent study); (3) to obtain the optimal image voxel size for such FE models to achieve a reasonable convergence on a powerful high performance computing (HPC) cluster.

4.2. Materials and methods

This convergence study was conducted with the same methodology described in an earlier paper (Chen et al., 2014). However, we decide to report here the description on a second study we conducted more recently on other specimens, because those specimens are also used in the following chapters. All microFE models used in this chapter were generated from the undeformed image datasets and solved while subject to the three boundary conditions based on the validation experiments, as explained in chapter 3.

4.2.1. MicroFE models

Homogeneous hexahedral model

To create the homogeneous hexahedral models, the original image datasets were first subsampled. From the original microCT images with a voxel size of 17 μm (Specimen 1 and 2 for example), 2 x 2 x 2 voxels were condensed into one, resulting in a new image data with a resolution of 34 μm. Similarly, 4 x 4 x 4, 8 x 8 x 8 voxels were grouped to generate the datasets of 68 μm and 136 μm, respectively. Then the images were binarised using a single level threshold by finding the mean value between two peaks (one representing the bone tissue, one representing the background) in the grayscale histograms (Fig.4.2). Voxels below the threshold value were deleted and for those above the threshold value, a connectivity filter (Matlab, R2014b, Mathworks, Inc.) was applied to remove the isolated voxels. In particular, only elements with surface (four nodes) connectivity were kept in the model. Finally, each remaining voxel in the image datasets was converted directly into equally sized 8-node hexahedral elements. The material properties for this type of model were assumed to be linear and isotropic, with a uniform Young's modulus of 17 GPa (Bayraktar et al., 2004; Morgan et al., 2003) and a Poisson's ratio of 0.3 (Pistoia et al., 2002). This type of model is hereinafter referred to as "HOMO-HEXA".

Heterogeneous hexahedral model

For heterogeneous hexahedral model, every voxel in the subsampled image datasets was converted directly into equally sized 8-node hexahedral elements. Voxels having greyscale above the mean value between two peaks in the greyscale histogram were considered as bone voxels. The greyscale of each voxel is considered proportional to the local tissue mineral density (TMD). This is equivalent to the concentration of hydroxyapatite (HA) (Mulder et al., 2008; Nuzzo et al., 2002) and quantified by

calibrating the greyscale with reference measures of phantoms containing HA of 250 and 750 mg/cm^3. The tissue material properties E_t were approximated from the TMD of the corresponding voxel according as $E_t = E(TMD_t/TMD_{mean})$ (Currey, 1988; van Ruijven et al., 2007), where E is the typical modulus of the trabecular specimen of 17GPa, TMD_t the TMD of the voxel, TMD_{mean} the mean TMD of all voxels. The TMD of all voxels were transformed into corresponding tissue modulus using this empirical equation. As the maximum module of elasticity of bone tissue found using micro-indentation or nano-indentation at the tissue scale is about 25 GPa (Mirzaali et al., 2015; Wang et al., 2006), voxels having elastic modulus above this upper limit (accounts for 1.5% of all bone voxels) were treated as noises from the scan and assigned with a value equal to 25 GPa. The modulus were discretized to 629 material cards and assigned with a Poisson's ratio of 0.3 (Pistoia et al., 2002). Voxels having greyscale below the first peak value of the histogram were assumed to be marrow and a uniform elastic modulus of 0.035 MPa and a Poisson's ratio of 0.5 was assigned (Jansen et al., 2015). Voxels having greyscale falling in between the bone and marrow thresholds were treated as the transition zone (newly formed bone tissue which was partially mineralized or voxels on the bone surface, which greyscale is a mixture between the bone and the marrow). The modulus values were assigned using a bilinear relationship, where the lowest and highest greyscale value were matched with marrow tissue modulus of 0.035 MPa and the lowest E_t of the bone tissue respectively. The greyscale of the midpoint was offset by 90% from the highest greyscale of marrow and the modulus of the midpoints was offset by 10% from the marrow modulus. In our study, only Specimen3 was scanned with calibration phantoms, heterogeneous model was only generated for this specimen (Fig.4.3). This type of model is hereinafter referred to as "HETE-HEXA".

Homogeneous tetrahedral model

10-node tetrahedral models of the specimen3 were automatically generated from microCT images using ScanIP (SimplewareLtd, Exeter, UK). This mesh creation algorithm is based on an enhanced version of the volumetric marching cube method modified to work for both single and multiple parts (Young et al., 2008). Then the algorithm extracts the conforming surfaces topology and automatically meshes based on its complexity and features. This algorithm is most suited to geometries like cancellous bone where there is a need for preserving small features while decimating the mesh elsewhere. The user can control the mesh refinement by indicating a tentative mesh

refinement factor. Different mesh refinements were generated with similar DOFs of the homogeneous hexahedral models. The material properties for this type of model were assumed to be linear and isotropic, with a uniform Young's modulus of 17 GPa (Bayraktar et al., 2004; Morgan et al., 2003) and a Poisson's ratio of 0.3 (Pistoia et al., 2002), as for the homogeneous hexahedral models. This type of model is hereinafter referred to as "HOMO-TETRA". Three different mesh types are shown in Fig.4.4.
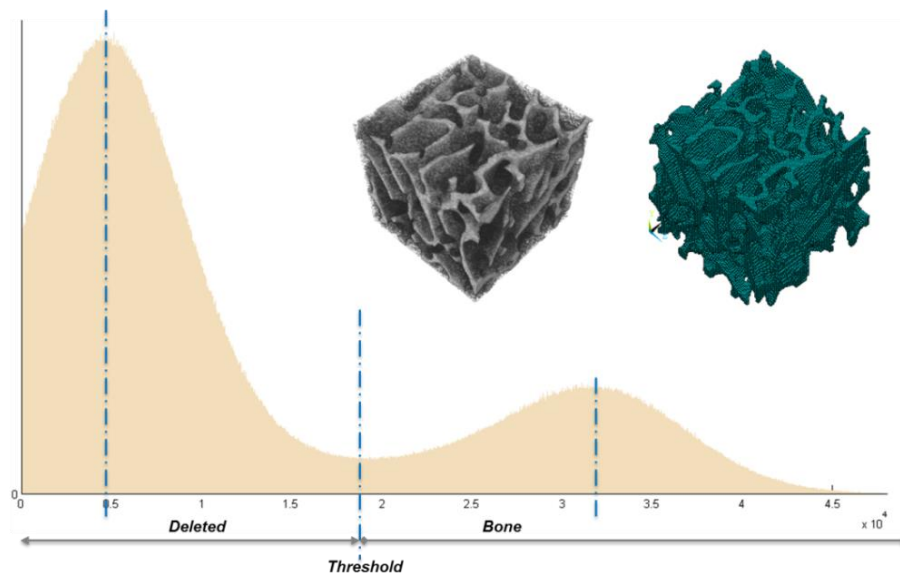
Fig.4.2. *HOMO-HEXA mesh generation scheme (The figure shows the histogram of the greyscale of voxels distributed throughout the sample, with X the greyscale value and Y the frequency; the sub-image cropped from the centre of the image dataset shows an example of the mesh)*
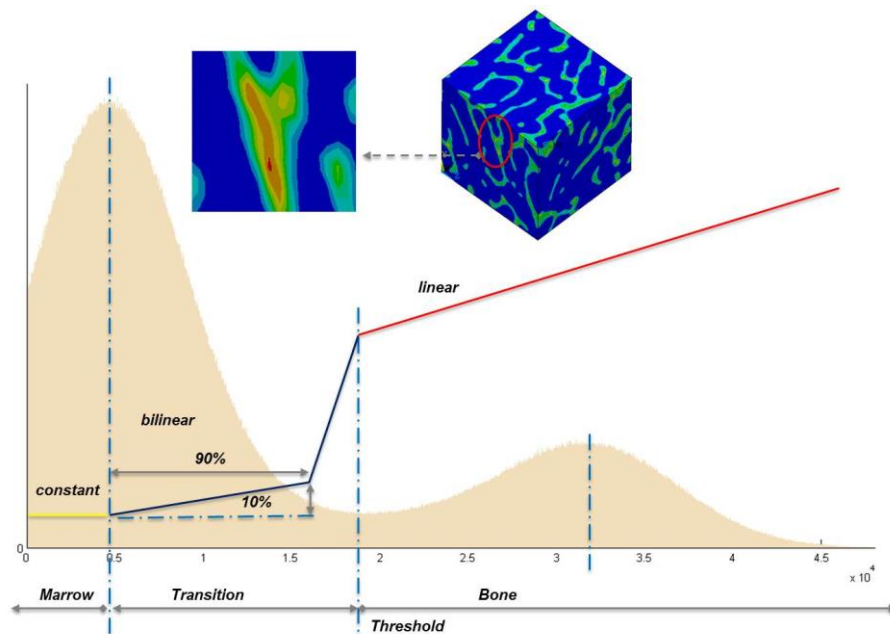
Fig.4.3. *HETE-HEXA mesh generation scheme (The figure shows the histogram of the greyscale of voxels distributed throughout the sample, with X the greyscale value and Y the frequency; the sub-image cropped from the centre of the image dataset shows an example of the mesh and the colour plot reflects the module of elasticity of the sample)*
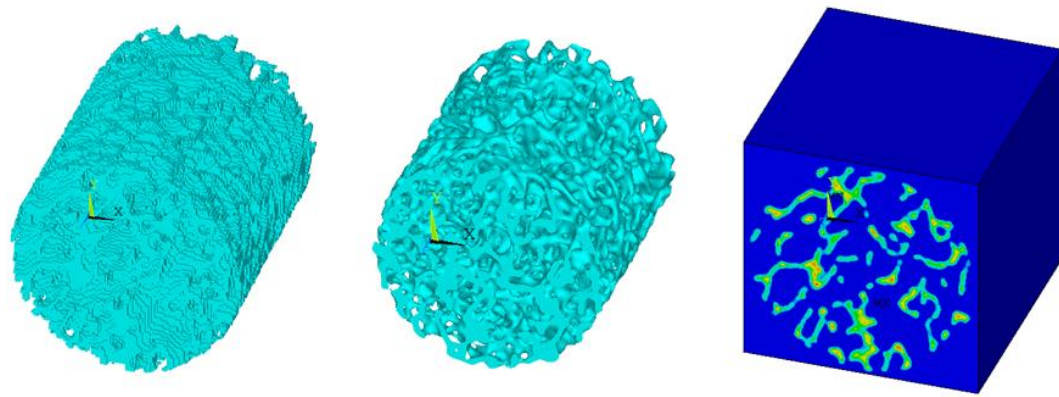
Fig.4.4. *HOMO-HEXA model (left), HOMO-TETRA model (middle) and HETE-HEXA model (right) of bovine cancellous bone tissue (Specimen3)*

4.2.2. Boundary conditions

Three different boundary conditions (BCs) were used for linear elastic simulations in order to replicate the BCs measured in experiments: "force BCs", "displacement BCs" and "interpolated BCs". Please refer to Chapter3 for details.

To explore the nonlinear behaviour of microFE model in terms of local convergence, a nonlinear simulation was also performed: a displacement was applied to models to simulate a uniaxial compression. As the objective was not to investigate the bone behaviour under larger deformation, but to achieve more accurate predictions for those small areas of bone tissues experiencing plastic deformation, a bilinear model approximating an elastic-perfectly-plastic constitutive equation was adopted, where the bone is considered to behave perfectly elastic up to the yield strain (7000 $\mu\varepsilon$) and then to deform in a perfect plastic manner without the need to increase the stress (MacNeil and Boyd, 2008; Niebur et al., 2000; Viceconti, 2012). A displacement load was predetermined in order to reach a maximum 3rd principal strain of 20,000 $\mu\varepsilon$ for the coarsest mesh refinement for each mesh. All other simulations were conducted using the same displacement.

All above-mentioned BCs were applied to the HOMO-HEXA of each specimen. The BC leading to the most accurate predictions ("interpolated BCs", results from an independent study, please refer to Chapter5 for details) was applied also to the HOMO-TETRA and HETE-HEXA for Specimen3. The most refined HETE-HEXA for Specimen3 (10 μm) consists of around 600 million of elements. In order to reduce the computational cost, we focused our attention on a sub-volume of 5 x 5 x 5 mm at higher

strain. In order to maintain the same BC, the boundary nodes of the sub-model were superimposed into the last solved mesh refinement and the displacement for these nodes were derived using element shape function. All models and BCs information is summarized in Table.4.1.

Table.4.1. Specimens and their corresponding models and BCs

Specimen	BCs	Models		
		Homo Hexa	*Hete Hexa*	*Homo Tetra*
Specimen1	Force	Yes		
	Disp	Yes		
	Interp	Yes		
	Nonlinear	Yes		
Specimen2	Force	Yes		
	Disp	Yes		
	Interp	Yes		
	Nonlinear	Yes		
Specimen3	Force	Yes		
	Disp			
	Interp	Yes	Yes	Yes
	Nonlinear	Yes		

4.2.3. Results comparison

The quantity chosen for the convergence study depends on the purpose: for example it can be the Von Mises Stress, used to quantify the failure in ductile materials such as metal (Perez-Gonzalez et al., 2011) or the maximum principal strain, frequently used to calculate the failure of bone tissue (Schileo et al., 2008). Here, to explore the convergence behaviour of cancellous bones at the tissue scale, three nodal outputs were examined. These are the 3rd principal strain, the 3rd principal stress (the most negative values for compression), and the displacement module (intensity of the displacement vector).

Since the Saint-Venant's Principle (Berdichevsky and Foster, 2003) is not valid near the boundary conditions, the region of interest for the convergence analysis was limited to the middle part (about 1/3) of the whole model. Bruce Irons first proposed the Patch Test in 1965 from a physical perspective (Irons and Loikkanen, 1983). But only in 2001 the patch test was proved sufficient for the convergence of nonconforming finite elements provided some approximation and weak continuity are satisfied (Wang, 2001). A reliable patch test requires all the nodes that exist in the coarsest mesh also exist in all

refined meshes, and the peak values at nodes with fixed spatial position are investigated. The code used to generate HEXA models guarantees overlapped nodes for each mesh refinement, making investigating node at the same spatial location possible. Because of the way the HOMO-TETRA models are generated, there is no guarantee that a mesh node investigated in one mesh will locate at the same spatial position in other meshes. Therefore, the convergence behaviour for HOMO-TETRA was investigated at the same spatial location by deriving the results using element shape function interpolation.

In order to compare the results between models with different mesh refinements, HEXA models preserving the original voxel size (17 μm for Specimen 1 and 2, 10 μm for Specimen3) were assumed to provide the most accurate results and therefore used as reference. For the HOMO-TETRA models we chose as reference a mesh refinement which has a number of degrees of freedom comparable to that of the HOMO-HEXA mesh at the original voxel size.

Convergence studies are time-consuming, and thus they are conducted only for a limited number of locations. Some authors prefer to focus their attention on the region where the largest spatial gradient of the selected output is predicted (maximum gradient criterion); this because if the mesh refinement is found adequate in those regions, it will surely be adequate also anywhere else. Some other authors prefer to test the convergence of the mesh refinement in the region where the highest value is predicted (maximum value criterion), because these are usually also among the regions with the highest gradient, and the accuracy of the predictions in these regions are the most important. Whereas locating the node with the peak value is standard post-processing feature in most FE codes, spatial gradients are not normally available. However, the regions where the gradients of stress or strain are higher are also the regions where the stress error is higher (Zienkiewicz and Zhu, 1987). In this study in all models convergence was investigated in the region with the largest 3rd principal strain and the one with the lowest convergence rate was selected and investigated on the behaviour with node of largest stress error. For the HEXA models (which satisfy the patch test requirements) we tested the convergence in the node with the highest 3rd principal strain (or the highest stress error) among those present in all mesh refinements; for the TETRA mesh, we simply took the node with the peak value in the most refined mesh, and interpolate the values at the same coordinates in the other meshes.

For each model, the percentage differences with respect to the reference model in each mesh refinement were computed and the mesh was assumed to be at convergence if such difference decreased monotonically with the element size, and the percentage difference was less than 5% for linear simulation and 10% for non-linear simulation (Chen et al., 2014).

All simulations were performed using ANSYS (Release 15.0, ANSYS, Inc.) on a high performance parallel computing cluster (SGI UV-2000 Intel Xeon E5-4650, 2.70 GHz, 104 cores, 1.6TB of RAM).

4.3. Results

For the linear elastic simulations of HOMO-HEXAs models under different BCs (Table.4.2), stress and strain started to show convergence with element size of 34-40 μm, depending on the model. To be specific: at 34 μm for Specimen1 and Specimen2 (lowest percentage of less than 1% for 3rd principal strain and 1.7% for 3rd principal stress with Specimen2 controlled by 'force BC') and at 40 μm for Specimen3 (lowest percentage of 1.7% for 3rd principal strain controlled by 'interpolated BC' and less than 1% for 3rd principal stress controlled by 'force BC'). For Specimen3, both strain and stress kept converging at 20 μm (lowest percentage of 1.2% for 3rd principal strain controlled by 'force BC' and less than 2.1% for 3rd principal stress controlled by 'interpolated BC'). For the case of 'force BC' in particular, the percentage difference decreased smoothly with the decreasing size of element for both strain and stress, whereas for 'displacement BC' and 'interpolated BC' the percentage difference fluctuated between the second coarsest mesh refinement and the second finest mesh refinement (68 and 34 μm models for specimen1 and specimen2, 40 and 20 μm models for specimen3). It was also found that the percentage difference between the coarsest mesh refinement and second coarsest mesh refinement in general was higher in Specimen1 and Specimen2 (136 and 68 μm models) than in Specimen3 (80 and 40 μm models). The highest difference happened in Specimen2 controlled with 'force BC' where the value for strain was 52.8% for 136 μm and 4.9% for 68 μm models and the value for stress was 62.3% for 136 μm and 5.3% for 68 μm models respectively. It is noticed from Table 4.2 that the model of Speciemen1 using "displacement BC" has the lowest convergence rate for each mesh refinement. This simulation was selected to further investigate the convergence behaviour using maximum gradient criterion. By

investigating the node subjected the highest stress error, the convergence behaviour is similar to the one using maximum value criterion. The results for linear simulation of HOMO-HEXAs were summarised in Table.4.2 and Table 4.3.

Regarding results using different mesh types under the same BC (interpolated BC') for Specimen3 (Table.4.4): for HETE-HEXA, both 3rd principal strain and 3rd principal stress converged at 20 µm (2.5% for 3rd principal strain and 3.1% for 3rd principal stress); for HOMO-TETRA, all mesh refinements with similar NDOFs of the HOMO-HEXA have reached convergence (lowest percentage of 2.6% for 3rd principal strain and 3.9% for 3rd principal stress). However, the mesh generation time for HOMO-TETRA is in general longer than HOMO-HEXA having comparable NDOFs (to generate models of around 40 million NDOFs, it took approximately half an hour for the HOMO-HEXA and 2 hours for HOMO-TETRA). The results for linear simulation of Specimen3 using different mesh types were summarised in Table.4.4.

The displacements for linear simulations have all converged at the coarsest mesh refinement for each specimen (136 µm for specimen1 and specimen2, 80 µm for specimen3), except for models of 136 µm for Specimen1 controlled by 'force BC', where the percentage difference was close to the considered threshold (5.2%). The convergence rate for the displacement was faster than strain and stress, where they all reached a converged solution of less than 1% with the second coarsest mesh refinements (68 µm for specimen1 and specimen2, 40 µm for specimen3).

Both the elapsed time and the memory usage increased dramatically with a decrease in element size. The largest model (sub-volume of the most refined HETE-HEXA) required 605 GB of real memory and approximately 3 hours to run. The results for linear simulation were summarised in Table.4.2-4.4.

The convergence behaviour for the non-linear simulations was similar to the linear case, except that the percentage differences were larger at each mesh refinement (Table.4.5). Stresses have started to converge at the second coarsest mesh refinement (68 µm for specimen1 and specimen2, 40 µm for specimen3 (lowest percentage of less than 1% for specimen1) and kept converging for the next mesh refinement. However, model of 34 µm of specimen2 failed to reach the convergence (13.2%) in terms of strain according to our criteria. Displacement again converged faster than strain and stress, where it started to converge with the least refined meshes. Similar to the linear case, both the

elapsed time and the memory increased dramatically with a decrease in element size. In addition, the elapsed time required for each mesh refinement in non-linear simulations was considerably longer than that of linear simulations. The largest model (10 µm model of specimen3) required approximately 589 GB of real memory and 38 hours to run. The results for non-linear simulation were summarised in Table.4.5.

Table.4.2. *Linear simulations for HOMO-HEXA models at peak strain location*

BCs	Specimen	Model (μm)	NODFs (million)	Elapsed Time (s)	Memory Usage (GB)	3rd Principal Strain (με) [% difference to reference model]		3rd Principal Stress (MPa) [% difference to reference model]		Displacement (μm) [% difference to reference model]	
Force	Specimen1	136	0.8	14	1.2	-1315	(32.7%)	-22.4	(34.3%)	12.2	(5.2%)
		68	4.9	47	9.0	-1048	(5.1%)	-16.0	(4.1%)	11.6	(<1%)
		34	33.1	911	52.2	-1024	(2.7%)	-17.0	(2.2%)	11.6	(<1%)
		17 *	237.9	5,310	371.2	-988	(0%)	-16.7	(0%)	11.6	(0%)
	Specimen2	136	0.8	13	1.2	-6667	(52.8%)	-120.4	(62.3%)	17.4	(2.8%)
		68	4.7	50	8.6	-4576	(4.9%)	-78.2	(5.3%)	17.8	(<1%)
		34	32.0	878	49.9	-4337	(<1%)	-75.4	(1.7%)	17.8	(<1%)
		17*	229.6	5,103	348.5	-4361	(0%)	-74.3	(0%)	17.9	(0%)
	Specimen3	80	1.1	17	2.8	-5430	(9.1%)	-94.7	(15.8%)	23.7	(<1%)
		40	6.8	78	12.3	-5140	(3.3%)	-82.4	(<1%)	23.6	(<1%)
		20	43.6	1,098	84.7	-5036	(1.2%)	-80.0	(2.2%)	23.5	(<1%)
		10*	302.5	7,122	510.9	-4977	(0%)	-81.7	(0%)	23.7	(0%)
Disp	Specimen1	136	0.8	14	1.2	-7009	(69.8%)	-117.1	(71.5%)	111.6	(1.5%)
		68	4.9	49	8.8	-4758	(15.3%)	-85.9	(25.9%)	111.3	(<1%)
		34	33.1	901	53.7	-4325	(4.8%)	-70.3	(3.0%)	111.4	(<1%)
		17*	237.9	5,201	383.6	-4127	(0%)	-68.2	(0%)	111.5	(0%)
	Specimen2	136	0.8	12	1.2	-6978	(16.6%)	-118.3	(19.7%)	91.6	(2.1%)
		68	4.7	55	8.2	-6027	(<1%)	-100.3	(1.4%)	89.7	(<1%)
		34	32.0	864	50.7	-6243	(4.3%)	-94.9	(3.9%)	89.7	(<1%)
		17*	229.6	5,188	331.1	-5986	(0%)	-98.8	(0%)	89.7	(0%)
Interp	Specimen1	136	0.8	12	1.1	-7004	(46.7%)	-126.9	(55.5%)	71.7	(<1%)
		68	4.9	53	8.8	-5141	(7.7%)	-72.4	(11.2%)	71.9	(<1%)
		34	33.1	889	50.1	-5003	(4.8%)	-84.4	(3.5%)	71.6	(<1%)
		17*	237.9	5,431	371.9	-4774	(0%)	-81.6	(0%)	71.7	(0%)
	Specimen2	136	0.8	10	1.2	- 6836	(38.1%)	-118.9	(40.7%)	229.1	(1.3%)
		68	4.7	57	8.1	- 4977	(<1%)	-84.6	(<1%)	226.3	(<1%)
		34	32.0	888	49.8	- 5171	(4.5%)	-86.7	(2.6%)	226.7	(<1%)
		17*	229.6	5,057	338.9	- 4949	(0%)	-84.5	(0%)	226.2	(0%)
	Specimen3	80	1.1	21	2.5	-6933	(25.1%)	-117.6	(24.6%)	43.1	(<1%)
		40	6.8	83	11.6	-5636	(1.7%)	-96.1	(1.8%)	43.2	(<1%)
		20	43.6	1,113	83.2	-5664	(2.2%)	-96.3	(2.1%)	43.2	(<1%)
		10*	302.5	7,420	506.3	-5542	(0%)	-94.4	(0%)	43.2	(0%)

*Reference model

Table.4.3. *Linear simulations for Specimen1 (HOMO-HEXA) at peak stress error location*

BCs	Specimen	Model (μm)	NODFs (million)	Elapsed Time (s)	Memory Usage (GB)	3rd Principal Strain (με) [% difference to reference model]		3rd Principal Stress (MPa) [% difference to reference model]		Displacement (μm) [% difference to reference model]	
Disp	Specimen1	136	0.8	14	1.2	-6833	(73.1%)	-115.2	(76.7%)	101.1	(1.6%)
		68	4.9	49	8.8	-4442	(12.5%)	-82.6	(26.7%)	99.5	(<1%)
		34	33.1	901	53.7	-4138	(4.8%)	-67.5	(3.5%)	99.4	(<1%)
		17*	237.9	5,201	383.6	-3948	(0%)	-65.2	(0%)	99.4	(0%)

*Reference model

Table.4.4. Linear simulation of Specimen3 for all mesh types at peak strain location

BCs	Mesh Type	Model (µm)	NODFs (million)	Elapsed Time (s)	Memory Usage (GB)	3rd Principal Strain (µε) [% difference to reference model]		3rd Principal Stress (MPa) [% difference to reference model]		Displacement (µm) [% difference to reference model]	
Interp	HOMO-HEXA	80	1.1	21	2.5	-6933	(25.1%)	-117.6	(24.6%)	43.1	(<1%)
		40	6.8	83	11.6	-5636	(1.7%)	-96.1	(1.8%)	43.2	(<1%)
		20	43.6	1,113	83.2	-5664	(2.2%)	-96.3	(2.1%)	43.2	(<1%)
		10*	302.5	7,420	506.3	-5542	(0%)	-94.4	(0%)	43.2	(0%)
	HETE-HEXA	80	3.8	34	7.7	-6792	(7.1%)	-157.5	(13.2%)	56.4	(<1%)
		40	29.6	967	46.5	-6682	(8.6%)	-127.9	(8.1%)	57.1	(<1%)
		20	279.1	6,800	441.7	-7128	(2.5%)	- 134.8	(3.1%)	56.8	(<1%)
		10*	384.1	11,302	605.2	-7311	(0%)	-139.1	(0%)	56.9	(0%)
	HOMO-TETRA	62	5.9	129	16.8	-6777	(2.9%)	-115.7	(4.4%)	23.0	(<1%)
		17	46.0	1350	74.9	-6758	(2.6%)	-115.2	(3.9%)	23.0	(<1%)
		11*	275.3	6,233	436.8	-6587	(0%)	-110.8	(0%)	23.0	(0%)

*Reference model.

• The most mesh refinement of HETE-HEXA model was generated using a sub-volume of the images, therefore the elapsed time and memory is not comparable with others.

• In HOMO-TETRA model, the minimum element edge length was reported instead of voxel size.

Table.4.5. Nonlinear simulation for HOMO-HEXA models at peak strain location

Specimen	Model (µm)	NODFs (million)	Elapsed Time (s)	Memory Usage (MB)	3rd Principal Strain (µε) [% difference to reference model]		3rd Principal Stress (MPa) [% difference to reference model]		Displacement (µm) [% difference to reference model]	
Specimen1	136	0.8	105	2.3	-19420	(140.8%)	-87.4	(8.4%)	34.1	(3.6%)
	68	4.9	556	12.4	-8459	(4.9%)	-80.9	(<1%)	33.2	(<1%)
	34	33.1	15,318	62.9	-8644	(7.2%)	-81.7	(1.3%)	32.9	(<1%)
	17*	237.9	96,015	430.7	-8064	(0%)	-80.7	(0%)	32.9	(0%)
Specimen2	136	0.8	120	2.1	-18971	(84.1%)	-128.7	(17.4%)	65.3	(5.2%)
	68	4.7	513	12.4	-9385	(8.9%)	-115.9	(5.8%)	64.1	(3.2%)
	34	32.0	14,455	59.9	-11665	(13.2%)	-114.3	(4.3%)	61.9	(<1%)
	17*	229.6	91,243	414.9	-10302	(0%)	-109.6	(0%)	62.1	(0%)
Specimen3	80	1.1	204	3.4	-19918	(65.0%)	-124.2	(10.5%)	38.6	(4.3%)
	40	6.8	889	15.0	-13957	(15.6%)	-113.9	(1.7%)	37.3	(<1%)
	20	43.6	21,713	98.8	-12522	(3.7%)	-108.4	(3.2%)	37.1	(<1%)
	10*	302.5	140,350	588.7	-12074	(0%)	-112.4	(0%)	37.1	(0%)

*Reference model

4.4. Discussion

The aim of the present study was to investigate the convergence behaviour of microFE models of cancellous bones at the tissue level in both elastic and post-elastic conditions, and to determine the optimal voxel size in terms of simulation accuracy as well as computational costs. In linear simulations of HOMO-HEXAs, all three parameters investigated (3rd principal strain, 3rd principal stress and displacement) reached a converged solution at the second or third most mesh refinement (34 µm models for

specimen1 and specimen2 and 40 μm models for specimen3). Considering the mean trabecular thickness reported in Chapter3 (192 μm for specimen1, 188 μm for specimen2 and 171 μm for specimen three), the ratio of mean trabecular thickness over element size is greater than four. Niebur et al. (1999) reported that the difference in apparent modulus were always less than 10% when the ratio of mean trabecular thickness over element size is greater than four. Therefore, the convergence behaviour of cancellous bone tissue is not only limited to the apparent properties but also can be extended to the local properties even using different BCs. However, the convergence behaviour of local parameters was seemingly in contradiction with that reported by Niebur et al. (1999), where the maximum tissue strain failed to converge. It should be noted however, Niebur's study was conducted by investigating the nodes having maximum tissue level strain at each mesh refinement, whereas the same spatial positions were used in this study, which provides a more consistent convergence evaluation by comparing differences at the same location.

Strain and stress in models using 'force BC' in general converged more smoothly, whereas the percentage difference in models using 'displacement BC' and 'interpolated BC' fluctuated. This is most likely due to the over constrained nature of the displacement-controlled BCs. In such case, by over-constraining, the loading condition of the same node in each mesh refinement may be changed: a node that is pushed in compression in one mesh might be less compressed (or pulled in tension) in other mesh refinements. Moreover, it should be noted that stress values are not guaranteed to converge. They sometimes fluctuate, especially when the changes in element size are large (Pointer, 2004). The higher difference seen between (136 and 68 μm models) in specimen1 and specimen2 is possibly because of the large element size used in the least refined mesh (136 μm), a value comparable to the mean trabecular thickness. By using a single global threshold value, differences in geometry and connectivity compared to the next mesh refinement may play a large role. Therefore, a higher difference in convergence rate between these two mesh refinements was expected.

The HETE-HEXA failed to converge until at 20 μm. This might be due to the different modulus of elements surrounding the node investigated in each mesh refinement, which produced higher stress error. The convergence behaviour for such model needs further investigation by using synchrotron radiation micro-computed tomography (SRμCT), which provide better image quality and therefore more accurate TMD prediction (Gross

et al., 2012; Kaynia et al., 2015; Kazakia et al., 2008). HOMO-TETRA models, by preserving the same smoothed geometry of each mesh refinement, showed faster convergence rate than HOMO-HEXA models in all cases.

The displacement converged much faster than the strain and stress in all cases. This is most likely due to the fact that the strain is calculated by one order of differentiation of the displacement, thus the interpolation function representing the displacement will always be one order higher than that of strain (Bathe, 1996; Fagan, 1992). Therefore, in a region characterised by a rapidly changing strain field, a converged mesh measured by displacement may not satisfy the same convergence criterion for the strain (Fagan, 1992; Viceconti, 2012).

In the non-linear simulations stresses converged earlier than strains. For specimen3 in particular, the stress started to converge at 40 μm (1.7% percentage difference) whereas the strain began to converge only at 20 μm (3.7% percentage difference). The early convergence of stress is most likely due to the elastic perfectly plastic constitutive equation used in the model, where the increase in strain does not induce the changes of stress in post-yield stage. The model with element size 34 μm of specimen2 failed to converge in terms of strain. Also, for specimen1 and specimen2, the convergence rate in strain fluctuated between models of 68 μm and 34 μm. This oscillation is likely due to the high stress and strain gradient inherent to the complex geometry of cancellous bones in this region, where the stress and strain does not converge asymptotically, rather they fluctuated towards a converged solution (Pointer, 2004). Moreover, because of the non-linear nature of the problem, the convergence of such FE models based on mesh refinement is not monotonically guaranteed (Bathe, 1996; Gu and Conte, 2003; Razavi et al., 2007). Therefore, the convergence behaviour of such models for nonlinear simulation has to be treated with caution. Nevertheless, the convergence tendency for the non-linear simulations appeared to follow a similar trend as that of the linear simulations: the displacement converged the fastest among the three parameters investigated due to its higher order nature.

One advantage of this study is that the parameters investigated were obtained at the same spatial location of each mesh refinement, much closer to the Patch test typically used to conduct the convergence study. Despite of these, there are a few limitations. First, in the present study, we investigated in full only the region where the highest

principal strain was predicted in each model; in principle, the convergence behaviour for other nodes might be different, as the node of highest strain value is not necessarily the location of the highest strain gradient (where the largest discretization error is expected). However, when we repeated the study for the HOMO-HEXA model of specimen1 at the location where the peak stress error was predicted, we reached identical conclusions. This should not come as a surprise, as all nodes investigated with the maximum strain criterion belong to the first five elements of highest stress error. However, this has to be treated with caution in the future. If the one's interest is the highest prediction value, then the convergence study using maximum value criterion might be sufficient; if one's interest is the overall model in predicting the local values, the convergence study should focus on the region with the highest stress error; Second, due to the global thresholding, the connectivity changes at each mesh refinement, altering the mesh topology, which strictly speaking violates the conditions for the Patch test. However, in each comparison, we performed the investigation using same BCs, mesh types, leaving the results differ only because of the discretization error and of minor mesh topology changes. Additional caution should be taken with the mesh convergence results for the HETE-HEXA models, as patch convergence theory does not strictly apply to heterogeneous materials; Third, although able to resolve the accurate geometry of cancellous bone tissue, the greyscale obtained from microCT, even after polynomial correction, is likely to be affected by beam hardening artefact, resulting in less accurate predictions of local TMD (Kazakia et al., 2008). Therefore, the convergence behaviour for such model may be further investigated using synchrotron radiation micro-computed tomography (SRµCT), which by using a monochromatic, high flux, parallel beam, is able to provide better signal-to-noise ratio and more accurate attenuation measurement than microCT.

The finest HOMO-HEXA mesh (10 µm, specimen3) required 430 GB of memory and two hours to solve using HPC. This is not an issue with the modern powerful computer resources. On the other hand, the non-linear model of the same size required 589 GB memory and approximately 38 hours to solve. The non-linear simulation requires that the load to be divided into several sub-steps and iterated by Newton-Raphson method (Bathe, 1996), which increases the computational cost. For the solution of such large models parallel computing combined with a nonlinear FE solver optimized for efficient parallelization is recommended (Christen et al., 2014).

The results of the current study confirm that linear elastic simulation of cancellous bones of HOMO-HEXAs, assuring convergence of the displacements, stress and strain by using an element size less than one quarter of the trabecular thickness (34-40 µm). This modelling framework can be used for future reference. However, HETE-HEXAs, represented with different local mineral distribution in each mesh refinement, converged only with a finer mesh (20 µm). Further investigation is needed by using more samples and different CT modalities. HOMO-TETRA models, by preserving the same geometry in each mesh refinement, showed faster convergence evidence than exhibited by HEXA models. Also considering the smoothed surface HOMO-TETRA models have better strain and stress prediction are expected than from HEXA models, and might be preferable to use in the future. But it is not until the models are validated with proper experiments that we can draw any useful conclusions. Nonlinear simulations on the other hand, do not always guarantee the convergence at the same voxel size converged in linear simulation. Therefore, a local convergence study should always be conducted before any further analysis of the model.

4.5. References

Bathe, K.-J.r., 1996. Finite element procedures. Prentice Hall, Englewood Cliffs, N.J.

Bayraktar, H.H., Morgan, E.F., Niebur, G.L., Morris, G.E., Wong, E.K., Keaveny, T.M., 2004. Comparison of the elastic and yield properties of human femoral trabecular and cortical bone tissue. J. Biomech. 37, 27-35.

Berdichevsky, V., Foster, D.J., 2003. On Saint-Venant's principle in the dynamics of elastic beams. Int J Solids Struct 40, 3293-3310.

Bouxsein, M.L., Boyd, S.K., Christiansen, B.A., Guldberg, R.E., Jepsen, K.J., Muller, R., 2010. Guidelines for assessment of bone microstructure in rodents using micro-computed tomography. J. Bone Miner. Res. 25, 1468-1486.

Chen, Y., Pani, M., Taddei, F., Mazza, C., Li, X., Viceconti, M., 2014. Large-scale finite element analysis of human cancellous bone tissue micro computer tomography data: a convergence study. J. Biomech. Eng. 136.

Christen, D., Webster, D.J., Muller, R., 2010. Multiscale modelling and nonlinear finite element analysis as clinical tools for the assessment of fracture risk. Philos T R Soc A 368, 2653-2668.

Christen, D., Zwahlen, A., Muller, R., 2014. Reproducibility for linear and nonlinear micro-finite element simulations with density derived material properties of the human radius. Journal of the mechanical behavior of biomedical materials 29, 500-507.

Currey, J.D., 1988. The effect of porosity and mineral content on the Young's modulus of elasticity of compact bone. J. Biomech. 21, 131-139.

Currey, J.D., 1999. What determines the bending strength of compact bone? J. Exp. Biol. 202, 2495-2503.

Depalle, B., Chapurlat, R., Walter-Le-Berre, H., Bou-Said, B., Follet, H., 2012. Finite element dependence of stress evaluation for human trabecular bone. Journal of the mechanical behavior of biomedical materials 18, 200-212.

Fagan, M.J., 1992. Finite element analysis : theory and practice. Longman Scientific & Technical;Wiley, Harlow, Essex, England.

Feldkamp, L.A., Goldstein, S.A., Parfitt, A.M., Jesion, G., Kleerekoper, M., 1989. The direct examination of three-dimensional bone architecture in vitro by computed tomography. J. Bone Miner. Res. 4, 3-11.

Gross, T., Pahr, D.H., Peyrin, F., Zysset, P.K., 2012. Mineral heterogeneity has a minor influence on the apparent elastic properties of human cancellous bone: a SRmuCT-based finite element study. Computer methods in biomechanics and biomedical engineering 15, 1137-1144.

Gu, Q., Conte, J.P., 2003. Convergence studies in nonlinear finite element response sensitivity analysis. Applications of Statistics and Probability in Civil Engineering, Vols 1 and 2, 297-304.

Guldberg, R.E., Hollister, S.J., Charras, G.T., 1998. The accuracy of digital image-based finite element models. J. Biomech. Eng. 120, 289-295.

Hollister, S.J., Brennan, J.M., Kikuchi, N., 1994. A homogenization sampling procedure for calculating trabecular bone effective stiffness and tissue level stress. J. Biomech. 27, 433-444.

Huiskes, R., Hollister, S.J., 1993. From structure to process, from organ to cell: recent developments of FE-analysis in orthopaedic biomechanics. J. Biomech. Eng. 115, 520-527.

Irons, B., Loikkanen, M., 1983. An Engineers Defense of the Patch Test. Int J Numer Meth Eng 19, 1391-1401.

Jansen, L.E., Birch, N.P., Schiffman, J.D., Crosby, A.J., Peyton, S.R., 2015. Mechanics of intact bone marrow. Journal of the mechanical behavior of biomedical materials 50, 299-307.

Kaynia, N., Soohoo, E., Keaveny, T.M., Kazakia, G.J., 2015. Effect of intraspecimen spatial variation in tissue mineral density on the apparent stiffness of trabecular bone. J. Biomech. Eng. 137.

Kazakia, G.J., Burghardt, A.J., Cheung, S., Majumdar, S., 2008. Assessment of bone tissue mineralization by conventional x-ray microcomputed tomography: comparison with synchrotron radiation microcomputed tomography and ash measurements. Med. Phys. 35, 3170-3179.

Keyak, J.H., Meagher, J.M., Skinner, H.B., Mote, C.D., Jr., 1990. Automated three-dimensional finite element modelling of bone: a new method. J. Biomed. Eng. 12, 389-397.

Ladd, A.J., Kinney, J.H., 1998. Numerical errors and uncertainties in finite-element modeling of trabecular bone. J. Biomech. 31, 941-945.

MacNeil, J.A., Boyd, S.K., 2008. Bone strength at the distal radius can be estimated from high-resolution peripheral quantitative computed tomography and the finite element method. Bone 42, 1203-1213.

Mirzaali, M.J., Jakob Schwiedrzik, J., Thaiwichai, S., Best, J.P., Michler, J., Zysset, P.K., Wolfram, U., 2015. Mechanical properties of cortical bone and their relationships with age, gender, composition and microindentation properties in the elderly. Bone.

Morgan, E.F., Bayraktar, H.H., Keaveny, T.M., 2003. Trabecular bone modulus-density relationships depend on anatomic site. J. Biomech. 36, 897-904.

Mulder, L., Koolstra, J.H., den Toonder, J.M., van Eijden, T.M., 2008. Relationship between tissue stiffness and degree of mineralization of developing trabecular bone. Journal of biomedical materials research. Part A 84, 508-515.

Niebur, G.L., Feldstein, M.J., Yuen, J.C., Chen, T.J., Keaveny, T.M., 2000. High-resolution finite element models with tissue strength asymmetry accurately predict failure of trabecular bone. J. Biomech. 33, 1575-1583.

Niebur, G.L., Yuen, J.C., Hsia, A.C., Keaveny, T.M., 1999. Convergence behavior of high-resolution finite element models of trabecular bone. J. Biomech. Eng. 121, 629-635.

Nuzzo, S., Peyrin, F., Cloetens, P., Baruchel, J., Boivin, G., 2002. Quantification of the degree of mineralization of bone in three dimensions using synchrotron radiation microtomography. Med. Phys. 29, 2672-2681.

Perez-Gonzalez, A., Iserte-Vilar, J.L., Gonzalez-Lluch, C., 2011. Interpreting finite element results for brittle materials in endodontic restorations. Biomedical engineering online 10, 44.

Pistoia, W., van Rietbergen, B., Laib, A., Ruegsegger, P., 2001. High-resolution three-dimensional-pQCT images can be an adequate basis for in-vivo microFE analysis of bone. J. Biomech. Eng. 123, 176-183.

Pistoia, W., van Rietbergen, B., Lochmuller, E.M., Lill, C.A., Eckstein, F., Ruegsegger, P., 2002. Estimation of distal radius failure load with micro-finite element analysis models based on three-dimensional peripheral quantitative computed tomography images. Bone 30, 842-848.

Pistoia, W., van Rietbergen, B., Lochmuller, E.M., Lill, C.A., Eckstein, F., Ruegsegger, P., 2004. Image-based micro-finite-element modeling for improved distal radius strength diagnosis: moving from bench to bedside. J. Clin. Densitom. 7, 153-160.

Pointer, J., 2004. Understanding Accuracy and Discretization Error in an FEA Model. ANSYS 7.1, 2004 Conference.

Razavi, H., Abolmaali, A., Ghassemieh, M., 2007. Invisible elastic bolt model concept for finite element analysis of bolted connections. J Constr Steel Res 63, 647-657.

Renders, G.A., Mulder, L., Langenbach, G.E., van Ruijven, L.J., van Eijden, T.M., 2008. Biomechanical effect of mineral heterogeneity in trabecular bone. J. Biomech. 41, 2793-2798.

Schileo, E., Taddei, F., Cristofolini, L., Viceconti, M., 2008. Subject-specific finite element models implementing a maximum principal strain criterion are able to estimate failure risk and fracture location on human femurs tested in vitro. J. Biomech. 41, 356-367.

Torcasio, A., Zhang, X., Duyck, J., van Lenthe, G.H., 2012. 3D characterization of bone strains in the rat tibia loading model. Biomechanics and modeling in mechanobiology 11, 403-410.

Ulrich, D., van Rietbergen, B., Weinans, H., Ruegsegger, P., 1998. Finite element analysis of trabecular bone structure: a comparison of image-based meshing techniques. J. Biomech. 31, 1187-1192.

van der Linden, J.C., Birkenhager-Frenkel, D.H., Verhaar, J.A., Weinans, H., 2001. Trabecular bone's mechanical properties are affected by its non-uniform mineral distribution. J. Biomech. 34, 1573-1580.

van Rietbergen, B., 2001. Micro-FE analyses of bone: state of the art. Adv. Exp. Med. Biol. 496, 21-30.

van Rietbergen, B., Majumdar, S., Pistoia, W., Newitt, D.C., Kothari, M., Laib, A., Ruegsegger, P., 1998. Assessment of cancellous bone mechanical properties from micro-FE models based on micro-CT, pQCT and MR images. Technol. Health Care 6, 413-420.

van Rietbergen, B., Weinans, H., Huiskes, R., Odgaard, A., 1995. A new method to determine trabecular bone elastic properties and loading using micromechanical finite-element models. J. Biomech. 28, 69-81.

van Ruijven, L.J., Mulder, L., van Eijden, T.M., 2007. Variations in mineralization affect the stress and strain distributions in cortical and trabecular bone. J. Biomech. 40, 1211-1218.

Vaughan, T.J., McCarthy, C.T., McNamara, L.M., 2012. A three-scale finite element investigation into the effects of tissue mineralisation and lamellar organisation in human cortical and trabecular bone. Journal of the mechanical behavior of biomedical materials 12, 50-62.

Viceconti, M., 2012. Multiscale modeling of the skeletal system. Cambridge University Press, Cambridge.

Wang, M., 2001. On the Necessity and Sufficiency of the Patch Test for Convergence of Nonconforming Finite Elements. Siam J Numer Anal 39, 363-384.

Wang, X.J., Chen, X.B., Hodgson, P.D., Wen, C.E., 2006. Elastic modulus and hardness of cortical and trabecular bovine bone measured by nanoindentation. T Nonferr Metal Soc 16, S744-S748.

Yeni, Y.N., Christopherson, G.T., Dong, X.N., Kim, D.G., Fyhrie, D.P., 2005. Effect of microcomputed tomography voxel size on the finite element model accuracy for human cancellous bone. J. Biomech. Eng. 127, 1-8.

Young, P.G., Beresford-West, T.B.H., Coward, S.R.L., Notarberardino, B., Walker, B., Abdul-Aziz, A., 2008. An efficient approach to converting three-dimensional image data into highly accurate computational models. Philos T R Soc A 366, 3155-3173.

Zienkiewicz, O.C., Zhu, J.Z., 1987. A simple error estimator and adaptive procedure for practical engineerng analysis International Journal for Numerical Methods in Engineering Volume 24, Issue 2, Int J Numer Meth Eng, pp. 337-357.

Chapter5

Validation of linear microFE models' predicted displacement using DVC

Summary

The validation of local mechanical properties in non-destructive micro-computed tomography (microCT) based finite element (microFE) model is challenging. Digital volume correlation (DVC) combined with microCT images can measure internal displacements and deformation of bone specimen and can provide experimental data for validation. In this study, two independent experimental setups were used to estimate the accuracy of the microFE models for local displacement predictions in two human and one bovine cancellous bone specimens. For human specimen three different boundary conditions (BCs) were used to predict the displacement field using homogeneous hexahedral microFE models and the BC leading to the most accurate results was applied to bovine specimen microFEs using different mesh generation scheme. The first two BCs were assigned according to force and displacement measurements of the testing jigs. Conversely, the displacements of the boundary nodes of the third BC were derived from DVC measurements of the corresponding layers. Results show excellent relationship between the numerical predictions (x) and the experiments (y) when using BC derived from the DVC measurements (human Specimen1, U_Z: y=0.99x+0.0001, RMSE: 0.001 mm; human Specimen2, U_Z: y=0.98x-0.005, RMSE: 0.011 mm), whereas only poor correlation was found using BCs according to experiment setups, especially if the specimen rotated during the planned uniaxial compression. When applying the third type of BC (BC leading to the best results) to bovine specimen microFEs, similar results were found (homogeneous hexahedral model, U_Z: y=x+0.0002, RMSE: 0.001 mm; heterogeneous hexahedral model, U_Z: y=x-0.0002, RMSE: 0.001 mm; homogeneous tetrahedral model, U_Z: y=x+0.0003, RMSE: 0.001 mm). In conclusion, microFE models predict accurately the displacement field, when the correct boundary conditions are applied. By including the local bone lamellar heterogeneity (*heterogeneous hexahedral model*) and using smoothed boundary (*homogeneous tetrahedral model*), it has only a minus impact on the accuracy of the local displacement prediction compared to the *homogeneous hexahedral model*. Part of this chapter was submitted to JMBBM for publication as: Chen Y, Dall'Ara E, Sales E, Manda K, Wallce R, Pankaj P, Viceconti M. MicroCT Based Finite Element Models of Cancellous Bone Predicted Accurately Displacement Computed by Elastic Registration: A Validation Study. The manuscript is currently under revision.

Keywords: MicroCT, microFE, cancellous bone, DVC, validation

5.1. Introduction

Bone tissue is a complex hierarchical material (Cowin, 2001). In order to address clinical and preclinical problems, it is important to study bone at the spatial scale that allows the most appropriate characterization of its mechanical behaviour. At the tissue scale, the interaction between bone mechanical stimuli and the biological function driven by the cell activity becomes more evident (Viceconti, 2012). The microCT based finite element (microFE) method has become a popular tool for non-destructive structural analysis of cancellous bone tissue (Hollister et al., 1994; van Rietbergen et al., 1995; Verhulp et al., 2008). The method involves the direct conversion of the 3D voxels of micro-computed tomography (microCT) images of the bone tissue (Feldkamp et al., 1989) into equally shaped and sized hexahedral elements. As microCT imaging has the ability to accurately resolve bone morphology in great detail (Bouxsein et al., 2010), specimen-specific microFE models that represent the structure of the specimen can be generated (Ulrich et al., 1998).

Every modelling method requires, before it can be considered reliable, a complete verification, validation, and uncertainty quantification assessment (Anderson et al., 2007). A systematic verification analysis of microFE models of bone tissue was recently published (Chen et al., 2014). However, for validation, the number of published reports is limited. While the predicted apparent properties (e.g. stiffness, strength) of each specimen can be compared with accurate experimental measurements (Christen et al., 2013; Pistoia et al., 2002; Wolfram et al., 2010; Yeni and Fyhrie, 2001), the validation of such models for local predictions is not trivial.

One possible approach is to use a full-field method, such as Digital Volume Correlation (DVC) techniques, to extract displacement or strain fields from repeated microCT scans performed during stepwise-compression experiments. In every validation study the boundary conditions (BCs) imposed in the model should be the same as in the experiments. However, even if we can measure accurately the resultant force applied, or the total displacement imposed during the stepwise compression test, the aspect ratio of the specimens typically used in these tests might be too small to assume valid Saint-Venant's Principle. If this is the case, it is not enough to reproduce in the model the loading resultant, but we need to consider also how such forces are locally distributed. To the authors' knowledge there are two studies in the literature that used DVC

measurements to validate microFE models displacement predictions on cancellous bone specimens, and their results are somehow inconclusive. Recently, Zhu et al. (2015) compared the predictions of microCT based tetrahedral homogeneous models to DVC measurements for bovine bone interdigitated with acrylic cement and a cellular foam samples. Only qualitative comparison between models and DVC displacement only along the loading direction was reported. Zauel et al. (2006) was the first to use a DVC approach based on the one reported in (Bay et al., 1999) to quantitatively validate a linear elastic microFE model of cancellous bone. They found very good correlation in displacement measured along the major loading direction (R^2 from 0.91 to 0.97, slopes between 0.93 and 0.98), but only poor correlation for transverse displacements (R^2 from 0.29 to 0.60, slopes between 0.33 and 0.88). This result is surprising as the precision error of their DVC method is isotropic (Dall'Ara et al., 2014; Zauel et al., 2006) and the predictions of the microFE models should not be affected by the loading direction unless strong local anisotropy needs to be included in the models. The findings reported by Zauel et al. (2006) suggest that homogeneous isotropic microFE models is not reliable in predicting transverse displacement. Therefore, we need to further explore the ability of predicting local displacement from microFE models, widely used in the research community to estimate bone properties at the tissue levels.

There is conclusive evidence showing that bone is constantly remodelled (Currey, 1999), thus each volume of tissue might have a different level of mineralisation and consequently exhibit significantly difference mechanical properties. Some studies suggested that incorporating the bone heterogeneity into microFE models is likely to affect the prediction of cancellous bone mechanical properties (Kaynia et al., 2015; Renders et al., 2008; van der Linden et al., 2001; van Ruijven et al., 2007). In addition, boundary recovery mesh is supposed to compensate for the loss of trabecular connections and potentially predict more accurately the strain field because of smoothed surface (Boyd and Muller, 2006; Leung et al., 2008; Muller and Ruegsegger, 1995; Ulrich et al., 1998). It is worthwhile investigating the impact on the local mechanical properties the assumptions of these models bring about over traditional homogeneous hexahedral model, which has not been done before. Therefore, the goal of this study was to challenge the displacements predicted by different microCT-based microFE models from different cancellous bone specimens tested with two independent experimental setups by comparison with a novel DVC based approach.

5.2. Materials and methods

Two independent testing procedures were used in order to assess the sensitivity of the validation approach for two different experimental protocols and input images and to extend the validity of the results. In both cases similar workflows were used (Fig.5.1).
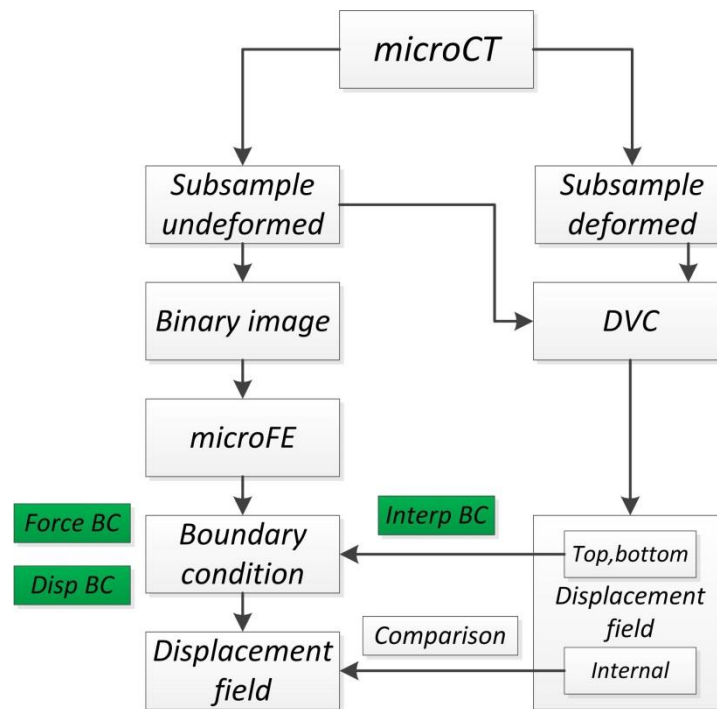
Fig.5.1. Workflow of the study

5.2.1. Experiment test and DVC measurement

The experimental set-up, the preparation of the specimens, and the DVC measurements methodology were fully detailed in Chapter 3.

5.2.2. MicroFE models

The microFE models verified in Chapter 4 were used in this validation study. To be specific: linear elastic homogeneous hexahedral models were generated for all specimens, with an element size of 34.44 μm for Specimen1 and Specimen2 and 19.84 μm for Specimen3; for Specimen3, we generated a heterogeneous hexahedral model with element size of 19.84 μm, and an homogeneous tetrahedral model with average element size selected so to obtain a mesh with a number of degrees of freedom (NDOF) comparable to the homogeneous hexahedral model. To be consistent throughout the thesis, the homogeneous hexahedral model, heterogeneous hexahedral model and homogeneous tetrahedral model are thereafter referred to as HOMO-HEXA, HETE-

HEXA and HOMO-TETRA respectively. Models' generation is fully detailed in Chapter 4.

5.2.3. Boundary conditions

Three sets of BCs were used for linear elastic simulations in order to replicate the BCs measured in experiments: "force BCs", "displacement BCs" and "interpolated BCs". All types of BCs were applied to HOMO-HEXA of three specimens where possible. The BC leading to the most accurate displacement prediction from HOMO-HEXA was applied to HETE-HEXA and HOMO-TETRA of specimen3, in order to compare the prediction accuracy of different mesh type. Please refer to Chapter 3 for more details on the definition of the boundary conditions.

5.2.4. Comparison between experimental and computational results

The DVC procedure provides the displacements of the centroid of a subgroup of the hexahedral microFE elements. In fact, only some of the nodes of the DVC grid (with nodal spacing of 12 or 25 voxels according to the specimen) lay in the bone elements of microFE. Therefore, for the HEXA models, the bone element centroid displacements were extracted and compared with the DVC grid displacements. On the other hand, due to the irregular shape and size of the elements used in the HOMO-TETRA, the mapping relationship of the DVC grids and bone elements in the model was first spotted and the coordinates of these DVC grid nodes were extracted. Then the model displacements were interpolated from these coordinates using element shape function and then compared with the corresponding DVC grid displacements. All comparisons were limited to the middle 80% of the specimen to avoid boundary effects. Following this procedure, we obtained the following number of comparison pairs: HOMO-HEXA: 4041 for Specimen1, 3671 for Specimen2 and 589 for Specimen3; HETE-HEXA: 597 for Specimen3; HOMO-TETRA: 625 for Specimen3.

5.2.5. Statistics

Any observation with Cook's distance (Fox and Long, 1990) larger than five times the mean Cook's distance was considered as outliers and removed from the analysis. This approach removed 1% to 4% points for each analysis. The comparison of displacement for microFE models and experiments was performed using linear regression, where the slope and intercept of the equation as well as coefficient of determination (R^2) were reported. For each comparison the Root Mean Square Error (RMSE), the RMSE divided

by the maximum experiment value (RMSE%), the largest difference between microFE prediction and DVC measurements (Max.error), the Max.error divided by the maximum experimental value (Max.error%), and the intra-class correlation (ICC which describes how strongly two groups of data resemble each other, with 0 being poor and 1 being excellent) were computed. All statistics have been done in SPSS (IBM SPSS Statistics for Windows, Version 21.0. Armonk, NY: IBM Corp.). The number of comparison pairs remained in each analysis was reported in Table.5.1 and Table.5.2.

5.3. Results

All coefficients calculated from the correlations between predicted and measured displacements are reported in Table.5.1 and Table.5.2.

The displacement predicted by HOMO-HEXAs with three different BCs and DVC measurements were all significantly linearly correlated (p<0.01) (Table.5.1). However, microFE models with "force BCs" and "displacement BCs" were far from the 1:1 relationship, underlined by the low ICCs (from 0.02 to 0.42). Conversely, microFE models with "interpolated BCs" lead to excellent correlations, with slope close to one (range: 0.98 to 1.07), intercept close to zero (range: -0.006 to 0.006 mm), high R^2 (range: 0.97 to 0.99) and high ICC (0.99). In that case similar results were found for the three specimens (Fig.5.2), with RMSE% lower than 2.5% (with maximum equal to 2.4% for predictions of Uz for Specimen2 and of Uy for Specimen3) and Max.err% lower than 11% (with maximum equal to 10.7% for predictions of Ux for Specimen2). These models overall predicted better U_Z (displacements along the major compression direction) with RMSE% from 1.1% to 2.4% and Max.err% from 3.5% to 5.6%) compared to the displacements along the transverse directions (RMSE% from 1.7% to 2.1% and Max.err% from 5.6% to 10.7% for U_X and RMSE% from 1.7% to 2.4% and Max.err% from 5.2% to 7.1% for U_Y). The best correlation was found for predictions of U_Z for Specimen3, with slope equal to 1 and intercept equal to 0.0002 mm. All the outputs from HOMO-HEXAs of three specimens using different BCs were summarized in Table.5.1.

The BC leading to the most accurate displacement ("interpolated BCs" in this study with the high ICCs, high R^2, slope close to one, intercept close to zero) was applied to HETE-HEXA and HOMO-TETRA for Specimen3. Overall, all three mesh types using "interpolated BCs" lead to accurate and consistent results compared to DVC

measurements, with slope close to one (range: 1.00 to 1.07), intercept close to zero (range: -0.002 to 0.0003 mm), high R^2 (range: 0.97 to 0.99) and high ICC (0.99). Also in this case, similar results were found by using three different mesh types (Fig.5.3), with RMSE% lower than 2.6% (with maximum equal to 2.6% for predictions of Uy for homogeneous tetrahedral model) and Max.err% lower than 7.5% (with maximum equal to 7.2% for predictions of Uy for homogeneous tetrahedral model). These models overall predicted better U_Z (displacements along the major compression direction) with RMSE% from 1.4% to 1.5% and Max.err% from 4.4% to 4.8%) compared to the displacements along the transverse directions (RMSE% from 2.0% to 2.1% and Max.err% from 5.0% to 5.6% for U_X and RMSE% from 2.4% to 2.6% and Max.err% from 6.7% to 7.2% for U_Y). All the outputs from these three mesh types of Specimen3 were summarized in Table.5.2.

In Fig.5.4 and Fig.5.5 comparisons between the predicted and measured vertical displacement for the "interpolated BCs" are reported. From those graph it can be noted that all specimens seemed to rotate to some extent during the experiments, slightly far away from uniaxial compression test, especially for Specimen1 and Specimen2.

Table.5.1. *Correlation between HOMO-HEXAs prediction and DVC measurement*

Specimen	BCs	Direction	Number of points (Remaining percentage)	R^2	Slope	Intercept (mm)	ICC	RMSE (mm)	RMSE%	Max.err (mm)	Max.err%
Specimen1	Force	U_X	3920(97%)	0.77	33.81	-0.040	0.02	0.036	54.1%	0.066	99.3%
		U_Y	3923(97%)	0.55	15.48	0.050	0.02	0.035	61.3%	0.057	100.1%
		U_Z	3930(97%)	0.47	11.41	0.100	Na	0.082	80.3%	0.103	101.4%
	Disp	U_X	3951(98%)	0.06	0.30	-0.030	0.18	0.027	38.7%	0.070	92.6%
		U_Y	3915(97%)	0.41	0.43	0.050	0.08	0.078	136.6%	0.099	173.8%
		U_Z	3947(98%)	0.02	0.05	0.080	0.01	0.154	152.2%	0.207	203.8%
	Intep	U_X	3890(96%)	0.99	1.00	<0.001	0.99	0.001	1.7%	0.005	7.4%
		U_Y	3888(96%)	0.99	1.01	<0.001	0.99	0.001	1.7%	0.004	7.1%
		U_Z	3916(97%)	0.99	0.99	<0.001	0.99	0.001	1.1%	0.004	3.5%
Specimen2	Force	U_X	3612(98%)	0.28	-29.18	0.110	Na	0.103	61.1%	0.169	100.0%
		U_Y	3603(98%)	0.27	-52.88	-0.210	Na	0.167	58.7%	0.284	99.9%
		U_Z	3619(99%)	<0.01	-3.04	0.280	Na	0.308	70.1%	0.440	101.2%
	Disp	U_X	3633(99%)	0.05	0.93	0.100	0.02	0.104	61.7%	0.171	101.2%
		U_Y	3638(99%)	0.52	-3.61	-0.240	Na	0.149	52.6%	0.291	102.2%
		U_Z	3619(99%)	<0.01	-0.21	0.280	Na	0.363	82.3%	0.537	122.0%
	Intep	U_X	3511(96%)	0.99	1.03	-0.006	0.99	0.003	2.0%	0.018	10.7%
		U_Y	3516(96%)	0.99	1.02	0.006	0.99	0.005	1.6%	0.015	5.2%
		U_Z	3531(96%)	0.99	0.98	-0.005	0.99	0.011	2.4%	0.025	5.6%
Specimen3	Force	U_X	586(99%)	0.07	1.48	0.030	0.02	0.035	58.0%	0.060	98.3%
		U_Y	574(97%)	0.03	1.13	0.030	0.01	0.028	58.2%	0.049	100.5%
		U_Z	577(98%)	0.32	1.55	-0.003	0.42	0.016	28.7%	0.039	72.1%
	Intep	U_X	570(97%)	0.99	1.07	-0.002	0.99	0.001	2.1%	0.003	5.6%
		U_Y	573(97%)	0.97	1.03	-0.001	0.99	0.001	2.4%	0.003	7.1%
		U_Z	568(96%)	0.99	1.00	<0.001	0.99	0.001	1.5%	0.002	4.5%

* Correlations are all significant at P < 0.01; Na: ICC not reliable

Table.5.2. Correlation between different model prediction and DVC measurement using "interpolated BC" for Specimen3

Specimen	Mesh types	Direction	Number of points (Remaining percentage)	R^2	Slope	Intercept (mm)	ICC	RMSE (mm)	RMSE%	Max.err (mm)	Max.err%
Specimen3	HOMO HEXA	U_X	570(97%)	0.99	1.07	-0.002	0.99	0.001	2.1%	0.003	5.6%
		U_Y	573(97%)	0.97	1.03	-0.001	0.99	0.001	2.4%	0.003	7.1%
		U_Z	568(96%)	0.99	1.00	<0.001	0.99	0.001	1.5%	0.002	4.5%
	HETE HEXA	U_X	576(96%)	0.99	1.07	-0.002	0.99	0.001	2.0%	0.003	5.4%
		U_Y	576(96%)	0.97	1.03	-0.001	0.99	0.001	2.5%	0.003	6.7%
		U_Z	576(96%)	0.99	1.00	<0.001	0.99	0.001	1.4%	0.002	4.4%
	HOMO TETRA	U_X	601(96%)	0.99	1.07	-0.002	0.99	0.001	2.0%	0.003	5.0%
		U_Y	604(97%)	0.97	1.03	-0.001	0.99	0.001	2.6%	0.004	7.2%
		U_Z	604(97%)	0.99	1.00	<0.001	0.99	0.001	1.5%	0.003	4.8%

* Correlations are all significant at P < 0.01
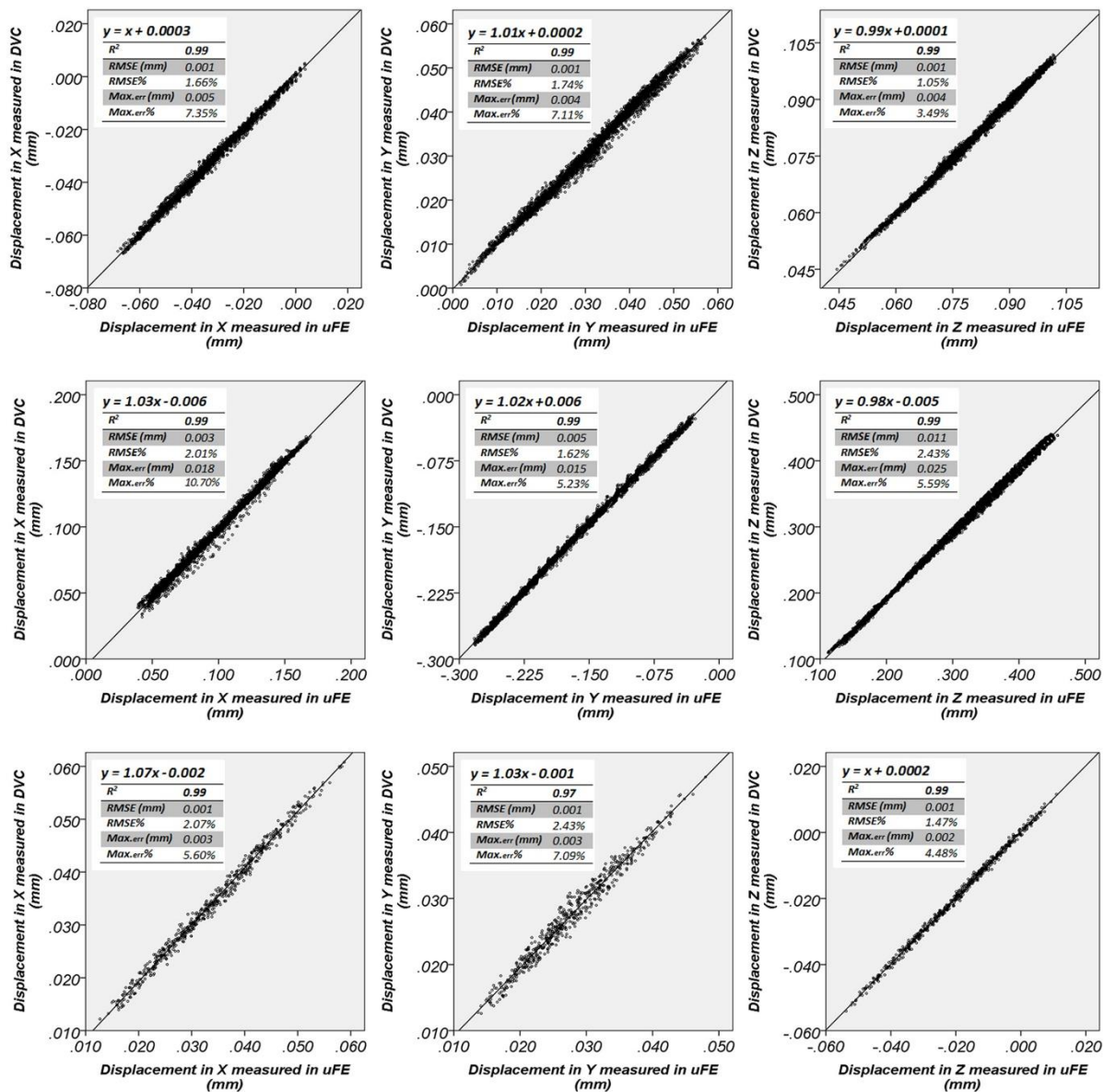
Fig.5.2. *Displacement predicted by HOMO-HEXAs plotted against DVC measurement using "interpolated BC" for Specimen1 (top), Specimen2 (middle) and Specimen3 (bottom).*
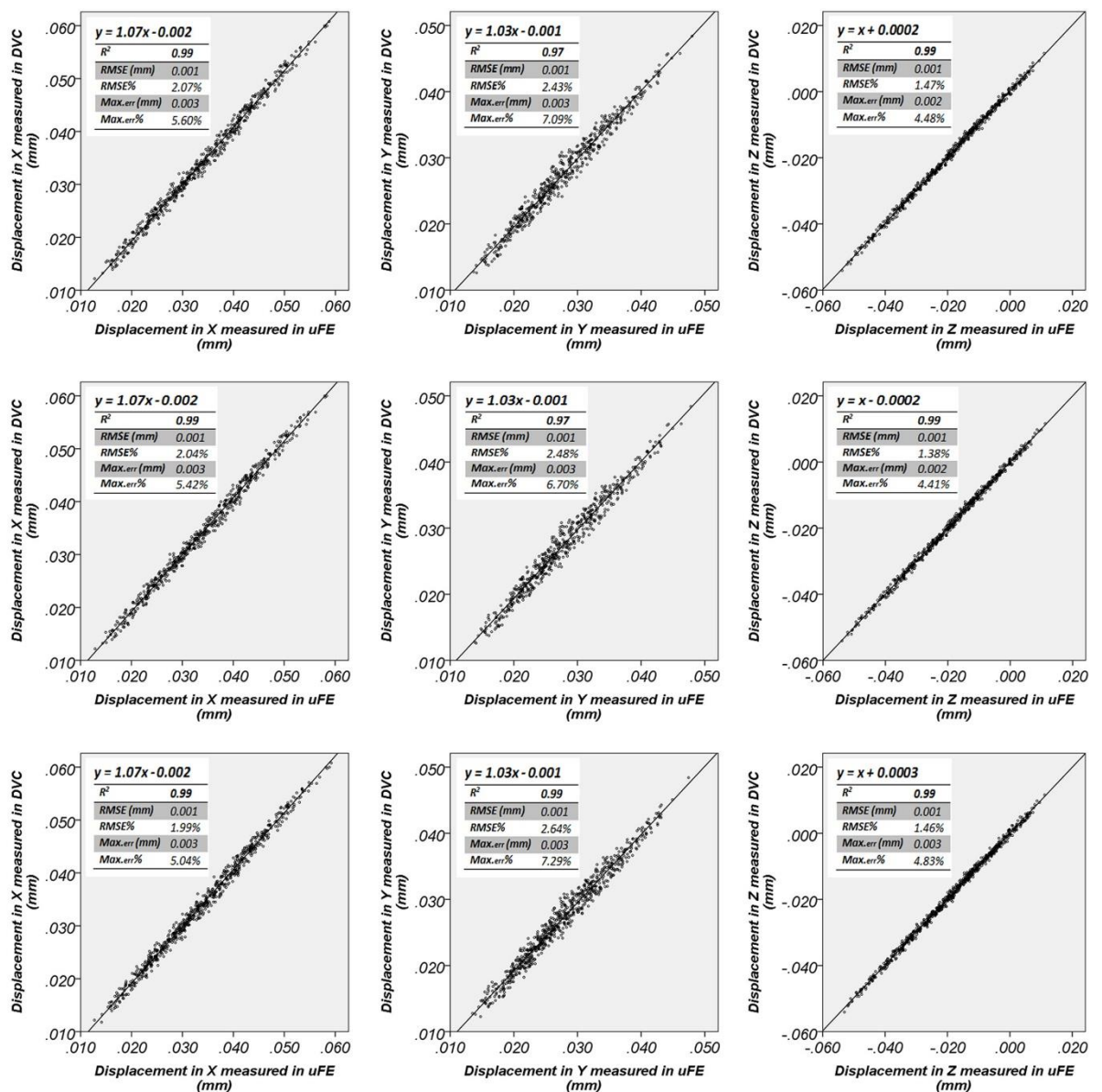
Fig.5.3. *Displacement predicted by three different models plotted against DVC measurement using "interpolated BC" for HOMO-HEXA (top), HETE-HEXA (middle) and HOMO-TETRA in Specimen3(bottom).*
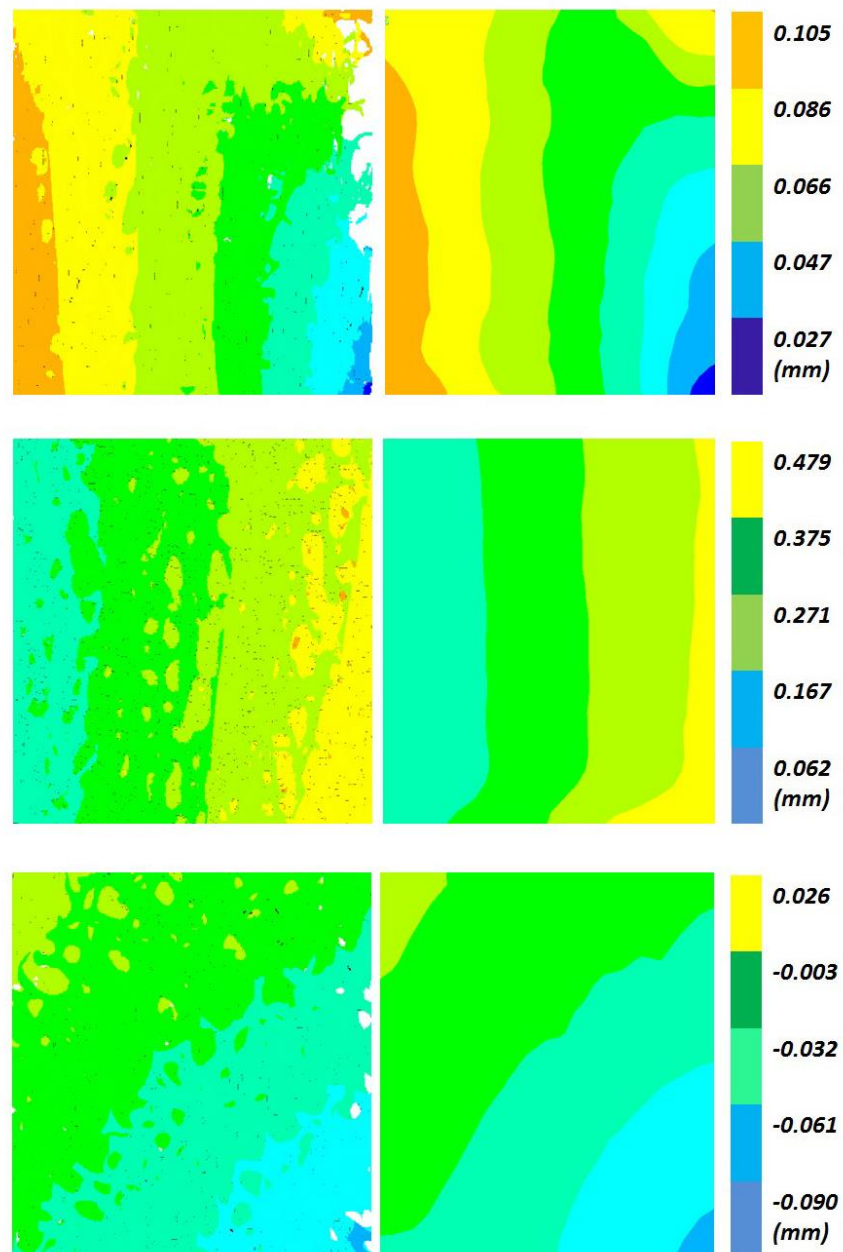
Fig.5.4. *Contour plot of the displacement along the loading direction viewed in the coronal plane for Specimen1 (top), Specimen2 (middle) and Specimen3 (bottom). Predictions from the HOMO-HEXAs with "interpolated BCs" (left) and DVC measurements (right) are reported.*
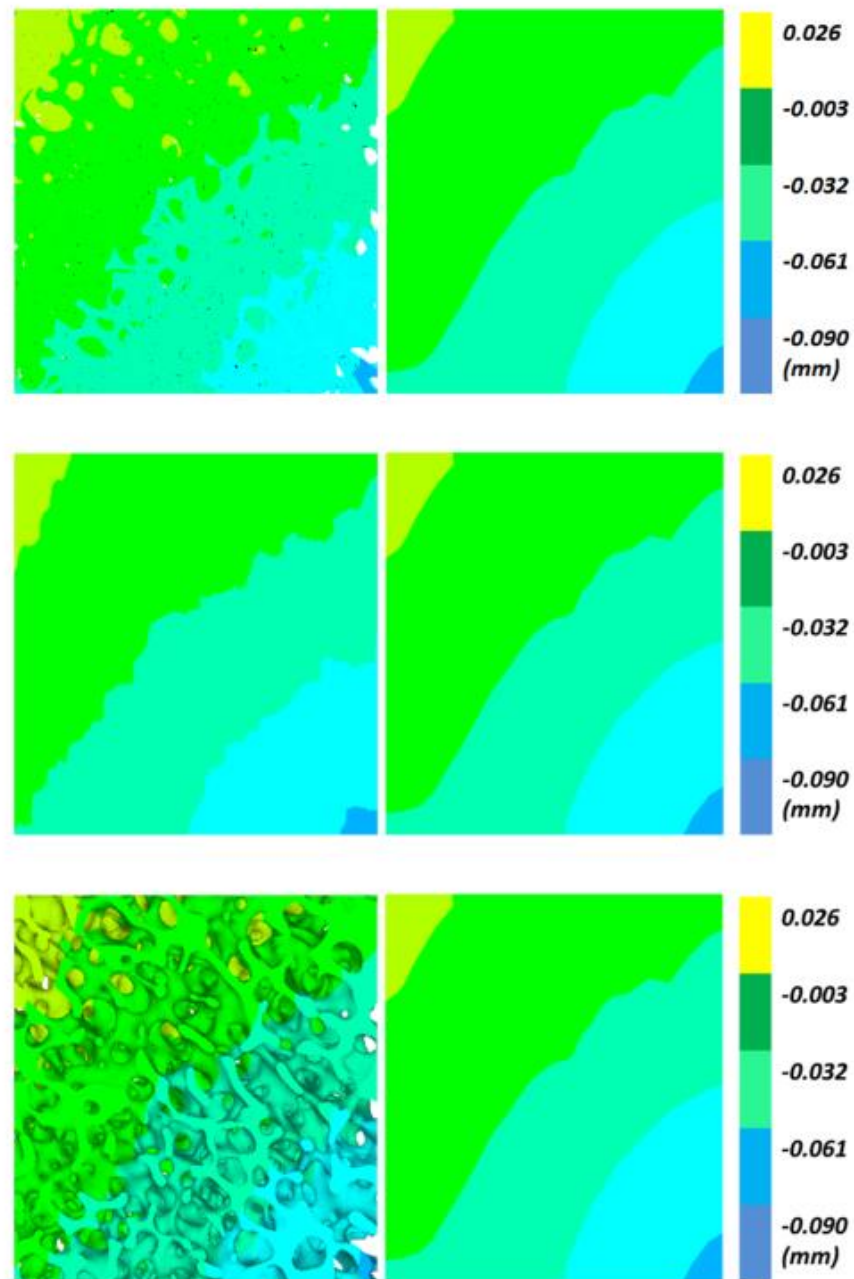
Fig.5.5. *Contour plot of the displacement along the loading direction viewed in the coronal plane for HOMO-HEXA (top), HETE-HEXA (middle) and HOMO-TETRA (bottom) in Specimen3. Predictions from the microFEs with "interpolated BCs" (left) and DVC measurements (right) are reported.*

5.4. Discussion

The aim of the present study was to develop a procedure that could be applied to validate microFE displacement prediction with DVC measurements. This work focused on studying the effect of different BCs applied to the models using different experimental set-ups and also the effect of local displacement prediction using different mesh type by applying the most realistic BC, the "interpolated BC" in this study.

MicroFEs using "force BCs" and "displacement BCs" in general predicted displacement poorly compared to DVC measurement. It should be noted however, it is very challenging to design loading jigs that allow a good control of the BCs with the requirements for perfect uniaxial compression test within a microCT system (non-parallel surfaces of the specimens, manufactured with lower stiffness radio-transparent materials, etc. – factors that may all leads to non-uniaxial compression loading in reality; refer to Chapter3 for more details). As the BCs assigned to microFEs were based on the nominal experimental conditions (i.e. perfectly flat and parallel surfaces of the sample and loading plates, compression along the axis of the specimen, etc.), the mismatch is probably due to the unexpected rotation of the specimens during the mechanical testing, visible from the DVC measurements (Fig.5.4-5.5). As soon as the BCs are not well reproduced in the microFE, a large variability in the predictions was noted, making "force BCs" and "displacement BCs" not reliable in these cases. Conversely, microFE models using "interpolated BCs" provided excellent correlation with the experimental results in all three directions, also for small compressive loads. The excellent correlations found for the predictions of displacements along the major loading direction (R^2 equal to 0.99, slope from 0.98 to 1.00, intercept from -5 to ~0 μm, ICC equal to 0.99) is comparable to what was reported by Zauel et al. (2006) on a similar study performed on two human cancellous specimens (R^2 from 0.91 to 0.97; slope from 0.93 to 0.98; intercept from 79 to 145 μm). However, in that case worse predictions were found for the transverse directions (R^2 from 0.29 to 0.60; slope from 0.33 to 0.88; intercept from -954 to 40 μm) while in the present study they were excellent, even if with slightly larger scatter (R^2 from 0.97 to 0.99; slope from 1.00 to 1.07; intercept from -6 to 6 μm). The small differences between the predictions of the displacements along the different directions underline that the assumption of isotropic material property for every element in case of microFE models is well posed. The improvement in the predictions of the displacements along the transverse directions in this study compared

to the previous report (Zauel et al., 2006) may be due to the improved accuracy of the DVC method used in this work (Dall'Ara et al., 2014; Palanca et al., 2015).

Comparable results were found amongst three different mesh types used in this study (with similar slope, intercept, RMSE% and Max.err% in Table.5.2). This once again showed the robustness and consistency of the method. While the results of this study clearly show the good accuracy of microFE models in predicting local displacements, further analyses should be done for studying the predictions of strain, which can play a fundamental role in the theory of mechano-regulated bone remodelling (Gedrange et al., 2008). However, the accuracy and precision of the current experimental methods for strain measurement in each element (as small as 10-20 microns) when modelling whole bone biopsy (10-20mm large) are too low (Grassi and Isaksson, 2015; Palanca et al., 2015). Therefore, the research community should focus first on the development of proper experimental protocols for such analyses.

Our results illustrate the strength of the current method: even with difficulty in controlling an ideal uniaxial compression test of the specimen in microCT, the "interpolated BC" is still able to produce the accurate results by catching the displacement distribution at the specimens' surfaces; also, it has to be noticed that this was found valid for both independent experimental protocols and for different specimens, scanned and subsampled with different voxel size and meshed with different material properties and element types, underlying the robustness of the method. In conclusion, microFE models with "interpolated BCs" predict local displacements in cancellous bone samples with excellent accuracy in all spatial directions. In addition, by including the local heterogeneity driven by the bone remodelling process (HETE-HEXA) and using smoothed boundary (HOMO-TETRA), it has only a minus impact on the local displacement prediction compared to the HOMO-HEXA – the mesh generation scheme widely used in the microCT based cancellous bone analysis. Although three mesh types produced comparably accurate displacement field, it remains to be investigated on how sensitive the models are for strain predictions - the derivative of displacement which is supposed to propagate to a larger extent of difference than the displacement – based on different idealization of each mesh type. Moreover, if larger compressive loads would be analysed, nonlinear models (Harrison et al., 2013) would become fundamental in order to simulate the local yielding of the trabecular bone structure.

5.5. References

Anderson, A.E., Ellis, B.J., Weiss, J.A., 2007. Verification, validation and sensitivity studies in computational biomechanics. Computer methods in biomechanics and biomedical engineering 10, 171-184.

Bouxsein, M.L., Boyd, S.K., Christiansen, B.A., Guldberg, R.E., Jepsen, K.J., Muller, R., 2010. Guidelines for assessment of bone microstructure in rodents using micro-computed tomography. J. Bone Miner. Res. 25, 1468-1486.

Boyd, S.K., Muller, R., 2006. Smooth surface meshing for automated finite element model generation from 3D image data. J. Biomech. 39, 1287-1295.

Chen, Y., Pani, M., Taddei, F., Mazza, C., Li, X., Viceconti, M., 2014. Large-scale finite element analysis of human cancellous bone tissue micro computer tomography data: a convergence study. J. Biomech. Eng. 136.

Christen, D., Melton, L.J., 3rd, Zwahlen, A., Amin, S., Khosla, S., Muller, R., 2013. Improved fracture risk assessment based on nonlinear micro-finite element simulations from HRpQCT images at the distal radius. J. Bone Miner. Res. 28, 2601-2608.

Cowin, S.C., 2001. Bone mechanics handbook, 2nd ed. CRC, Boca Raton, Fla. ; London.

Currey, J.D., 1999. What determines the bending strength of compact bone? J. Exp. Biol. 202, 2495-2503.

Dall'Ara, E., Barber, D., Viceconti, M., 2014. About the inevitable compromise between spatial resolution and accuracy of strain measurement for bone tissue: a 3D zero-strain study. J. Biomech. 47, 2956-2963.

Feldkamp, L.A., Goldstein, S.A., Parfitt, A.M., Jesion, G., Kleerekoper, M., 1989. The direct examination of three-dimensional bone architecture in vitro by computed tomography. J. Bone Miner. Res. 4, 3-11.

Fox, J., Long, J.S., 1990. Modern methods of data analysis. Sage Publications, Newbury Park, Calif.

Gedrange, T., Mai, R., Weingaertner, J., Hietschold, V., Bourauel, C., Pradel, W., Lauer, G., Proff, P., 2008. Finite element representation of bone substitute remodelling in the jaw bone. Biomed. Tech. (Berl.) 53, 220-223.

Grassi, L., Isaksson, H., 2015. Extracting accurate strain measurements in bone mechanics: A critical review of current methods. Journal of the mechanical behavior of biomedical materials 50, 43-54.

Harrison, N.M., McDonnell, P., Mullins, L., Wilson, N., O'Mahoney, D., McHugh, P.E., 2013. Failure modelling of trabecular bone using a non-linear combined damage and

fracture voxel finite element approach. Biomechanics and modeling in mechanobiology 12, 225-241.

Hollister, S.J., Brennan, J.M., Kikuchi, N., 1994. A homogenization sampling procedure for calculating trabecular bone effective stiffness and tissue level stress. J. Biomech. 27, 433-444.

Kaynia, N., Soohoo, E., Keaveny, T.M., Kazakia, G.J., 2015. Effect of intraspecimen spatial variation in tissue mineral density on the apparent stiffness of trabecular bone. J. Biomech. Eng. 137.

Leung, S.Y., Browne, M., New, A.M., 2008. Smooth surface micro finite element modelling of a cancellous bone analogue material. Proc. Inst. Mech. Eng. H 222, 145-149.

Muller, R., Ruegsegger, P., 1995. Three-dimensional finite element modelling of non-invasively assessed trabecular bone structures. Med. Eng. Phys. 17, 126-133.

Palanca, M., Tozzi, G., Cristofolini, L., Viceconti, M., Dall'Ara, E., 2015. Three-dimensional local measurements of bone strain and displacement: comparison of three digital volume correlation approaches. J. Biomech. Eng. 137.

Pistoia, W., van Rietbergen, B., Lochmuller, E.M., Lill, C.A., Eckstein, F., Ruegsegger, P., 2002. Estimation of distal radius failure load with micro-finite element analysis models based on three-dimensional peripheral quantitative computed tomography images. Bone 30, 842-848.

Renders, G.A., Mulder, L., Langenbach, G.E., van Ruijven, L.J., van Eijden, T.M., 2008. Biomechanical effect of mineral heterogeneity in trabecular bone. J. Biomech. 41, 2793-2798.

Ulrich, D., van Rietbergen, B., Weinans, H., Ruegsegger, P., 1998. Finite element analysis of trabecular bone structure: a comparison of image-based meshing techniques. J. Biomech. 31, 1187-1192.

van der Linden, J.C., Birkenhager-Frenkel, D.H., Verhaar, J.A., Weinans, H., 2001. Trabecular bone's mechanical properties are affected by its non-uniform mineral distribution. J. Biomech. 34, 1573-1580.

van Rietbergen, B., Weinans, H., Huiskes, R., Odgaard, A., 1995. A new method to determine trabecular bone elastic properties and loading using micromechanical finite-element models. J. Biomech. 28, 69-81.

van Ruijven, L.J., Mulder, L., van Eijden, T.M., 2007. Variations in mineralization affect the stress and strain distributions in cortical and trabecular bone. J. Biomech. 40, 1211-1218.

Verhulp, E., van Rietbergen, B., Muller, R., Huiskes, R., 2008. Indirect determination of trabecular bone effective tissue failure properties using micro-finite element simulations. J. Biomech. 41, 1479-1485.

Viceconti, M., 2012. Multiscale modeling of the skeletal system. Cambridge University Press, Cambridge.

Wolfram, U., Wilke, H.J., Zysset, P.K., 2010. Valid micro finite element models of vertebral trabecular bone can be obtained using tissue properties measured with nanoindentation under wet conditions. J. Biomech. 43, 1731-1737.

Yeni, Y.N., Fyhrie, D.P., 2001. Finite element calculated uniaxial apparent stiffness is a consistent predictor of uniaxial apparent strength in human vertebral cancellous bone tested with different boundary conditions. J. Biomech. 34, 1649-1654.

Zauel, R., Yeni, Y.N., Bay, B.K., Dong, X.N., Fyhrie, D.P., 2006. Comparison of the linear finite element prediction of deformation and strain of human cancellous bone to 3D digital volume correlation measurements. J. Biomech. Eng. 128, 1-6.

Zhu, M.L., Zhang, Q.H., Lupton, C., Tong, J., 2015. Spatial resolution and measurement uncertainty of strains in bone and bone-cement interface using digital volume correlation. Journal of the mechanical behavior of biomedical materials 57, 269-279.

Chapter6

Local mechanical property prediction: comparison among different microCT-based finite element models

Summary

Three different 3D micro-computed tomography (microCT) based finite element (microFE) models (*homogenous hexahedral model, heterogeneous hexahedral model and homogeneous tetrahedral model*) have been reported in the literature for the estimation of bone mechanical properties at tissue level. Using DVC experimental measurements, we validated these three modelling methods in term of displacement; all three performed similarly well. As no experimental full-field measurement is available to validate strain predictions, in this chapter we will compare the strain fields predicted by the three methods when applied to the same specimen and the same boundary conditions. Therefore, the goal of this study is to compare their strain fields two by two, in order to explore the effect of specific idealisations on the prediction of strains. *homogenous hexahedral* and *heterogeneous hexahedral models* different only in the idealisation of how the tissue elastic properties are mapped; *homogenous hexahedral* and *homogenous tetrahedral models* different only for how the boundary is idealised; *heterogeneous hexahedral* and *homogenous tetrahedral models* differ for both aspects, and can inform whether the heterogeneous mapping of the elastic properties can mitigate the effects of less accurate boundary recovery in hexahedral model, where compared to tetrahedral model. The results show that differences in mechanical properties prediction exist locally between two hexahedral models, because of different element connectivity. Although being able to catch the local mineral density distribution of the bone tissue, at 20 µm of spatial resolution the advantage of *heterogeneous hexahedral model* over traditionally less computational expensive *homogenous hexahedral model* seems minimal. *Homogeneous tetrahedral models* tend to predict higher and smoother strain in regions with high strain than both *homogenous hexahedral* and *heterogeneous hexahedral models*, suggesting that a more accurate boundary recovery may capture more accurately the strain gradients near the surface, which the both *hexahedral* models tend to fluctuate because of jagged surface. Therefore, it is concluded that at tissue level, *homogeneous tetrahedral model* is highly recommended in exploring cancellous bone's local strain prediction. Further work should perform on the validation of strain predicted by such models.

Keywords: MicroCT, microFE, mesh, cancellous bone, strain

6.1. Introduction

The most important functions of the skeleton (movement, protection, support) are all biomechanical in nature. Thus, it is not surprising that for a number of clinical scenarios the most important question to be answered is "will this bone fracture under this load"? If such question is limited to present time, it can be answered with excellent accuracy by only knowing the geometry of the bone, its mineral density distribution, and the precise direction and intensity of the forces being applied (Bouxsein et al., 2010; Kazakia et al., 2008). But if the question refers to a period of time, then in order to answer we also need to take into account how the mechanical properties of the bone might change during that time interval. Adult human bones change their mechanical properties over time only because of ageing, of a disease processes, or because of an intervention, whether pharmacological, or related to the life style (nutrition, exercise, smoking/drinking, etc.). Whatever is the cause, such changes take place at the tissue scale, where cellular populations remodel the mineralised extracellular matrix altering the tissue mechanical properties. Thus, it is of vital importance to be able to quantify the mechanical properties of bone tissue with a spatial resolution of 10-20 μm, a scale that better resolve the underneath bone microstructure (Bouxsein et al., 2010). Experimentally, this can only be done invasively (Atluri et al., 1983; Jansen et al., 2015; Zienkiewicz and Holister, 1965; Zienkiewicz et al.; Zienkiewicz et al., 1970), but using micro-computed tomography (MicroCT) imaging we can obtain non-invasive estimates of tissue behaviour under mechanical loading, by generating from the imaging data micro-finite element (MicroFE) models (Keyak et al., 1990; van Rietbergen, 2001; van Rietbergen et al., 1995). However, microFE models, as any other predictive model, need to pass a number of verification, validation, and uncertainty quantification tests (Anderson et al., 2007; Chen et al., 2014; Zauel et al., 2006) before they can be trusted and used for preclinical and clinical assessments.

In spite their popularity in biomechanics literature, there are relatively few published studies that document the verification and validation of such models. With respect to verification, we have defined the level of mesh refinement typically required to ensure asymptotic convergence over displacements and strains for various microFE modelling methods, both for linear and non-linear constitutive equations in Chapter3 (Chen et al., 2014). With respect to validation, Digital Volume Correlation (DVC) combined with in situ mechanical testing and microCT imaging can be used to measure the 3D full-field

displacement at a resolution of 10-20 μm as shown in Chapter4, but are not precise enough to provide an accurate measurement of strain at that spatial resolution (Dall'Ara et al., 2014). Therefore, so far microFE models have been validated exclusively with respect to their ability to predict such displacements (Zauel et al., 2006), in spite the fact that, for most applications, microFE models are primarily used to predict stresses and strains, not displacements.

Also, there are three broad families of modelling methods to generate microFE models of bone tissue, that rely on fairly different set of idealisations: the most commonly used microFE models assume the bone tissue to be homogeneous, segment bone from the background by using a threshold value in the attenuation coefficients, and use the Cartesian approximation of the boundary between bone tissue and marrow provided by the microCT images (Hollister et al., 1994; van Rietbergen et al., 1995; Verhulp et al., 2008). Other authors proposed alternative modelling methods that either model the bone tissue heterogeneity, but retain the Cartesian approximation to the boundary, independently from any threshold (Gross et al., 2012), or alternatively recover the smooth boundary through image segmentation, but retain the bone homogeneity assumption (Boyd and Muller, 2006; Leung et al., 2008; Muller and Ruegsegger, 1995; Ulrich et al., 1998). It is unclear how each of these idealisations affects the predictive accuracy.

Therefore, the aim of the present study is to compare three microFE modelling methods *(homogenous hexahedral model, heterogeneous hexahedral model and homogeneous tetrahedral model)* already verified and validated at least for the displacement, so as to explore the effect of the idealisations each method relies upon.

6.2. Materials and methods

6.2.1. MicroFE models and boundary conditions

Three different microFE models of Specimen3 verified for local convergence in Chapter3 and validated for displacement in Chapter4 were used in this study: HOMO-HEXA with voxel size of 19.84; HETE-HEXA with voxel size of 19.84; HOMO-TETRA with similar number of degrees of freedom (NDOF) as HOMO-HEXA (minimum edge length ~ 17 μm).

HOMO-HEXA

Two types of BCs were applied to HOMO-HEXA. In uniaxial displacement-based compression: the nodes at the lowermost layer were fully constrained, and a vertical displacement was applied to nodes at the uppermost layer of the model. A preliminary simulation was conducted to determine the displacement (0.02 mm) that allowed the maximum elemental third principal strain to reach 8000 με in order to stay in linear elastic regime. In uniaxial force-based compression, the nodes at the lowermost layer were fully constrained, and a vertical force was equally distributed to nodes at the uppermost layer of the model. The force was determined by calculating the reaction force (101 N) along the loading direction Z from the displacement-based compression. To improve readability, the displacement-based and force-based HOMO-HEXAs are referred to as D-HOMO-HEXA and F-HOMO-HEXA respectively.

HETE-HEXA

Two types of BCs were applied to HETE-HEXA, with the same uniaxial displacement and force as in HOMO-HEXA. To be specific, in uniaxial displacement-based compression: the nodes at the lowermost layer were fully constrained, and a vertical displacement (0.02 mm) was applied to nodes at the uppermost layer of the model. In uniaxial force-based compression, the nodes at the lowermost layer were fully constrained, and a vertical force (101 N) was equally distributed to only bone nodes at the uppermost layer of the model. The displacement-based and force-based HETE-HEXAs are referred to as D-HETE-HEXA and F-HETE-HEXA respectively.

HOMO-TETRA

Only the displacement-based BC was applied to the model, with the same uniaxial displacement as in HOMO-HEXA. In particular, the nodes at the lowermost layer were fully constrained, and a vertical displacement (0.02 mm) was applied to nodes at the uppermost layer of the model. The displacement-based HOMO-TETRA is referred to as D-HOMO-TETRA thereafter.

6.2.2. Model comparison

Since no experimental measurement with sufficient accuracy and spatial resolution is available, strictly speaking no validation is possible. However, we know that each model relies on a different set of idealizations/simplifications: HOMO-TETRA models

the boundary as smooth, whereas all HETE-HEXA and HOMO-HEXA models simplify it with a Cartesian approximation (jagged boundary). Similarly, HETE-HEXA models the gradients of mechanical properties of the tissue due to different mineralisation using a linear approximation, whereas HOMO-HEXA models simplify it assuming such properties are constant. Thus, knowing that the three modelling methods under evaluation produce comparable displacement field, we can compare their strain fields two by two, in order to explore the effect of specific idealisations on the prediction of strains. HOMO-HEXA and HETE-HEXA different only the idealisation of how the tissue elastic properties are mapped; HOMO-HEXA and HOMO-TETRA different only for how the boundary is idealised; HETE-HEXA and HOMO-TETRA differ for both aspects, and can inform whether the heterogeneous mapping of the elastic properties can mitigate the effects of less accurate boundary recovery in hexahedral model, where compared to tetrahedral model.

To avoid boundary effects, the extreme top and bottom region of 10% the length of the model were excluded. The remaining region of 80% was evenly divided into three sections, which were sub-divided into four equally shaped quadrants. The models were divided into twelve regions of interest (ROI) this way (Fig. 6.1). Using the D-HOMO-HEXA model as reference, we selected the ROI with the highest stress error (Zienkiewicz and Zhu, 1987), and restricted the comparison to this region, assumed to be the most critical region of the model in term of strain gradients (Pointer, 2004). All comparisons between the models were limited to this ROI.
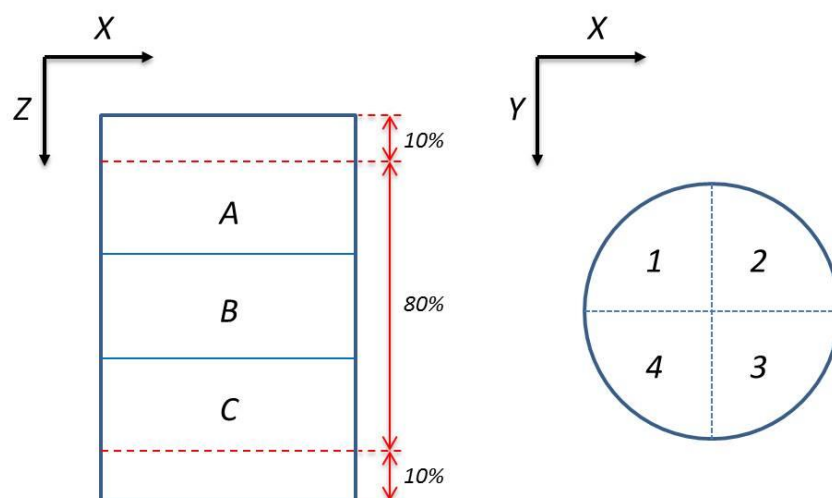
Fig.6.1. *ROI partition of the specimen*

HOMO-HEXA vs. HETE-HEXA

The bone elements contained in the chosen ROI from HOMO-HEXA and HETE-HEXA sharing the same spatial location were selected and their outputs were compared. In particular, for each loading condition (D-HOMO-HEXA vs. D-HETE-HEXA and F-HOMO-HEXA vs. F-HETE-HEXA), the nodal displacements and elemental centroid normal strains and normal stresses in X, Y (transverse direction) and Z (loading direction) between two models were compared.

HOMO-TETRA vs. HOMO-HEXA

The surface nodes of HOMO-TETRA from the ROI was selected and mapped into HOMO-HEXA. The surface nodal displacements, normal strains and normal stresses in X, Y (transverse direction) and Z (loading direction) from D-HOMO-TETRA was compared with interpolated results from the same spatial location in D-HOMO-HEXA using trilinear interpolation.

HOMO-TETRA vs. HETE-HEXA

The surface nodes of HOMO-TETRA from the ROI was selected and mapped into bone elements in HETE-HEXA. To reduce the computational time, only the normal strain in Z (loading direction) from D-HOMO-TETRA was compared with interpolated results from the same spatial location in D-HETE-HEXA using trilinear interpolation.

6.2.3. Statistics

Each comparison was performed using linear regression, where the slope and intercept of the equation as well as coefficient of determination (R^2) were reported. As there is no strain validation for the models, and each microFE models the bone tissue based on its simplification, any distinction seen between the models were treated as the difference. For each comparison the Root Mean Square Difference (RMSD), the RMSD divided by the absolute maximum value from the reference model (RMSD%), the largest difference between two models (Max. diff), the Max. diff divided by absolute maximum value from the reference model (Max. diff%) were computed.

6.3. Results

Preliminary test shows that the A3 (Fig.6.1) from D-HOMO-HEXA has the highest stress error and the comparisons between models were limited to this region. Results from all comparisons are reported in Fig.6.2-7.

HOMO-HEXA vs. HETE-HEXA

In displacement-based loading condition, the D-HETE-HEXA overall predicted lower displacement than the D-HOMO-HEXA by 15% along X (slope equal to 0.85, R^2 equal to 0.99, RMSD% equal to 7.26%), 17% along Y (slope equal to 0.83, R^2 equal to 0.96, RMSD% equal to 14.29%) and 7% along Z (slope equal to 0.93, R^2 equal to 0.99, RMSD% equal to 1.90%) (Fig.6.2, left). Similarly, the D-HETE-HEXA predicted lower strain than D-HOMO-HEXA model by 11% in X (slope equal to 0.89, R^2 equal to 0.92, RMSD% equal to 2.16%), 11% in Y (slope equal to 0.89, R^2 equal to 0.91, RMSD% equal to 3.05%) and 3% in Z (slope equal to 0.97, R^2 equal to 0.94, RMSD% equal to 2.45%) (Fig.6.3, left). The stress the two models predicted also has similar trend with D-HETE-HEXA predicting lower value than D-HOMO-HEXA model by 15% in X (slope equal to 0.85, R^2 equal to 0.91, RMSD% equal to 2.91%) and Y (slope equal to 0.85, R^2 equal to 0.90, RMSD% equal to 3.14% in Y) and 5% in Z (slope equal to 0.95, R^2 equal to 0.92, RMSD% equal to 3.72%) (Fig.6.4, left).

Similar trends but larger differences were found in comparisons between the two hexahedral models under force-based loading condition. To be specific, the F-HETE-HEXA predicted lower displacements than F-HOMO-HEXA by 31% in X (slope equal to 0.69, R^2 equal to 0.91, RMSD% equal to 17.03%), 41% in Y (slope equal to 0596, R^2 equal to 0.93, RMSD% equal to 22.68%) and 30% in Z (slope equal to 0.70, R^2 equal to 0.94, RMSD% equal to 20.74%) (Fig.6.2, right). The F-HETE-HEXA predicts lower strain than F-HOMO-HEXA by 33% in X (slope equal to 0.67, R^2 equal to 0.92, RMSD% equal to 4.09%), 34% in Y (slope equal to 0.66, R^2 equal to 0.89, RMSD% equal to 4.13%) and 27% in Z (slope equal to 0.73, R^2 equal to 0.93, RMSD% equal to 4.18%) (Fig.6.3, right). Stress predicted from two models has similar trend with F-HETE-HEXA predicting lower value than F-HOMO-HEXA by 36% in X (lope equal to 0.64, R^2 equal to 0.90, RMSD% equal to 5.64%), 37% in Y (slope equal to 0.63, R^2 equal to 0.88, RMSD% equal to 6.67%) and 29% in Z (slope equal to 0.71, R^2 equal to 0.91, RMSD% equal to 5.74%) (Fig.6.4, right).

From the scatter plots it is seen for both boundary conditions there are certain nodes (less than 0.3%) in two hexahedral models showing different displacement behaviour (reflected by scatter plots of displacements showing weird spikes in Fig.6.2). It is also noticed that there are certain elements having very low strain and stress intensity (close to zero) in HOMO-HEXA but deformed to a certain degree in HETE-HEXA (reflected by vertical lines of points in the Fig.6.3-4).

HOMO-TETRA vs. HOMO-HEXA

D-HOMO-TETRA overall predicted similar displacements as D-HOMO-HEXA, especially along the loading direction Z (slope equal to 1, R^2 equal to 0.99, RMSD% equal to 0.83%) (Fig.6.5, left). The D-HOMO-TETRA in general predicted higher strain than D-HOMO-HEXA model by 9% in X (slope equal to 1.09, R^2 equal to 0.71, RMSD% equal to 4.88%), 9% in Y (slope equal to 1.09, R^2 equal to 0.69, RMSD% equal to 7.19%) and 23% in Z (slope equal to 1.23, R^2 equal to 0.79, RMSD% equal to 5.59%) (Fig.6.5, middle). The stress the two models predicted also has similar trend with D-HOMO-TETRA predicting higher value than D-HOMO-HEXA model by 20% in X (slope equal to 1.20, R^2 equal to 0.77, RMSD% equal to 4.33%) and 22% in Y (slope equal to 1.22, R^2 equal to 0.74, RMSD% equal to 6.49% in Y) and 29% in Z (slope equal to 1.29, R^2 equal to 0.83, RMSD% equal to 5.27%) (Fig.6.5, right).

It was also noticed that the RMSD of both strain and stress increased with strain or stress intensity. Especially in Z direction, the D-HOMO-TETRA and D-HOMO-HEXA tended to predict comparable strain at low strain intensity (below -4000 με), and differ largely at high strain field (beyond -4000 με) (Fig.6.6. left). Therefore, we restricted the analysis to high strain field in loading direction Z. In particular, surface nodal strain higher than -4000 με predicted by D-HOMO-TETRA were selected and compared with strain interpolated from the D-HOMO-HEXA at the same spatial location. To make it comparable, the intercept of the linear regression at higher strain field was forced to be -59 με (the same as when investigating the overall strain range). It showed that at higher strain, the D-HOMO-TETRA predicted 49% higher strain than D-HOMO-HEXA and poor correlation between two models were found (slope equal to 1.49, R^2 equal to 0.12, RMSD% equal to 24.30%) (Fig.6.7, left).

HOMO-TETRA vs. HETE-HEXA

The D-HOMO-TETRA in general predicted higher strain than D-HETE-HEXA model by 11% in Z (slope equal to 1.11, R^2 equal to 0.73, RMSD% equal to 5.72%) (Fig.6.6, right). Similarly, in Z direction, the D-HOMO-TETRA and D-HETE-HEXA tended to predict comparable strain at low strain intensity (below -4000 με), and differ largely at high strain field (beyond -4000 με). By comparing only the higher strain field (higher than -4000 με predicted by D-HOMO-TETRA) in two models and forcing the intercept of the regression to be 122 με (the same as when investigating the overall strain range), the D-HOMO-TETRA predicted 45% higher strain than D-HETE-HEXA and poor correlation between two models were found (slope equal to 1.45, R^2 equal to 0.05, RMSD% equal to 22.32%) (Fig.6.7, right). It was also noticed that there are certain nodes having very low strain intensity (close to zero) in D-HOMO-TETRA but deformed to a certain degree in D-HETE-HEXA (reflected by horizontal lines of points in Fig.6.6 right).
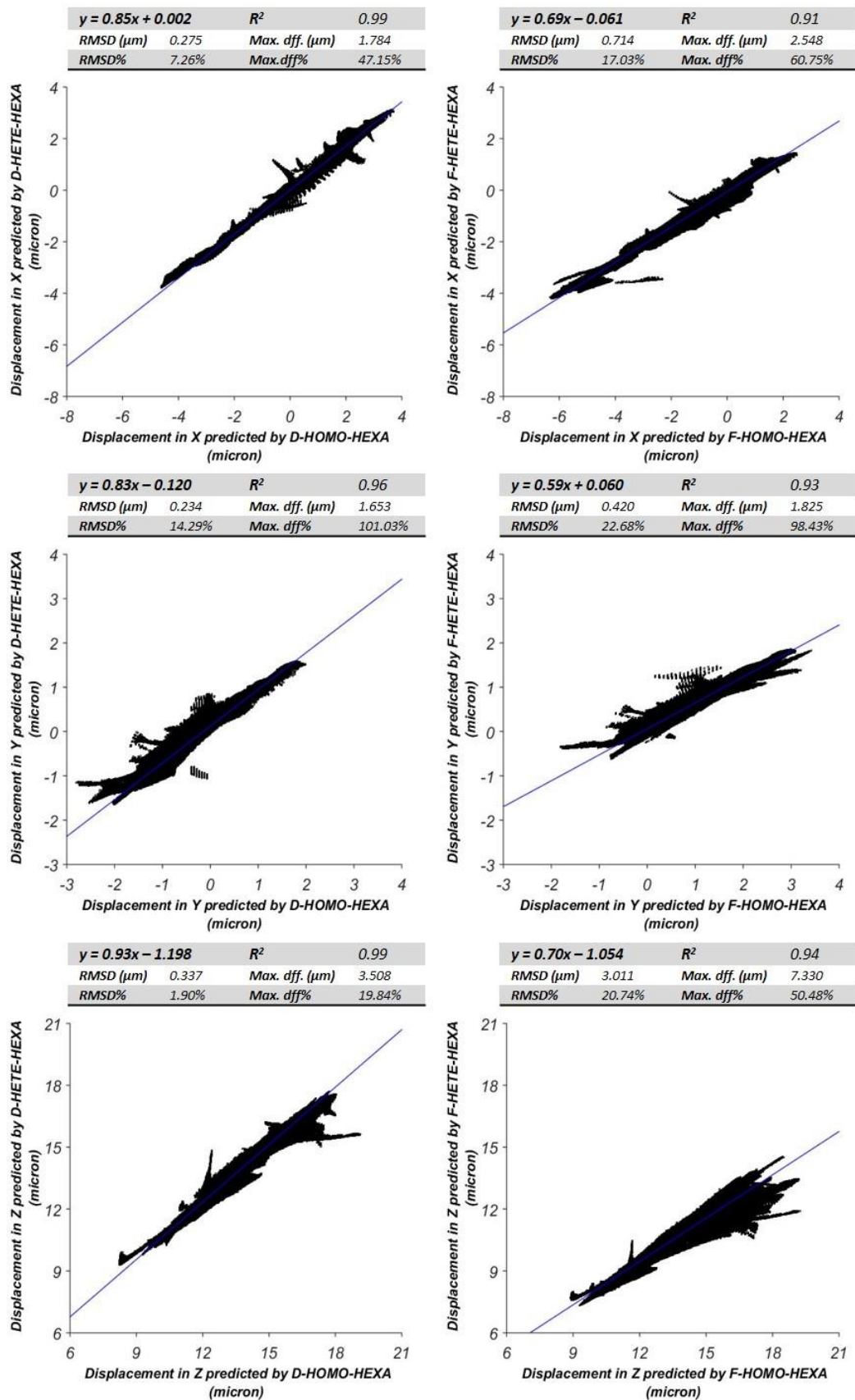
Fig.6.2. *Displacement comparison between HOMO_HEXA and HETE_HEXA using displacement-based BC (left) and force-based BC (right)*

$y = 0.89x + 19$		R^2	0.92
RMSD (με)	107	*Max. dff. (με)*	1959
RMSD%	2.16%	*Max. dff%*	39.77%

$y = 0.67x + 13$		R^2	0.91
RMSD (με)	157	*Max. dff. (με)*	2934
RMSD%	4.09%	*Max. dff%*	76.28%

$y = 0.89x + 39$		R^2	0.91
RMSD (με)	95	*Max. dff. (με)*	1571
RMSD%	3.05%	*Max. dff%*	50.49%

$y = 0.66x + 37$		R^2	0.89
RMSD (με)	132	*Max. dff. (με)*	2455
RMSD%	4.13%	*Max. dff%*	76.69%

$y = 0.97x - 79$		R^2	0.94
RMSD (με)	174	*Max. dff. (με)*	5369
RMSD%	2.45%	*Max. dff%*	75.87%

$y = 0.73x - 64$		R^2	0.93
RMSD (με)	222	*Max. dff. (με)*	4757
RMSD%	4.18%	*Max. dff%*	89.48%

Fig.6.3. *Strain comparison between HOMO_HEXA and HETE_HEXA using displacement-based BC (left) and force-based BC (right)*

$y = 0.85x - 0.43$		R^2	0.91
RMSD(MPa)	2.09	Max. dff. (MPa)	43.76
RMSD%	2.91%	Max. dff%	60.70%

$y = 0.64x - 0.32$		R^2	0.90
RMSD(MPa)	2.97	Max. dff. (MPa)	64.99
RMSD%	5.64%	Max. dff%	123.25%

$y = 0.85x - 0.13$	R^2	0.90
RMSD(MPa)	1.81	Max. dff. (MPa)	31.59
RMSD%	3.14%	Max. dff%	54.75%

$y = 0.63x - 0.01$	R^2	0.88
RMSD(MPa)	2.57	Max. dff. (MPa)	58.32
RMSD%	6.67%	Max. dff%	151.64%

$y = 0.95x - 1.75$	R^2	0.92
RMSD(MPa)	3.72	Max. dff. (MPa)	103.86
RMSD%	3.36%	Max. dff%	93.72%

$y = 0.71x - 1.38$	R^2	0.91
RMSD(MPa)	4.38	Max. dff. (MPa)	117.69
RMSD%	5.74%	Max. dff%	154.34%

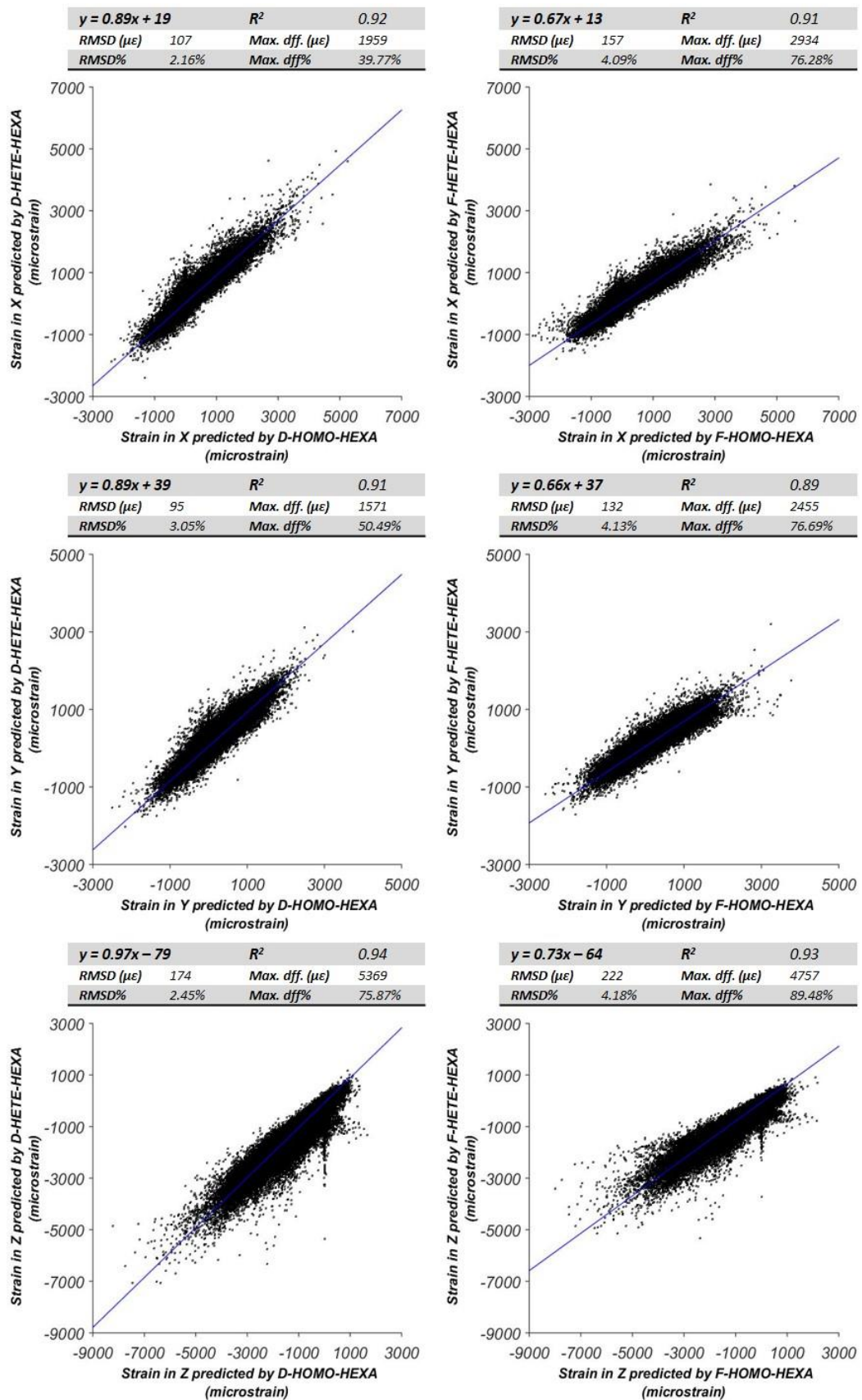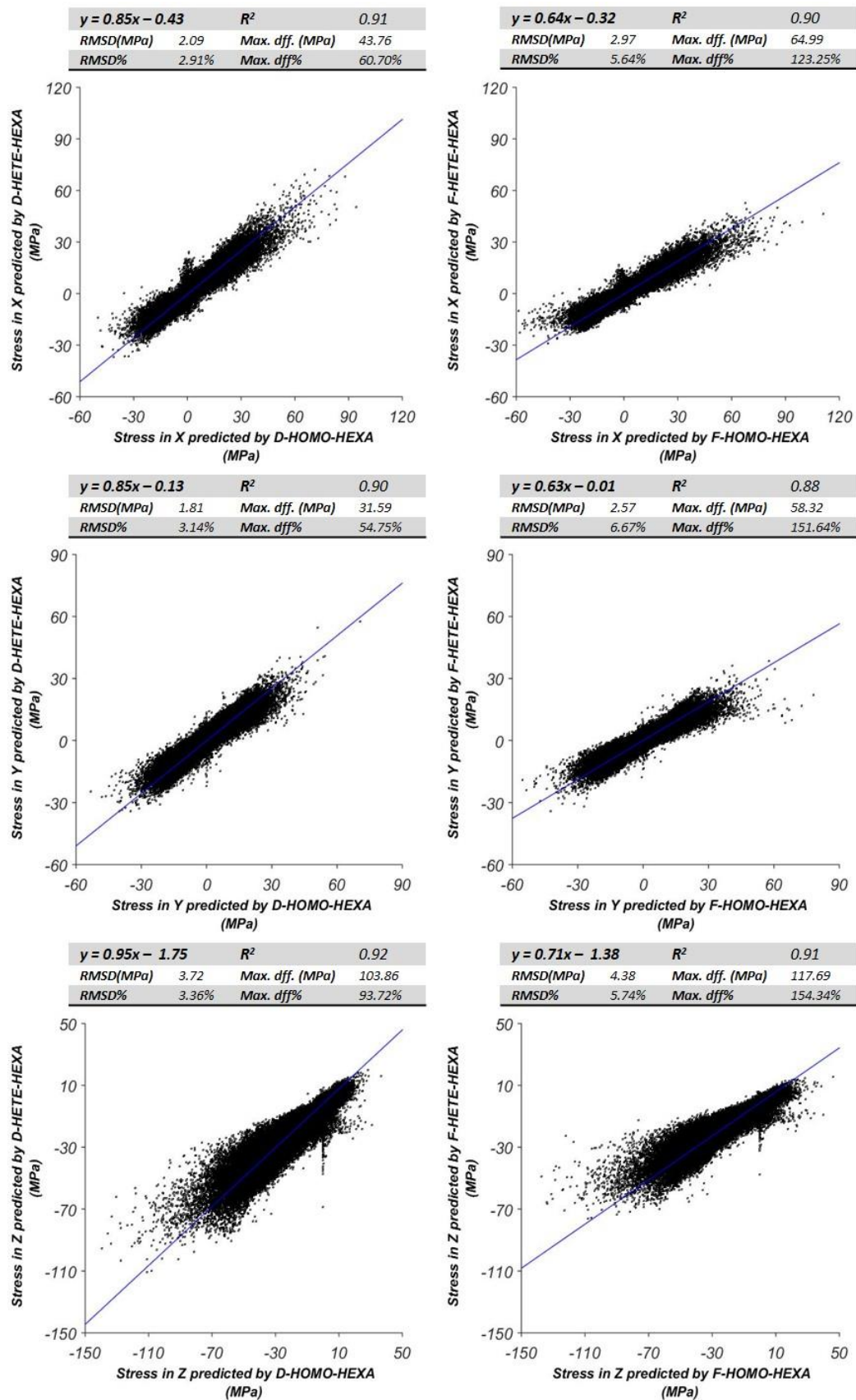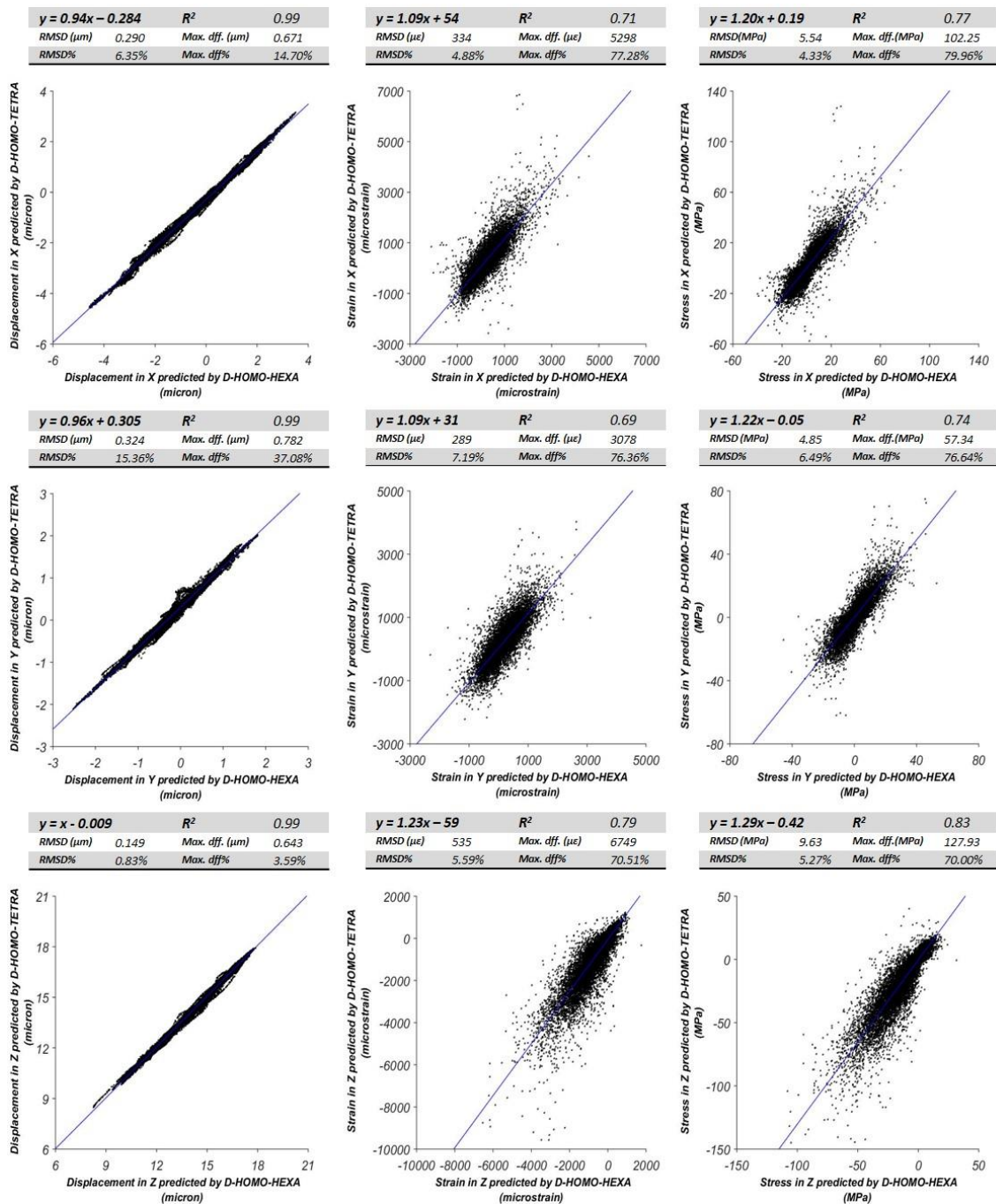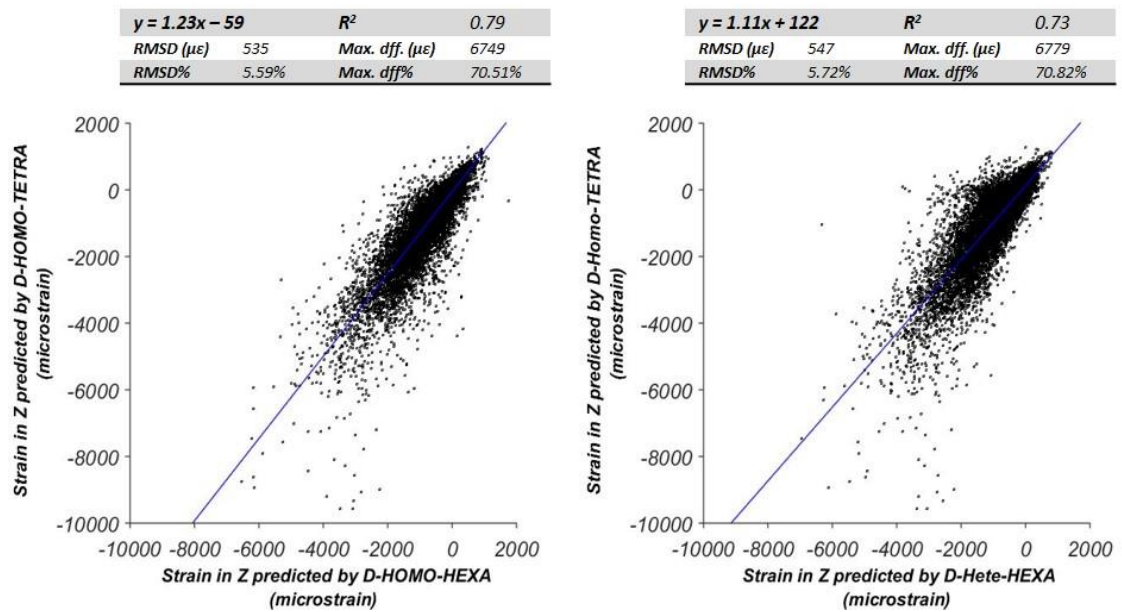**Fig.6.4.** *Stress comparison between HOMO_HEXA and HETE_HEXA using displacement-based BC (left) and force-based BC (right)*

$y = 0.94x - 0.284$		R^2		0.99
RMSD (µm)	0.290	Max. diff. (µm)		0.671
RMSD%	6.35%	Max. diff%		14.70%

$y = 1.09x + 54$		R^2		0.71
RMSD (µε)	334	Max. diff. (µε)		5298
RMSD%	4.88%	Max. diff%		77.28%

$y = 1.20x + 0.19$		R^2		0.77
RMSD(MPa)	5.54	Max. diff.(MPa)		102.25
RMSD%	4.33%	Max. diff%		79.96%

$y = 0.96x + 0.305$		R^2		0.99
RMSD (µm)	0.324	Max. diff. (µm)		0.782
RMSD%	15.36%	Max. diff%		37.08%

$y = 1.09x + 31$		R^2		0.69
RMSD (µε)	289	Max. diff. (µε)		3078
RMSD%	7.19%	Max. diff%		76.36%

$y = 1.22x - 0.05$		R^2		0.74
RMSD(MPa)	4.85	Max. diff.(MPa)		57.34
RMSD%	6.49%	Max. diff%		76.64%

$y = x - 0.009$		R^2		0.99
RMSD (µm)	0.149	Max. diff. (µm)		0.643
RMSD%	0.83%	Max. diff%		3.59%

$y = 1.23x - 59$		R^2		0.79
RMSD (µε)	535	Max. diff. (µε)		6749
RMSD%	5.59%	Max. diff%		70.51%

$y = 1.29x - 0.42$		R^2		0.83
RMSD (MPa)	9.63	Max. diff.(MPa)		127.93
RMSD%	5.27%	Max. diff%		70.00%

Fig.6.5. *Comparison between D_HOMO_TETRA and D_HOMO_HEXA in terms of displacement (left), strain (middle) and stress (right); top line results for X, middle Y, bottom line Z direction*

112

y = 1.23x − 59		R²		0.79
RMSD (µε)	535	Max. dff. (µε)	6749	
RMSD%	5.59%	Max. dff%	70.51%	

y = 1.11x + 122		R²		0.73
RMSD (µε)	547	Max. dff. (µε)	6779	
RMSD%	5.72%	Max. dff%	70.82%	

Fig.6.6. *Comparison between D_HOMO_TETRA and D_HOMO_HEXA (left) and between D_HOMO_TETRA and D_HETE_HEXA (right) in terms of strain in the loading direction (Z)*

y = 1.49x − 59		R²		0.12
RMSD (µε)	2326	Max. dff. (µε)	6749	
RMSD%	24.30%	Max. dff%	70.51%	

y = 1.45x + 122		R²		0.05
RMSD (µε)	2137	Max. dff. (µε)	6779	
RMSD%	22.32%	Max. dff%	70.82%	
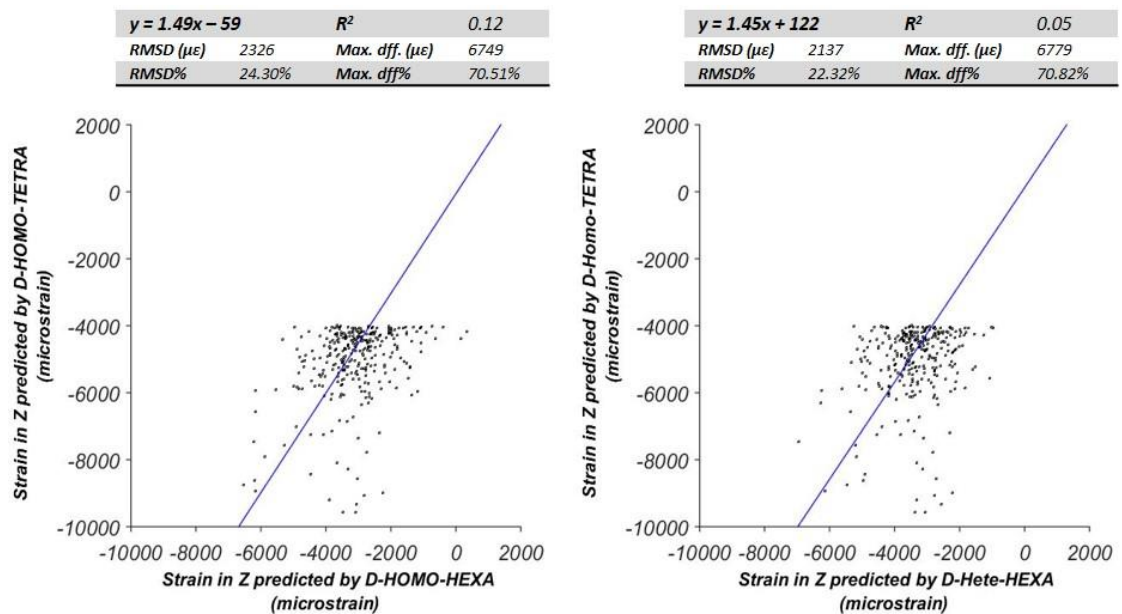
Fig.6.7. *Comparison between D_HOMO_TETRA and D_HOMO_HEXA (left) and between D_HOMO_TETRA and D_HETE_HEXA (right) in terms of high strain in the loading direction (Z)*

6.4. Discussion

The aim of the present study was to compare stress and strain field predicted by microFE models using different mesh generation schemes. The HETE-HEXA, by capturing mineralisation gradients due to remodelling process, was assumed to predict more accurately the results than the HOMO-HEXA. The HOMO-TETRA, by recovering the boundary smoothly, was assumed to predict better the results than the HOMO-HEXA, especially at the trabecular surface.

When the predictions of the two hexahedral models loaded with the displacement-based BC were compared, the D-HETE-HEXA predicted lower displacement (7% - 17%), strain (3% - 11%) and stress (5% - 15%), this is probably due to the lower stiffness of HETE-HEXA. This is confirmed by the lower reaction force of HETE-HEXA (~89N) compared to HOMO-HEXA (~101N). In the force-based compression, the differences between two models were larger with the F-HETE-HEXA predicts even lower displacement (30% - 41%), strain (27% -33%) and stress (29% - 37%). This is probably due to the fact that in displacement-based loading condition, the models were over-constrained and the stiffness of model played less important role. However, in force-based loading condition, the model would deform naturally according to the force transmitted to each point (as opposed to displacement-based loading condition, where the model are forced to deform to a certain degrees as BC imposed). Therefore the stiffness plays a larger role and larger differences in local mechanical properties are seen.

In both loading conditions, the two models predicted different displacements at certain locations (Fig.6.2). Because of different material properties used, two models might exhibit different level of anisotropy and connectivity, resulting in difference in displacement of transverse direction of a couple of micros. During compression, a single trabecula in the HOMO-HEXA that lacks of connectivity (Fig.6.8) is more likely to perform a rigid body motion (Fig.6.9, left). However, the same trabecula in HETE-HEXA would be compressed by having connectivity to other trabeculae through transition elements (partially mineralised bone tissue existed at the trabecular surface) (Fig.6.9, right). It is also found that the RMSD increases with the stress intensity (reflected by the butterfly or cone shape of the stress scatter plot in Fig.6.4). This is probably due to the different material properties in two models. In particular, while the

module of elasticity in HOMO-HEXA is constant (17 GPa) throughout the elements, it spans a certain range in HETE-HEXA (~10-25 GPa). Therefore, when having comparable strains, the HETE-HEXA would predict stresses spanned in a larger range, especially for elements having higher strain intensity. In addition, there are certain elements having nearly null strain and stress intensity in HOMO-HEXA but valued in a certain range in HETE-HEXA (Fig.6.3-4). Again, these elements behaved differently because of different element connectivity of local regions in two models (Fig.6.10). Single trabecula lacking of support in HOMO-HEXA performed a rotation while connectivity between trabeculae guaranteed the deformation in HETE-HEXA.

The D-HOMO-TETRA predicted overall similar displacement (0% - 6%), higher strain (9% to 23%) and stress (20% - 29%) compared to D-HOMO-HEXA. This suggests that a more accurate boundary recovery model may capture more accurately the strain gradients near the surface, which the D-HOMO-HEXA tends to reduce, especially at high strain field. This was reflected by the strain distribution plot in the direction of load, Z (Fig.6.11). The D-HOMO-TETRA predicted similarly at low strain field as D-HOMO-HEXA but quite differently at high strain field (highlighted by red circle). The recovered boundary of D-HOMO-TETRA tended to result in a smoothed and continuous strain gradient whereas the jagged surfaces of D-HOMO-HEXA causes the strain to fluctuate leading to unstable strain concentrators in a few corner nodes, which explains the very poor correlation of high strain field between two models.

The D-HETE-HEXA behaved similarly to D-HOMO-HEXA when compared to D-HOMO-TETRA. In particular, D-HOMO-TETRA and D-HETE-HEXA strain predictions were in good agreement for low strain values, but differed largely in region with high strain (highlighted by red circle) (Fig.6.11). The results suggest that the heterogeneous mapping of the elastic properties in D-HETE-HEXA does not mitigate the effects of less accurate boundary recovery. In addition, there are certain surface nodes having nearly null strain in D-HOMO-TETRA but resulting in a certain range in D-HETE-HEXA (Fig.6.6, right). It is seen from the contour plot (Fig.6.12) these points behaved differently because of different element connectivity of local regions in two models. Lacking of support, some trabeculae (highlighted by red circle) in D-HOMO-TETRA performed a rigid body motion while connectivity through transition elements led to deformation in D-HETE-HEXA.

From the above mentioned comparisons, it results that three different tissue modelling techniques tend to predict similar displacement overall (refer to the validation study in Chapter 4). However, differences in mechanical properties exist locally between two hexahedral models, due to different conditions of element connectivity. In particular, HETE-HEXA is able to catch the local mineralization distribution, as well as the connectivity through partially mineralized tissue which is not modelled in homogeneous models. Seeing under displacement-based loading condition, two hexahedral models produced quite similar strains along loading direction and also the higher computational cost of HETE-HEXA, with voxel sizes of 10-20 μm the advantage over traditional less computationally expensive HOMO-HEXA seems minimal. However, considering the ability of HETE-HEXA of catching local mineralization distribution and possibly mitigating the partial volume effect, their usefulness may increase if applied to lower resolution images as clinical CT scans performed at larger voxel size (e.g. high-resolution peripheral quantitative computed tomography (HRpQCT) at a typical voxel size of 82 μm (Christen et al., 2013)). HOMO-TETRA tends to predict higher strains at high strain field than both HOMO-HEXA and HETE-HEXA, suggesting that a more accurate boundary recovery may capture more accurately and smoothly the strain gradients near the surface, which the both hexahedral models tend to fluctuate due to jagged surface. Thus HOMO-TETRA maybe superior, especially if the purpose is to investigate the bone failure mechanism based on certain strain criteria (Pistoia et al., 2002; Schileo et al., 2008). Therefore, we concluded amongst different tissue modelling techniques, HOMO-TETRA is highly recommended, in spite of the higher difficulty in generating them, especially for low volume fraction specimens. Further investigation on its strain prediction need to be done when there is a proper validation method to measure the strain at the scale of tens of microns.
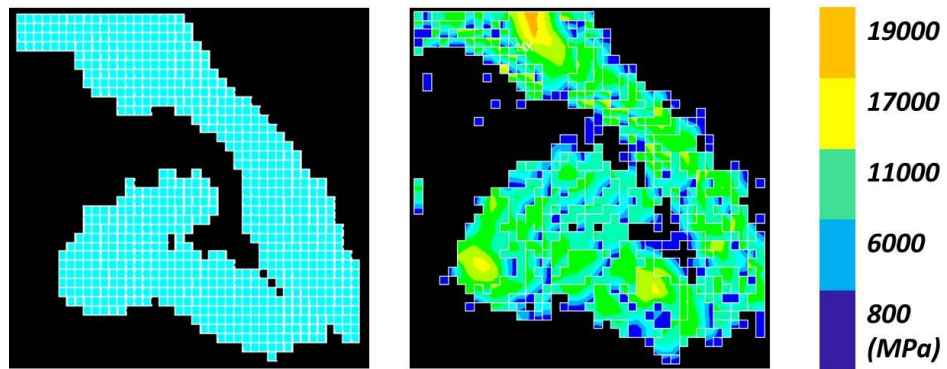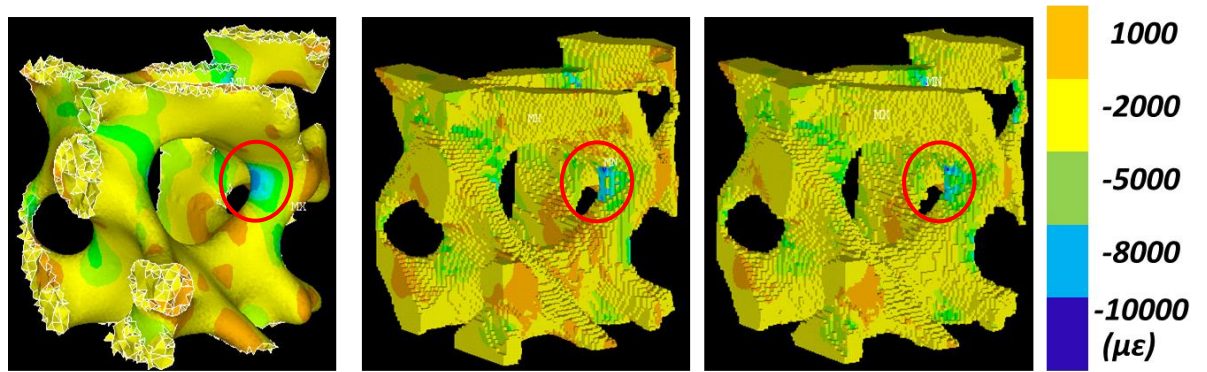
Fig.6.8. *Element modulus distribution of a single trabecula in HOMO_HEXA (left) and HETE_HEXA (right). In HETE_HEXA, both bone elements and transition elements are plotted. It is seen that by having transition elements wrapping out of bone elements, HETE_HEXA has more connectivity than HOMO-HEXA.*
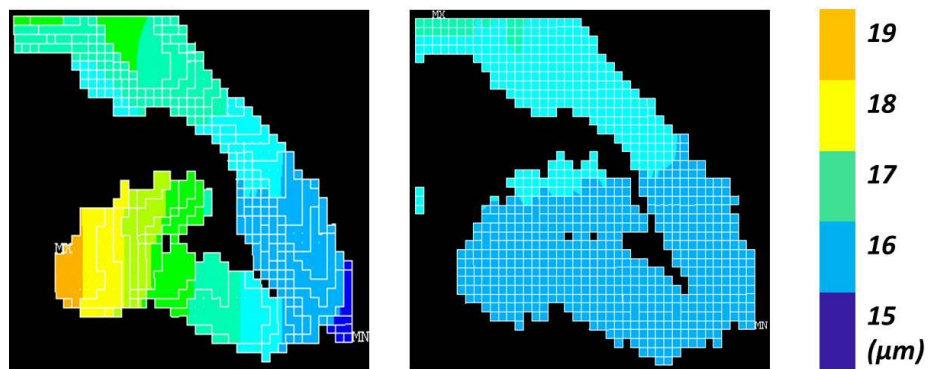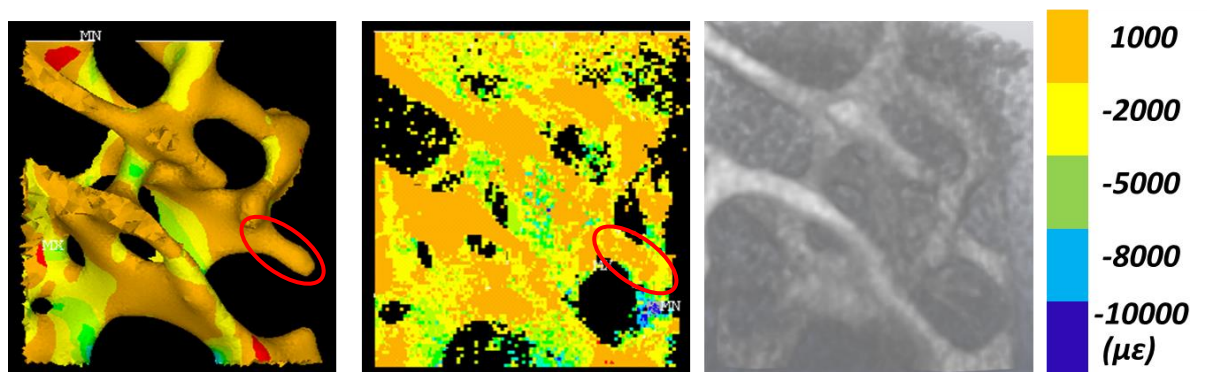

Fig.6.9. *Displacement distribution (loading direction Z) of a single trabecula in HOMO_HEXA (left) and HETE_HEXA (right). Only bone elements are plotted.*
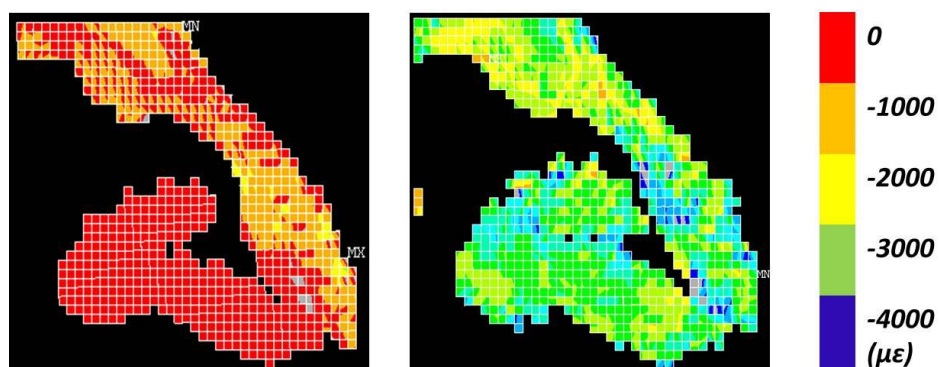
Fig.6.10. *Strain distribution (loading direction Z) of a single trabecula in HOMO_HEXA (left) and HETE_HEXA (right). Only bone elements are plotted.*

Fig.6.11. *Strain distribution (loading direction Z) of a few trabeculae in D_HOMO_TETRA (left), D_HOMO_HEXA (middle) and D_HETE_HEXA (right).*

Fig.6.12. *Strain distribution (loading direction Z) of a few trabeculae in D_HOMO_TETRA (left), D_HETE_HEXA (middle) and 3D representation of images (right). In D_HETE_HEXA, both bone elements and transition elements are plotted. It is seen that by having transition elements D_HETE_HEXA catches the partially mineralized bone tissue that was not modelled in D_HOMO_TETRA. Correspondingly, during compression the single trabecula highlighted by red circle in D_HOMO_TETRA performed a rigid body motion, resulting in nearly null strain whereas in D_HETE_HEXA, by having extra support through transition elements, it deformed to some extent*

6.5. References

Anderson, A.E., Ellis, B.J., Weiss, J.A., 2007. Verification, validation and sensitivity studies in computational biomechanics. Computer methods in biomechanics and biomedical engineering 10, 171-184.

Atluri, S.N., Gallagher, R.H., Zienkiewicz, O.C., Pian, T.H.H., 1983. Hybrid and mixed finite element methods. Wiley, Chichester ; New York.

Bouxsein, M.L., Boyd, S.K., Christiansen, B.A., Guldberg, R.E., Jepsen, K.J., Muller, R., 2010. Guidelines for assessment of bone microstructure in rodents using micro-computed tomography. J. Bone Miner. Res. 25, 1468-1486.

Boyd, S.K., Muller, R., 2006. Smooth surface meshing for automated finite element model generation from 3D image data. J. Biomech. 39, 1287-1295.

Chen, Y., Pani, M., Taddei, F., Mazza, C., Li, X., Viceconti, M., 2014. Large-scale finite element analysis of human cancellous bone tissue micro computer tomography data: a convergence study. J. Biomech. Eng. 136.

Christen, D., Melton, L.J., 3rd, Zwahlen, A., Amin, S., Khosla, S., Muller, R., 2013. Improved fracture risk assessment based on nonlinear micro-finite element simulations from HRpQCT images at the distal radius. J. Bone Miner. Res. 28, 2601-2608.

Dall'Ara, E., Barber, D., Viceconti, M., 2014. About the inevitable compromise between spatial resolution and accuracy of strain measurement for bone tissue: a 3D zero-strain study. J. Biomech. 47, 2956-2963.

Gross, T., Pahr, D.H., Peyrin, F., Zysset, P.K., 2012. Mineral heterogeneity has a minor influence on the apparent elastic properties of human cancellous bone: a SRmuCT-based finite element study. Computer methods in biomechanics and biomedical engineering 15, 1137-1144.

Hollister, S.J., Brennan, J.M., Kikuchi, N., 1994. A homogenization sampling procedure for calculating trabecular bone effective stiffness and tissue level stress. J. Biomech. 27, 433-444.

Jansen, L.E., Birch, N.P., Schiffman, J.D., Crosby, A.J., Peyton, S.R., 2015. Mechanics of intact bone marrow. Journal of the mechanical behavior of biomedical materials 50, 299-307.

Kazakia, G.J., Burghardt, A.J., Cheung, S., Majumdar, S., 2008. Assessment of bone tissue mineralization by conventional x-ray microcomputed tomography: comparison with synchrotron radiation microcomputed tomography and ash measurements. Med. Phys. 35, 3170-3179.

Keyak, J.H., Meagher, J.M., Skinner, H.B., Mote, C.D., Jr., 1990. Automated three-dimensional finite element modelling of bone: a new method. J. Biomed. Eng. 12, 389-397.

Leung, S.Y., Browne, M., New, A.M., 2008. Smooth surface micro finite element modelling of a cancellous bone analogue material. Proc. Inst. Mech. Eng. H 222, 145-149.

Muller, R., Ruegsegger, P., 1995. Three-dimensional finite element modelling of non-invasively assessed trabecular bone structures. Med. Eng. Phys. 17, 126-133.

Pistoia, W., van Rietbergen, B., Lochmuller, E.M., Lill, C.A., Eckstein, F., Ruegsegger, P., 2002. Estimation of distal radius failure load with micro-finite element analysis models based on three-dimensional peripheral quantitative computed tomography images. Bone 30, 842-848.

Pointer, J., 2004. Understanding Accuracy and Discretization Error in an FEA Model. ANSYS 7.1, 2004 Conference.

Schileo, E., Taddei, F., Cristofolini, L., Viceconti, M., 2008. Subject-specific finite element models implementing a maximum principal strain criterion are able to estimate failure risk and fracture location on human femurs tested in vitro. J. Biomech. 41, 356-367.

Ulrich, D., van Rietbergen, B., Weinans, H., Ruegsegger, P., 1998. Finite element analysis of trabecular bone structure: a comparison of image-based meshing techniques. J. Biomech. 31, 1187-1192.

van Rietbergen, B., 2001. Micro-FE analyses of bone: state of the art. Adv. Exp. Med. Biol. 496, 21-30.

van Rietbergen, B., Weinans, H., Huiskes, R., Odgaard, A., 1995. A new method to determine trabecular bone elastic properties and loading using micromechanical finite-element models. J. Biomech. 28, 69-81.

Verhulp, E., van Rietbergen, B., Muller, R., Huiskes, R., 2008. Indirect determination of trabecular bone effective tissue failure properties using micro-finite element simulations. J. Biomech. 41, 1479-1485.

Zauel, R., Yeni, Y.N., Bay, B.K., Dong, X.N., Fyhrie, D.P., 2006. Comparison of the linear finite element prediction of deformation and strain of human cancellous bone to 3D digital volume correlation measurements. J. Biomech. Eng. 128, 1-6.

Zienkiewicz, O.C., Holister, G.S., 1965. Stress analysis; recent developments in numerical and experimental methods. J. Wiley, London, New York,.

Zienkiewicz, O.C., Taylor, R.L., Nithiarasu, P., The finite element method for fluid dynamics, Seventh edition. ed.

Zienkiewicz, O.C., Valliappan, S., Ergatoudis, J., 1970. Finite element analysis in rock mechanics, a general review. Construction Industry Research and Information Association, London,.

Zienkiewicz, O.C., Zhu, J.Z., 1987. A simple error estimator and adaptive procedure for practical engineerng analysis International Journal for Numerical Methods in Engineering Volume 24, Issue 2, Int J Numer Meth Eng, pp. 337-357.

Chapter7

Conclusions

7.1. Research questions

The mechanical behaviour of bone under stress is of great scientific and clinical importance. From a fundamental scientific perspective, as the primary function of the skeleton is mechanical in nature a lot of related biological and physiological mechanisms are mechano-regulated; in all this research it is essential to know with the best possible accuracy the displacements, stresses, and strains induced by given loads in the bone tissue.

From the clinical point of view the mechanical behaviour of bone is important in relation to fragility fractures induced by osteoporosis, other dismetabolisms, and congenital bone diseases such as osteogenesis imperfecta; in mechano-related degenerative diseases such as osteoarthritis; in the identification of abuse-related fractures in children; in the risk of bone fracture due to metastatic lesions; and in neurological conditions such as Charcot's joint. A good example is osteoporosis.

Osteoporosis is a systemic skeletal disease characterized by a reduction of bone mass and deterioration of bone microstructure (Borah et al., 2001; Kanis and Johnell, 2005; Kim et al., 2009; Sedlak et al., 2007). It causes bones to become weak and fragile, and therefore more sensitive to fracture from falling or overloading. It is a large and growing concern for public health, and has drawn a lot of attentions on the research and treatment of the disease. In traditional clinical practice, bone fracture risk is assessed using dual-energy X-ray absorptiometry (DXA) by evaluating the bone quality based on its density (Brask-Lindemann et al., 2011; Salehi-Abari, 2015). However, the skeletal competence is not only determined by the bone mineral density, but also by its microstructure (Ulrich et al., 1999), the information which cannot be provided by DXA. Since the introduction of micro computed tomography (microCT), it has been the reference methodology to investigate bone tissue morphology (Ruegsegger et al., 1996). Soon after specific methods were developed to transform these three dimension (3D) images into specimen-specific microCT based finite element models (microFE) (Hollister et al., 1994; van Rietbergen et al., 1995; Verhulp et al., 2008), which has the potential to fill the gap.

However, even though they showed great potential in predicting mechanical properties of bone tissue, such models need to be verified and validated (V&V) through accurate

experiments in the laboratory. In particular, it becomes fundamental to V&V the local predictions of displacement and strain if we want to use the models at tissue and cell scales, where the biomechanical behaviour is closely related to biological function of bone tissue. Therefore the goal of this PhD thesis was to evaluate the ability of microFE models to estimate the local mechanical properties of cancellous bone tissue. This goal was achieved by defining three sub-goals. *First*: to conduct a systematic convergence study of cancellous bones of different mesh types with linear elastic and non-linear constitutive equation; *Second*: to challenge the displacements predicted by different verified microFE models of different cancellous bone tested with two independent experimental setups by comparison with a novel DVC-based approach; *Third:* as currently there is no experiment method to validate the strain at 10-20 µm level, typical element size used in microFE models, to compare the strain and stress fields predicted by different tissue modelling methods in the light of their respective idealisations.

7.2. Main contributions and general discussion

The results of the convergence study in **Chapter4** confirmed that the linear elastic simulation of cancellous bones with HOMO-HEXAs, assures convergence of the displacements, stress and strain for an element size of 30-40 µm. In particular, by conducting the study using different samples, scanned at different voxel sizes, all HOMO-HEXAs converged at the same rate – models with element size smaller than one quarter of the average trabecular thickness. Therefore this modelling framework is robust and the converged model element size can be used for future reference. HETE-HEXAs, accounting for differences in local mineralization distribution in each mesh refinement, converged only at a smaller element size (20 µm). In spite of requiring more pre-processing time to generate, HOMO-TETRA by preserving the same geometry over each mesh refinement showed better local convergence (for Specimen3 at 5.9 million of NDOFs) than HOMO-HEXA (for Specimen3 at 6.8 million of NDOFs) and HETE-HEXA (for Specimen3 at 44.1 million of NDOFs). Nonlinear simulations on the other hand, do not always guarantee the convergence at the same voxel size converged in linear simulation due to the nature of nonlinear constitutive equations. Such models are fundamental in order to simulate the local yielding of the cancellous bone structure and therefore it becomes crucial to quantify the modelling discretization errors. Correspondingly, a local convergence study should always be conducted before any further analysis of the model.

The validation study presented in **Chapter5** showed that the boundary condition (BC) plays a big role in predicting local mechanical properties of cancellous bone. In particular, microFE models with "interpolated BCs" (BC matched with DVC measurements of corresponding layers) predict local displacements with excellent accuracy compared to other BCs (BCs assigned according to the nominal force and displacement applied in the experiments). In every validation study the BCs imposed in the model should be the same as in the experiments. However, in some cases where the experimental protocol is complex (such as in situ mechanical testing within a microCT scanner), it is not trivial to control them during the tests and it becomes very hard to accurately replicate them into the models. Therefore it is necessary to compare the outputs of models and experiments by measuring the deformation of the sample under real BCs, which may be quite different from the nominal conditions. The results proved the strength of our method: even though it is difficult to control an ideal uniaxial compression in microCT scanner, the BC derived from DVC measurements is still able to replicate the experiments by catching the displacement distribution at the specimens' surfaces. Either the inclusion of the local heterogeneity (HETE-HEXA) or the accurate recovery of the boundary (HOMO-TETRA) has only a minimal impact on the local displacement prediction compared to the HOMO-HEXA – the traditional mesh generation scheme widely used in the microCT-based cancellous bone modelling. The consistency of these results across all specimens tested with different experiment setups and different mesh types, suggest that the modelling methods we proposed in this study are robust in this regard.

No experimental measurement with sufficient accuracy and spatial resolution is available to validate the strain predictions. However, the three broad families of modelling methods used throughout in the thesis rely on fairly different idealisations and simplifications. Thus in **Chapter6**, we compared the strain fields predicted by these three modelling methods two by two, in order to explore the effect of specific idealisations on the prediction of strains. Results showed that differences in displacement, strain and stress exist locally between two HEXA models, due to different conditions of element connectivity and levels of anisotropy. In particular, the HETE-HEXA is able to catch the local mineralization distribution, as well as the connectivity through partially mineralized tissue which is not modelled in HOMO models. Under displacement-based loading conditions the two HEXA models produced similar strains

in the loading direction; considering the higher computational cost of HETE-HEXA, the advantage of this modelling method over traditional less computationally expensive HOMO-HEXA seems minimal, at least for models generated from microCT data at the 10-20 μm resolution. However, considering the ability of HETE-HEXA of catching local mineralization distribution and possibly mitigating the partial volume effect, their potential may increase if applied to lower resolution images as clinical CT scans performed at larger voxel size (e.g. high-resolution peripheral quantitative computed tomography (HRpQCT) at a typical voxel size of 82 μm (Christen et al., 2013)). The HOMO-TETRA predicted in regions with significant strain gradients higher strains than both HOMO-HEXA and HETE-HEXA, suggesting that a better boundary recovery may capture more accurately and smoothly the strain gradients near the surface, where the predictions of both HEXAs tend to fluctuate due to jagged surface. HOMO-HEXA predicted on average strains 23% lower than HOMO-TETRA along loading direction, with average local strain difference of 49% for strains over 4000 με, and peak differences over 70%.

On the basis of these results, we can conclude that all methods perform similarly in term of displacement predictions, but HOMO-TETRA is probably preferable in predicting accurately strain at the tissue scale, especially if the purpose is to investigate the bone tissue fracture using strain-based failure criteria (Bayraktar et al., 2004; Pistoia et al., 2002; Schileo et al., 2008). Therefore, we conclude amongst different tissue modelling techniques, HOMO-TETRA is highly recommended, in spite of the higher difficulty in generating them, especially for low volume fraction specimens. Further investigation on its strain prediction need to be done when there is a proper validation method to measure the strain at the scale of tens of microns.

7.3. Limitations

This thesis focused on V&V of cancellous bone specimen at the tissue scale, the scale where the interaction between mechanical stimuli and biological function become mostly evident, which is critical in exploring bone remodelling. While the objectives of this research project have been successfully achieved, there are a few limitations that are worth of mention. First, in the convergence study, we investigated only one point subjected to highest principal strain in each model. This is due to the need of maximum strain failure criterion mostly used in studying bone tissue (Schileo et al., 2008).

However, when we repeated the study for the HOMO-HEXA model of specimen1 at the location where the peak stress error was predicted, we reached identical conclusions. This should not come as a surprise, as all nodes investigated with the maximum strain criterion belong to the first five elements of highest stress error. However, this has to be treated with caution in the future. If the one's interest is the highest prediction value, then the convergence study using maximum value criterion might be sufficient; if one's interest is the overall model in predicting the local values, the convergence study should focus on the region with the highest stress error. Additional caution should be taken with the mesh convergence results for the HETE-HEXAs, as convergence theory does not strictly apply to heterogeneous materials. Second, all the coarser Cartesian mesh refinements were generated using subsampled image datasets. By subsampling, the noises inherent in microCT are lessened, which doesn't reflect the true image quality scanned at that specific resolution. Therefore, it might be worth investigating the microFE models using image datasets scanned with different spatial resolution, so that the effect of the noises on the convergence behaviour can be taken into account. Third, we used only three specimens displayed relatively high bone volume fraction (BV/TV) and trabecular thickness. Depending on species, anatomic sites, imaging modalities, microFE conversion techniques and loading conditions, the convergence behaviour of the model could be different (van Rietbergen, 2001). Therefore, it remains to be investigated using more samples on how much the results would change for less dense specimens in the verification studies and validation studies of microFE models using DVC. Further, although being able to resolve the accurate geometry of cancellous bone tissue, the greyscale obtained from microCT, even after polynomial correction, is likely to be affected by beam hardening artefacts, resulting in noises in images and even less accurate predictions of local tissue mineral density (TMD) (Kazakia et al., 2008). Both factors have a huge impact on the local mechanical behaviour of HETE-HEXA models. Thus, it would be worth investigating in the future how much sensitive the local TMD affect the displacement and strain prediction of HETE models using synchrotron radiation micro-computed tomography (SRμCT), which by using mono-energetic, high flux, parallel beam, is able to provide high signal-to-noise ratio and more accurate TMD measurements than microCT. Moreover, if larger compressive loads experiments would be analysed, nonlinear models (Harrison et al., 2013) would become fundamental in order to simulate the local yielding of the trabecular bone structure.
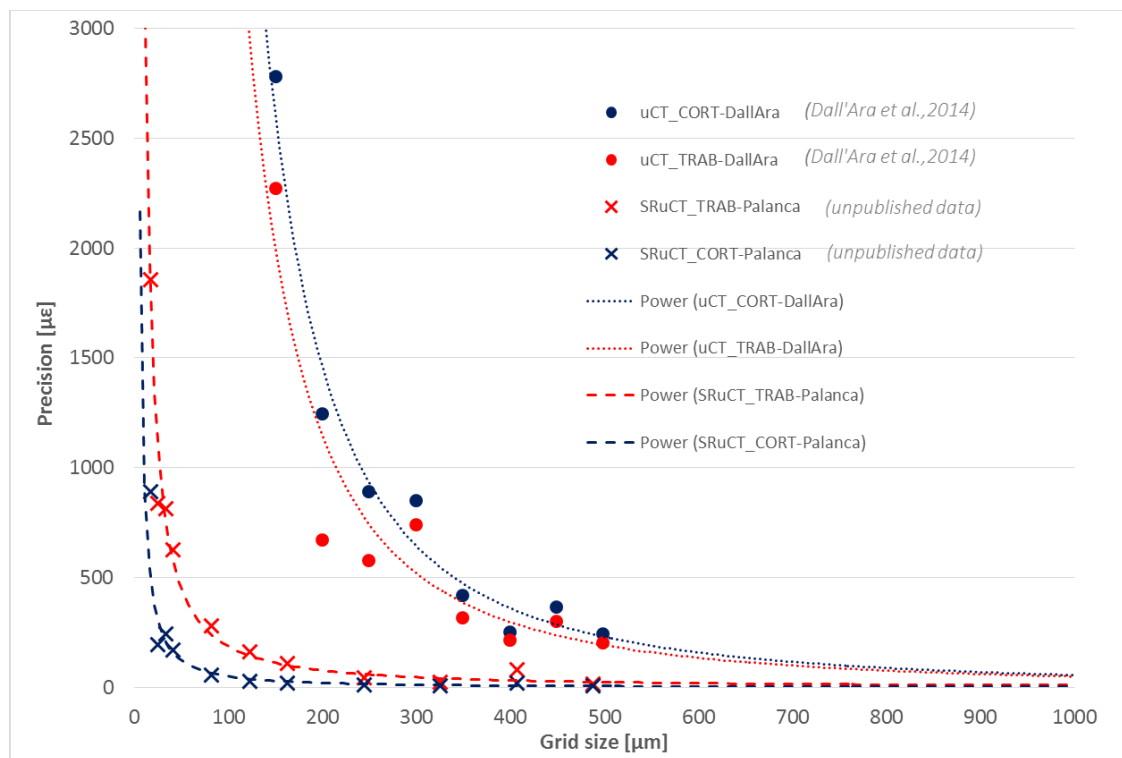
Fig.7.1. *Preliminary results for precision-grid size relationships using DVC combined with µCT datasets (dotted line) and SRµCT (dashed line) for cortical (blue) and trabecular (red) bone. Figure provided by Dr Dall'Ara.*

7.4. Future prospects

The accuracy and precision of the DVC in predicting strains was performed by registering two repeated scans of the same specimen and was estimated with the mean and standard deviation of the difference between the nominal (strain should be zero) and the measured variables (Dall'Ara et al., 2014). The subset size has been indicated as possibly the most influential parameter in terms of measurement precision(Jandejsek et al., 2011) and analysis showed that the precision errors decrease with increasing the subset size of the region analysed by following power laws (Dall'Ara et al., 2014). This is due to the requirement for successful measurements of displacement that the selected subset, used to track changes between undeformed and deformed images, be large enough so that during the correlation procedure, the intensity pattern is sufficiently unique in order to distinguish itself from all other subsets (Roberts et al., 2014). Current microCT-based DVC method provide strain measurement with precision in the order of hundreds of µε only for large grid sizes (e.g. 202 µε for subsampling areas of approximately 500 µm, whereas very high errors were found: in the order of several

thousands of με for grid size of approximately 50μm as reported by Palanca et al. (2015)), making it impossible to validate the strain with spatial resolutions similar to the one obtainable with microFE models. One potential way of improving this method is to improve the image quality to feed the registration with, for example by imaging the bone tissue with SRμCT. In particular, following the same procedure reported in (Dall'Ara et al., 2014), it is shown that the strain error in trabecular bone (red dashed line) can achieve approximately 200 με for subsampling areas of approximately 100 μm (Fig.7.1), improving the spatial resolution for similar errors five times compared with microCT data. However, while the potential of SRμCT-based DVC method is clear for both cortical and trabecular bone, it should be noted that right now there is no protocol to perform stepwise mechanical testing at the SRμCT facility without damaging the sample. If the problem can be fixed in the near future, then strain predicted by different microFE models may be validated and the advantage of using certain mesh type becomes more evident.

7.5. Conclusions

Within the scope of the present thesis, three important achievements in microCT-based bone tissue modelling methods have been made. First, conducting convergence studies of different microFE models according to patch test, the discretization error on local mechanical properties can be quantified, which is essential in exploring bone mechanobiology. By using verified microFEs in further analysis, the computational cost is largely reduced while the accuracy of the mathematical model is still assured. Second, we proposed a robust approach in validating microFE predicted displacement field using a novel DVC technique. By showing accurate and consistent results for both independent experimental protocols and for different specimens, scanned and subsampled with different voxel size, and meshed with different modelling techniques, it is confidently to say that the verified microFE models are at least able to produce accurate displacement field – the fundamental results for linear elastic FE field problem. Third, by comparing three tissue modelling methods, we have illustrated the differences in these models in predicting local mechanical properties and recommended the usage of HOMO_TETRA model due to its smoothed boundary for better strain prediction on the trabecular surfaces, especially one's interest is the local failure of the bone tissue. Validation of the microFE models with strain at the scale of tens of microns needs to be done in the future by combining DVC method with better quality imaging technique

such as SRμCT. By then, failure region of the bone specimen can be located and the advantage of using certain mesh type would become more evident. In conclusion, this thesis showed a systematic method to conduct V&V of different microCT-based tissue modelling methods. Considering the results shown, the workflow we proposed here is therefore robust and can be used as benchmark for future reference in tissue modelling works.

7.6. References

Bayraktar, H.H., Morgan, E.F., Niebur, G.L., Morris, G.E., Wong, E.K., Keaveny, T.M., 2004. Comparison of the elastic and yield properties of human femoral trabecular and cortical bone tissue. J. Biomech. 37, 27-35.

Borah, B., Gross, G.J., Dufresne, T.E., Smith, T.S., Cockman, M.D., Chmielewski, P.A., Lundy, M.W., Hartke, J.R., Sod, E.W., 2001. Three-dimensional microimaging (MRmicroI and microCT), finite element modeling, and rapid prototyping provide unique insights into bone architecture in osteoporosis. Anat. Rec. 265, 101-110.

Brask-Lindemann, D., Cadarette, S.M., Eskildsen, P., Abrahamsen, B., 2011. Osteoporosis pharmacotherapy following bone densitometry: importance of patient beliefs and understanding of DXA results. Osteoporos. Int. 22, 1493-1501.

Christen, D., Melton, L.J., 3rd, Zwahlen, A., Amin, S., Khosla, S., Muller, R., 2013. Improved fracture risk assessment based on nonlinear micro-finite element simulations from HRpQCT images at the distal radius. J. Bone Miner. Res. 28, 2601-2608.

Dall'Ara, E., Barber, D., Viceconti, M., 2014. About the inevitable compromise between spatial resolution and accuracy of strain measurement for bone tissue: a 3D zero-strain study. J. Biomech. 47, 2956-2963.

Harrison, N.M., McDonnell, P., Mullins, L., Wilson, N., O'Mahoney, D., McHugh, P.E., 2013. Failure modelling of trabecular bone using a non-linear combined damage and fracture voxel finite element approach. Biomechanics and modeling in mechanobiology 12, 225-241.

Hollister, S.J., Brennan, J.M., Kikuchi, N., 1994. A homogenization sampling procedure for calculating trabecular bone effective stiffness and tissue level stress. J. Biomech. 27, 433-444.

Jandejsek, I., Jirousek, O., Vavrik, D., 2011. Precise strain measurement in complex materials using Digital Volumetric Correlation and time lapse micro-CT data. 11th International Conference on the Mechanical Behavior of Materials (Icm11) 10, 1730-1735.

Kanis, J.A., Johnell, O., 2005. Requirements for DXA for the management of osteoporosis in Europe. Osteoporos. Int. 16, 229-238.

Kazakia, G.J., Burghardt, A.J., Cheung, S., Majumdar, S., 2008. Assessment of bone tissue mineralization by conventional x-ray microcomputed tomography: comparison with synchrotron radiation microcomputed tomography and ash measurements. Med. Phys. 35, 3170-3179.

Kim, S.H., Suh, H.S., Cho, M.H., Lee, S.Y., Kim, T.S., 2009. Finite element simulation of ultrasound propagation in bone for quantitative ultrasound toward the diagnosis of osteoporosis. Conf. Proc. IEEE Eng. Med. Biol. Soc. 2009, 436-439.

Palanca, M., Tozzi, G., Cristofolini, L., Viceconti, M., Dall'Ara, E., 2015. Three-dimensional local measurements of bone strain and displacement: comparison of three digital volume correlation approaches. J. Biomech. Eng. 137.

Pistoia, W., van Rietbergen, B., Lochmuller, E.M., Lill, C.A., Eckstein, F., Ruegsegger, P., 2002. Estimation of distal radius failure load with micro-finite element analysis models based on three-dimensional peripheral quantitative computed tomography images. Bone 30, 842-848.

Roberts, B.C., Perilli, E., Reynolds, K.J., 2014. Application of the digital volume correlation technique for the measurement of displacement and strain fields in bone: a literature review. J. Biomech. 47, 923-934.

Ruegsegger, P., Koller, B., Muller, R., 1996. A microtomographic system for the nondestructive evaluation of bone architecture. Calcif. Tissue Int. 58, 24-29.

Salehi-Abari, I., 2015. Early diagnosis of osteopenia/osteoporosis by bone mineral density test using DXA method in early adulthood. Int. J. Rheum. Dis.

Schileo, E., Taddei, F., Cristofolini, L., Viceconti, M., 2008. Subject-specific finite element models implementing a maximum principal strain criterion are able to estimate failure risk and fracture location on human femurs tested in vitro. J. Biomech. 41, 356-367.

Sedlak, C.A., Doheny, M.O., Estok, P.J., Zeller, R.A., Winchell, J., 2007. DXA, health beliefs, and osteoporosis prevention behaviors. J. Aging Health 19, 742-756.

Ulrich, D., van Rietbergen, B., Laib, A., Ruegsegger, P., 1999. The ability of three-dimensional structural indices to reflect mechanical aspects of trabecular bone. Bone 25, 55-60.

van Rietbergen, B., 2001. Micro-FE analyses of bone: state of the art. Adv. Exp. Med. Biol. 496, 21-30.

van Rietbergen, B., Weinans, H., Huiskes, R., Odgaard, A., 1995. A new method to determine trabecular bone elastic properties and loading using micromechanical finite-element models. J. Biomech. 28, 69-81.

Verhulp, E., van Rietbergen, B., Muller, R., Huiskes, R., 2008. Indirect determination of trabecular bone effective tissue failure properties using micro-finite element simulations. J. Biomech. 41, 1479-1485.